ASSESSMENT OF GLOBAL BUCKLING AND FATIGUE LIFE FOR STEEL

CATENARY RISER BY

HULL-RISER-MOORING COUPLED DYNAMIC ANALYSIS PROGRAM

A Thesis

by

TAESUNG EOM

Submitted to the Office of Graduate Studies of
Texas A&M University
in partial fulfillment of the requirements for the degree of

MASTER OF SCIENCE

Chair of Committee,   Moo-Hyun Kim
Committee Members,   Jun Zhang
    Alejandro H. Orsi
Head of Department,   John Niedzwecki

August 2013

Major Subject: Ocean Engineering

ABSTRACT

Steel Catenary Riser (SCR) is a popular solution for a floating production facility in the deep and ultra-deep ocean. In the analysis of SCR, the behavioral characteristics are investigated to check the failure modes by assessing the magnitude and the frequency of the stress and strain which SCR goes through in time series. SCR is affected by the motions of connected floating production facility and exciting environmental loads. The driven force and motion of SCR has an interaction with seabed soil which represents the stiffness and friction force where SCR touches the seabed. Dynamic response of SCR is primarily caused by the coupled motion of floating structure. The displacement of floating structure is often large and fast enough to cause short cycles of negative and positive tension on SCR. The interaction between SCR and seabed is concentrated at the touchdown zone resulting into the compression and corresponding deformation of pipeline at the position. This paper presents models of floating production facilities and connected mooring lines and SCRs in 100-year hurricane environmental loads and seabed, focusing on the motional characteristics of SCR at the touchdown zone. In time series simulation, the model of SCR is first analyzed as a pipeline with indefinite elasticity so that the SCR does not fail even if the exciting loads exceed the property limit of SCR. Then the SCR design is manually checked using criteria for each failure mode to estimate the integrity.

DEDICATION

To my wife, Moon Sun Kim

ACKNOWLEDGEMENTS

TABLE OF CONTENTS

LIST OF FIGURES

LIST OF TABLES

1 INTRODUCTION

1.1 General

As the water depth for oil and gas production increases and locations become remote, technologies for economical solutions have been developed. Offshore production facilities for oil and gas production include SPAR and Floating Production Storage and Offloading (FPSO). Each of these structures has an optimized design concept for operation. Also, to attach offshore pipelines on the seabed to specific floating offshore structures, steel pipelines such as Top Tension Riser (TTR), Steel Catenary Riser (SCR) and Flexible Riser have been employed. Figure 1.1 shows examples of a typical floating production facility and riser configuration.

SCR is a steel pipeline that hangs from a floating production facility to the seabed. It is free-hanging and curves down gently to the touchdown point (TDP) on the seabed. Figure 1.2 describes the configuration of SCR touchdown zone (TDZ). Major concerns with the SCR design include several failure modes which are primarily related to the behavioral characteristics of SCR on the seabed. Particularly, the magnitude and number of repeated bending and tensile stress near the TDZ have high correlation with those failures. The soil model on the seabed and the interaction with SCR are the important factors for the analysis, while the modeling contains a lot of complexities to be considered. Therefore it is very important to analyze the behavioral characteristics and corresponding stress which the pipeline goes through with the realistic environmental load and seabed model.
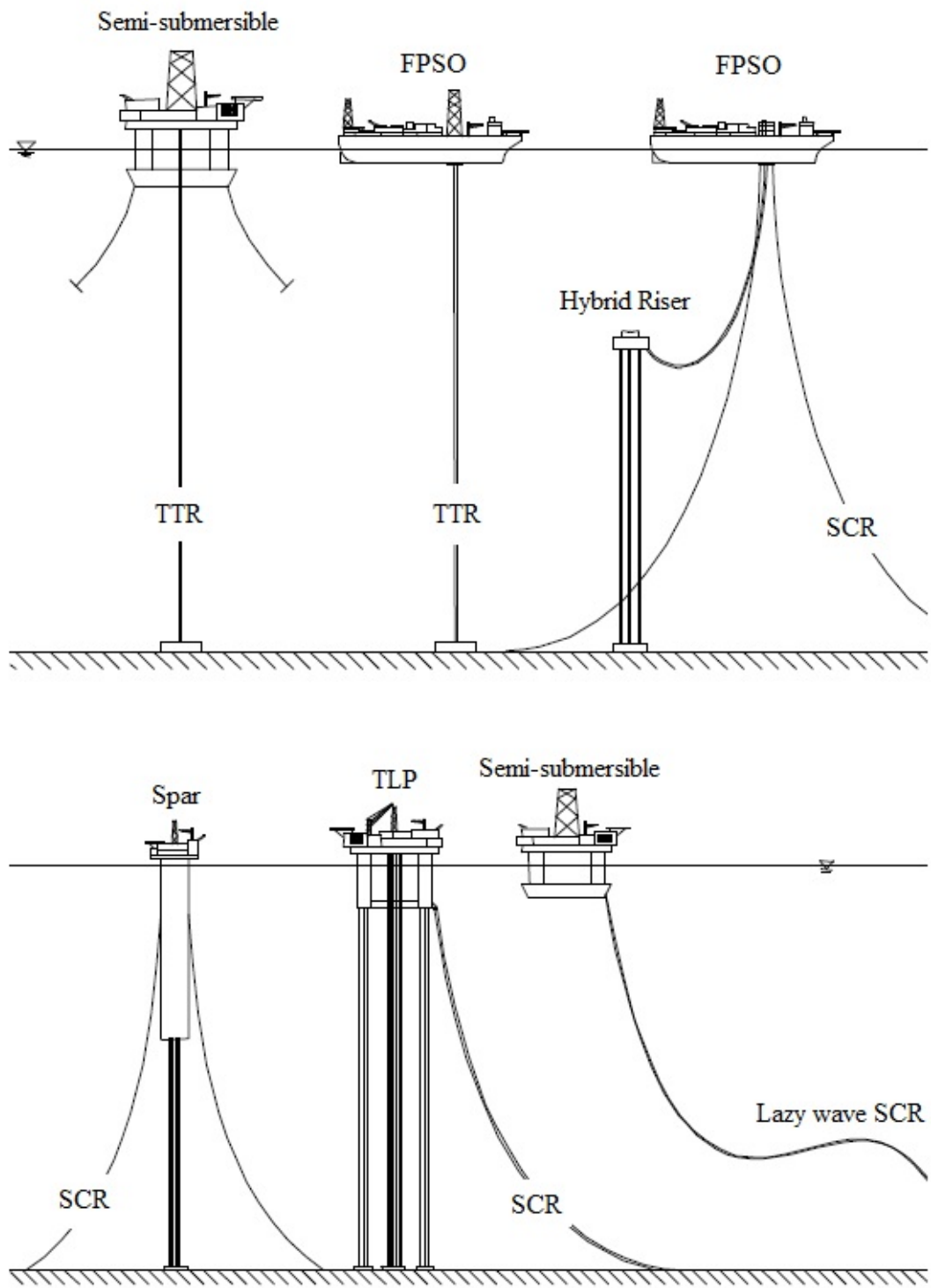
Figure 1.1   Examples of floating structure and riser configuration (DNV-OS-F201)
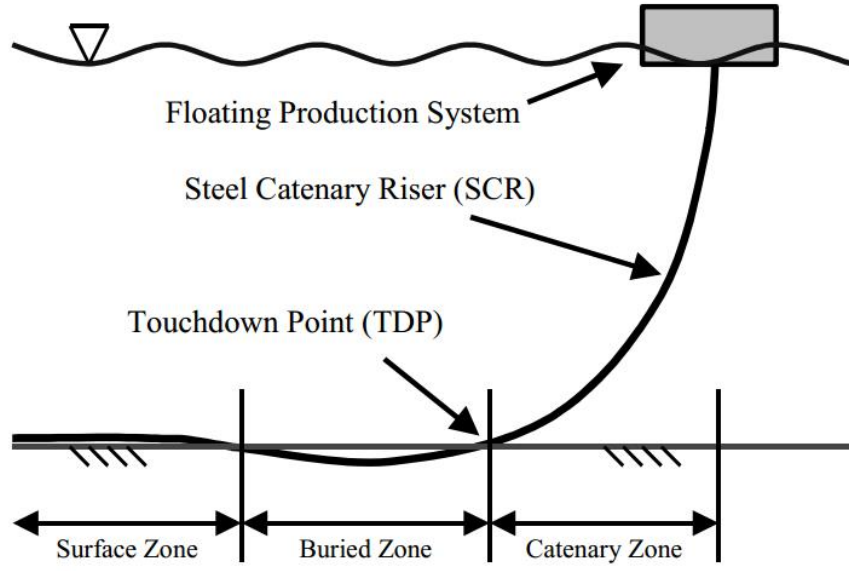
Figure 1.2   General catenary arrangement (Bridge et al, 2003)
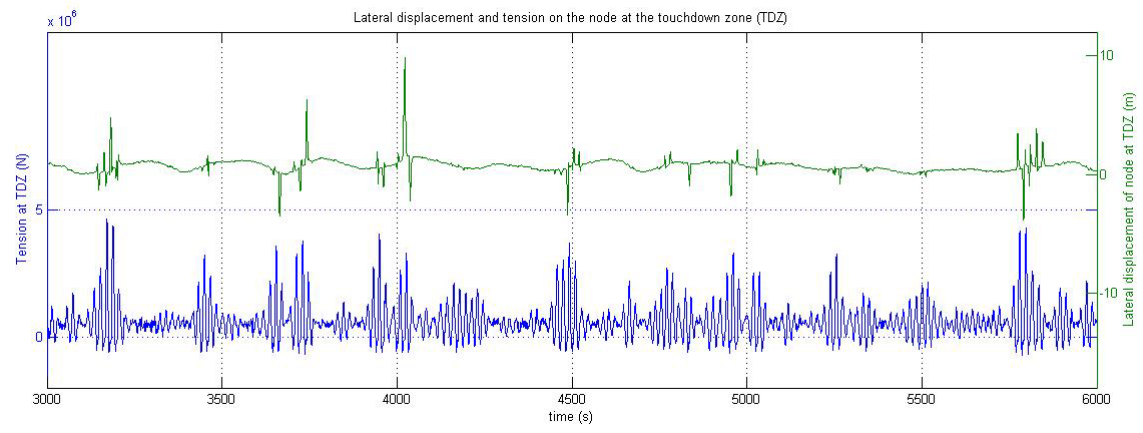
Figure 1.3   Lateral displacement and tension time series of node at TDZ

1.2   Concept of spar and FPSO

The spar platform is a large single vertical cylinder which supports a deck. The concept of the spar platform states that due to its large draft and corresponding displacement, its natural period is so large that it is possible to avoid the dominant wave energy from the peak period of exciting waves. The design concept leads to small heave and pitch response motions of the spar platform during operation of the production facility and allows to install the risers to dry trees. Nevertheless, the second order low-frequency effect of wave and wind load can excite large resonant motion and tension responses in mooring lines which maintain the position of the spar platform. The second order load plays an important role contributing to the motions of floating structure and tensions in the mooring lines in platform design. Thus, a reliable dynamic analysis technique is required to analyze the spar platform.

FPSO is a combined design of storage and production at the remote development site and it has been spotlighted as one of the most economical solutions for deepwater oil production. Some FPSOs are passively moored through a turret system so that the tanker can weathervane or rotate in response to the environmental loads in the direction of wind, wave and current in a hurricane. The waves, winds, and currents are usually non-parallel and often subject FPSO to quartering or beam seas which can cause the significant response of a ship-shaped hull of FPSO. Compared to the spar platform, the heave response motion of FPSO is larger than that of the spar platform. The large amplitude and velocity of heave motion of an FPSO can result in negative effective tension on SCR which is connected to FPSO through the turret. Particularly, the compression on SCR

near TDZ can lead to a failure mode such as local buckling and fatigue failure. Therefore the behavioral characteristics of SCR near TDZ must be carefully analyzed to estimate the possibility of failure mode from the motion of FPSO.

1.3   Sub-critical local dynamic buckling of SCR

When a floating platform experiences large response to the exciting environmental load which does not include too small frequency, the motion often causes compression and corresponding instability of the connected SCR system. The large displacement and velocity of platform drive the decrease of effective tension along SCR and particularly result in the compression near TDP since the closer to the seabed the smaller the tension on the SCR. This compression propagates along SCR with increasing local buckling until the platform motion turns to the opposite direction in its interval of response motion. Then the deformation of SCR vanishes and tension along SCR recovers. Kuiper et al (2007) named this instability of riser as sub-critical local dynamic buckling. In this study, the research focus is made on the mechanism of the sub-critical local dynamic buckling.

1.4   Literature review and objective

Song and Stanton (2009) introduced the procedure for the analysis and major design issues of SCR, presenting the related techniques, software, rules and regulations. They outlined the analysis flow in which the procedure is initiated by design basis and leads to fatigue analysis of SCR including VIV, VIM and motion fatigue, emphasizing

the shell element model of SCR near TDZ for the compression assessment. However, the seabed model which makes friction to the lateral displacement of pipe and causes lateral buckling is not fully considered in the study and they also mention the needs of more study for the pipe-soil interaction.

Seabed model normally focuses on vertical stiffness and lateral friction. Bruton et al (2006, 2008) illustrated the lateral pipe-soil interaction in a case study (SAFEBUCK JIP) introducing the mechanism of lateral buckling of subsea pipeline and heating/cooling driven pipe walking on seabed. In their model, As-laid position of the subsea pipeline does not go through the repeated cycle of touch and separation to the seabed. Since the vertical displacement to the seabed is driven by the weight of SCR, the soil berms in the lateral directions of pipeline is simulated in their simulations and tests. Zhou et al (2010) addressed the interaction between pipe walking and lateral buckling on seabed in cyclic displacement, defining the pipe walking as a global axial displacement driven by start-up/shut-down cycles of high thermal loading. Aubeny (2008, 2009) presented a seabed model with soil stiffness and backbone curve to simulate the penetration of SCR into the seafloor and cyclic unloading and reloading using the P-y curve. Nakhaee (2010) also introduced and modeled the degradation P-y curve for seabed in his dissertation. However, their SCR model for the P-y curve is cyclic heave motion which does not fully consider the lateral deformation of pipeline on seabed caused by the compressional force and corresponding local sub-critical buckling. The seabed memory in their model is simulated as the trench at TDZ.

The vertical motion of a floating production facility is an important driving factor for SCR compression. Many analyses of floating production facilities and mooring-risers have been conducted to establish criteria for the coupled motion and behavior of floating facilities and mooring-risers. Cheng et al (2007) introduced the correlation between hang-off vertical velocity and tension on SCR near TDZ. Also, McCann (2003) and Zou (2012) introduced the relation between hang-off velocity and terminal velocity to estimate the compression on SCR using frequency domain solution. Those assessment techniques are efficient for the estimation, while they are not as accurate as time series analysis with refined seabed model.

Kuiper et al (2007) have found that the heave motions of platform with high amplitudes and frequencies result into destabilization of vertical riser. With the heave motion of platform, the lateral deformations are initialized at the hang-off point as a pulse and propagate through the riser to downward. The pulse widens while its propagation to the touchdown point (TDP) owing to the dispersion and loses its energy because of hydrodynamic damping. Therefore the maximum lateral deformation on the riser is observed near the TDP. They named this deformation as sub-critical local dynamic buckling and it is the phenomenon which is observed in this study.

Although SCR is a popular solution in terms of cost and efficiency, an extreme environmental condition to a vessel-type floating structure often results in the failure of SCR. Yue et al (2011) suggested lazy-wave SCR as an alternative for the turret moored FPSO and comparing the performance and fatigue life of a lazy-wave SCR with a simple SCR.

In this study, the sub-critical local dynamic buckling of SCR at TDZ which is driven by coupled motion of floating structure in time series is investigated. The investigation requires enough consideration of seabed model which includes the stiffness to the vertical force and friction to the lateral motions. In order to avoid complexity, the heat on the pipeline which generates expansion and contraction of pipeline is not considered. Also, corresponding global and local buckling in a segment of SCR is investigated based on the procedure and criteria of DNV RP F110 (Det Norseke Veritas, 2007). The coupled behavior of SCR and floating production facilities are analyzed using the hull-riser-mooring coupled dynamic analysis program, CHARM3D.

The CHARM3D program is a program for the analysis of 3-D hull-riser-mooring coupled dynamics. It was developed by the authors' group to analyze the coupling effects between floating platforms and mooring/riser systems (Kim et al, 2001; Tahar and Kim, 2003; Yang and Kim, 2010). It also provides a time-domain solution for the hull-mooring-riser coupled static and dynamic analysis of offshore structure systems. Verifications for CHARM3D have been made through numerous comparisons against experiments and field data for more than a decade. In this study, the assessment of SCR global buckling and check of integrity near the touchdown zone are investigated with CHARM3D.

The process and criteria for global buckling assessment of submarine pipelines are also introduced in DNV RP F110 followed by an integrity check which investigates failure modes such as local buckling, fracture and fatigue.

2   PROCEDURE OF ANALYSIS

In this section, the concept of the analysis and methodology are introduced based on the procedure. The analysis starts from the preliminary design of the system configuration including the floating production facility, mooring lines and risers. Then the static and dynamic motion analysis of the system is performed to assess global buckling caused by negative effective tension on SCR. Once global buckling is assessed, investigation of the failure modes of SCR is required for the pipeline integrity check and it is possible to verify the initial design of the system based on the result of this integrity check.

2.1   Numerical model

2.1.1   Spar system

2.1.1.1   Spar platform

The spar platform model for this study is a classic spar with dimensions designed by Koo (2003) with a length of 214.88 meters and diameter of 37.19 meters as shown in Figure 2.1. The main particulars of the spar platform are shown in Table 2.1. Its average draft is 198.12 meters with total displacement of 220,740 metric tons and it targets water depth of 3,000 meters in this study. The total displacement is the sum of light ship weight, ballast water, liquid cargo and top tensions for the mooring lines and SCR. Light ship weight includes the hull, topside without any ballast water and cargo. For the numerical analysis, the submerged hull is discretized into 1504 rectangular panels. The

number of panels affects the running time of the analysis and so a limited mesh number (less than 2,000) is recommended. Also, the normal vector of the panel should be toward the outside. With the discretized spar model, WAMIT calculates the hydrodynamic coefficients and forces required for a time series analysis. Figure 2.2 shows the discretized model of the submerged spar hull.
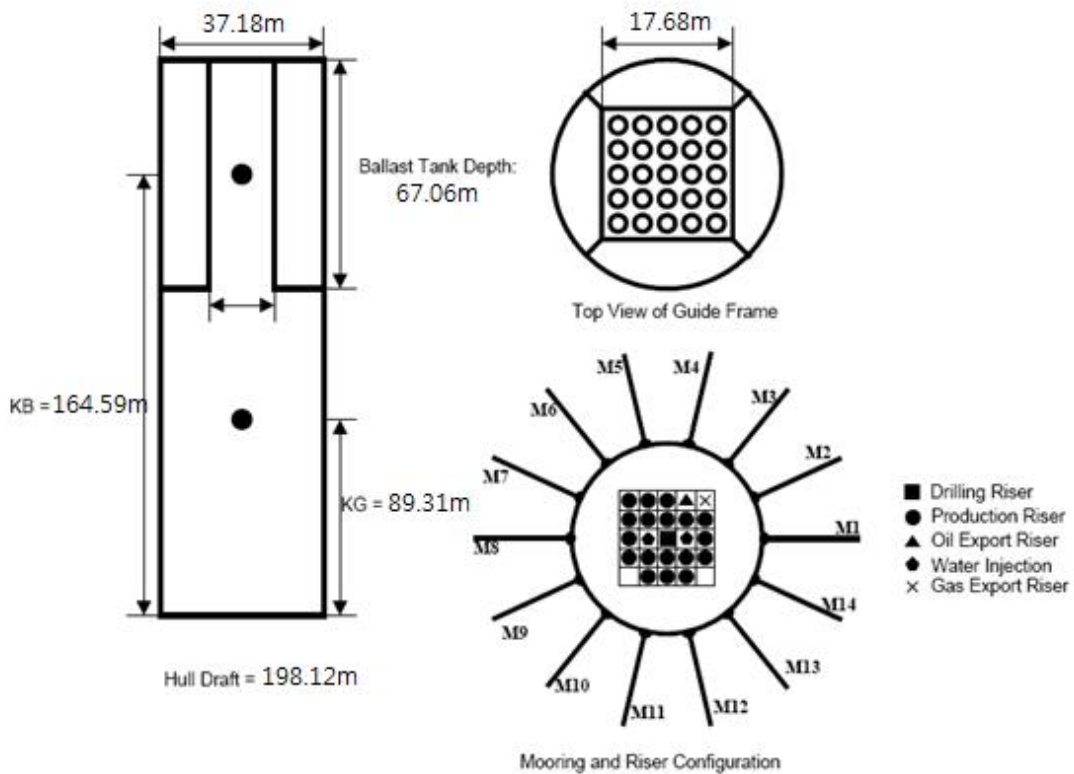
Figure 2.1   Configuration of spar hull and mooring/riser (Koo, 2003)
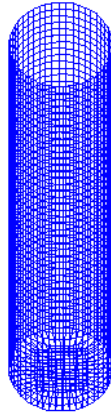
Figure 2.2 Mesh generation of spar

Table 2.1 Principal particulars of spar platform (Koo, 2003)

Description	Magnitude
Water depth (m)	3,000
Total Displacement (m.ton)	220,740
Diameter (m)	37.19
Length (m)	214.88
Draft (m)	198.12
Hard Tank Depth (m)	67.06
KB (m)	164.60
KG (m)	125.58
KG (Based on Total Displacement) (m)	89.31
Radius of Gyration (m)	Pitch = 67.36, Yaw = 8.69
Drag Force Coefficient	1.15
Center of Pressure (m)	220.07

2.1.1.2   Mooring lines and risers

The spar system consists of 14 mooring lines and 24 risers including 23 TTRs and 1 SCR. In the numerical model, the end points of lines are assumed to be connected to a rigid body by stiff springs with stiffness. The stiffness is controlled by the input between the lines and rigid bodies. Also, in order to model the buoyancy-can effect to the vertical riser, the connection point between riser and spar platform is modeled as a horizontal spring in order to make the free vertical motion of the spar. Therefore the vertical stiffness of the spring at the top end of the vertical risers is zero. The arrangement of installed mooring lines and risers is shown in Figure 2.1. For the purpose of reducing weight, the main part of each mooring line is composed of polyester except for the two end parts which are chain.   The characteristics of the mooring line are summarized in Table 2.2.

Table 2.2   Mooring system characteristics

Line	No.	Segment Length (m)	Wet Weight (kg/m)	Dry Weight (kg/m)	Axial Stiffness (kN)	Bending Stiffness (kN.m^2)
Chain	14	76.368(top) 351.10(floor)	322.638	381.374	1,328,000	0
Polyester		3,036	2.668	21.713	240,192	0

Each vertical riser is supported by a freely floating buoyancy-can near the top of the riser and passes through a series of buoyancy-cans and riser guide frames. In the numerical model, the risers are modeled up to the keel of the spar and the effects of buoyancy-cans are approximately performed in the hull restoring coefficient matrix

(Tahar et al., 2002). Figure 2.3 and Tables 2.3 and 2.4 show the configuration of the buoyancy-can supported vertical riser system for a spar platform and the characteristics of each riser.
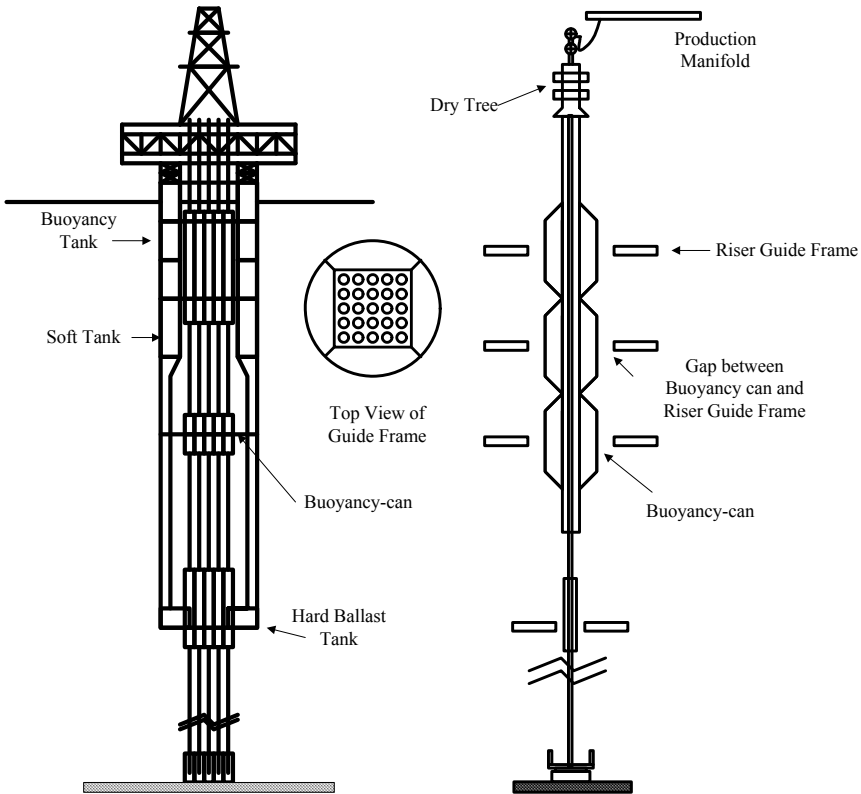
Figure 2.3   Schematic drawing of spar riser system with buoyancy-can (Koo, 2003)

Table 2.3   Riser system characteristics

Line	No.	Segment Length (m)	Wet Weight (kg/m)	Dry Weight (kg/m)	Axial Stiffness (kN)	Bending Stiffness (kN.m^2)
Drilling Riser	1	2,803	366.177	595.266	1.20E+07	0
Production Riser	18	2,803	194.757	269.511	2.99E+06	0
Water Injection	2	2,803	63.019	80.354	1.84E+06	0
Oil Export	1	2,803	159.381	264.31	4.63E+06	0
Gas Export	1	2,803	73.827	153.161	4.63E+06	0
SCR	1	5,000	76.86	134.1	2.70E+06	1.34E+04

Table 2.4   Pre-tensions of lines

Line		No.	Pre-tension at hang-off point (kN)
Mooring line		14	3,150
Riser	Production	18	5,731
	Water injection	2	1,864
	Oil export	1	4,702
	Gas export	1	2,181
	Drilling	1	10,760
	SCR	1	3,500

One steel catenary riser (SCR) of 5,000m length with axial and bending stiffness is included in this study. The discretization of SCR is an important factor in the analysis of force factors on SCR. Finer elements are modeled near the touchdown point and

hang-off point. The intermediate part is composed of a relatively coarse element as shown in Table 2.5.

Table 2.5   Discretization of SCR model

	From Fairlead	Remaining part	From Anchor point
Segment length (m)	200	4,000	800
Outer Diameter (m)	0.268		
Inner Diameter (m)	0.224		
Wet weight (kg/m)	76.86		
Dry weight (kg/m)	134.1		
# of Element	20	20	80

2.1.2   FPSO system

2.1.2.1   FPSO

The FPSO model used in this study is a 200,000 DWT crude oil tanker moored in 1,829 meters water depth by a taut chain-polyester-chain mooring system with turret. The internal single turret is located 63.55 m away from the forward perpendicular with a diameter of 15.85 m. The main parameters of the turret-moored FPSO are those of the model set up by DeepStar Offshore Industry Consortium (Wichers and Devlin, 2001) as given in Table 2.6. For the numerical analysis, the submerged part of the FPSO hull is discretized into 1684 rectangular panels. Figure 2.4 shows the discretized model of the submerged part of the FPSO hull.
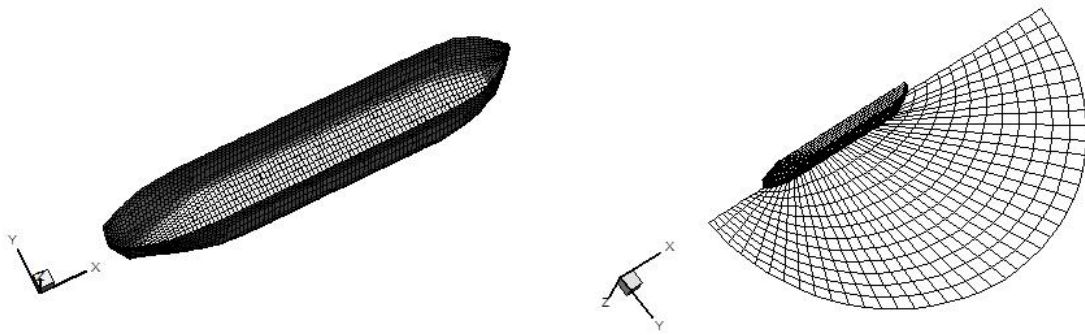
Figure 2.4   Discretization of FPSO hull and free surface (Kim and Kim, 2002)

Table 2.6   Main particulars of FPSO (Kim and Kim, 2002)

Description	Symbol	Unit	Value
Production level		*bpd*	120,000
Storage		*bbls*	1,440,000
Vessel size		*kDWT*	200.0
Length between perpendicular	Lpp	*m*	310.00
Breadth	B	*m*	47.17
Depth	H	*m*	28.04
Draft	T	*m*	18.9
Displacement		*MT*	240,869
Length-beam ratio	L/B		6.57
Beam-draft ratio	B/T		2.5
Block coefficient	Cb		0.85
Center of buoyancy Forward section10	FB	*m*	6.6
Center of gravity above Base	KG	*m*	13.3
Water plane area	A	m^2	13,400
Frontal wind area	Af	m^2	1011.7
Transverse wind area	Ab	m^2	3771.9
Roll radius of gyration at CG	R_{xx}	*m*	14.77
Pitch radius of gyration at CG	R_{yy}	*m*	77.47
Yaw radius of gyration CG	R_{zz}	*m*	79.30
Turret in center line behind Fpp (20.5% Lpp)	Xtur	*m*	63.55
Turret elevation below tanker base	Ztur	*m*	1.52
Turret Diameter		*m*	15.85

2.1.2.2   Mooring lines and risers

The main particulars of the mooring lines are almost identical to those of the model set up by DeepStar Offshore Industry Consortium (Wichers and Devlin, 2001). Meanwhile, the riser configuration model is slightly modified; 77 degrees are used

instead of 80.9 degrees (Kim and Kim, 2002). Other than the arrangement of installation, material properties of the riser models are re-calculated based on Young's modulus of steel (78.5 kN/m3) to obtain the appropriate bending stiffness, tensile stiffness, outer diameter and wall thickness of SCR. The particulars of the mooring lines and risers are shown in Tables 2.7 ~ 2.11.

Table 2.7   Main particulars of mooring systems (Kim and Kim, 2002)

Designation	Unit	Value
Water depth	m	1829
Pre-tension	kN	1424
Number of lines		4×3
Degree between the 3 lines	deg.	5
Length of mooring line	m	2652
Radius of location of chain Stoppers on turn table	m	7.0
Segment 1(ground section): Chain		
Length at anchor point	m	121.9
Diameter	cm	9.52
Dry weight	N/m	1856
Weight in water	N/m	1615
Stiffness AE	kN	912081
Mean breaking load (MBL)	kN	7553
Segment 2: Polyester Rope		
Length	m	2438
Diameter	cm	16.0
Dry weight	N/m	168.7
Weight in water	N/m	44.1
Stiffness AE	kN	186825
Mean breaking load (MBL)	kN	7429
Segment 3(FPSO section): Chain		
Length at anchor point	m	91.4
Diameter	cm	9.52
Dry weight	N/m	1856
Weight in water	N/m	1615
Stiffness AE	kN	912081
Mean breaking load (MBL)	kN	7553

Table 2.8   Hydrodynamic coefficients of mooring lines

Hydrodynamic Coefficients	Symbol	Chain	Rope/Poly
Normal drag	C_{dn}	2.45	1.2
Normal added inertia coefficient	C_{in}	2.00	1.15

Table 2.9   Main particulars of risers

Riser type	Qt	OD	ID	AE	EI	Weight (dry/wet)	C_{dn}
		m	m	kN	$kN.m^2$	N/m	
Liquid production	4	0.254	0.208	3.34E+06	2.25E+04	134/99	1
Gas production	4	0.386	0.350	4.16E+06	7.06E+04	167/47	1
Water injection	2	0.531	0.495	5.80E+06	1.91E+05	286/193	1.414
Gas injection	2	0.287	0.247	3.36E+06	3.01E+04	185/119	1.414
Gas export	1	0.343	0.309	3.48E+06	4.64E+04	138/43	1
Each length	3,057m						

Table 2.10   Discretization of SCR model

	Fairlead				Anchor point
Segment length (m)	300	1617	100	40	1000
Wet weight (kg/m)	105.661	105.661	105.661	105.661	105.661
Dry weight (kg/m)	196.441	196.441	196.441	196.441	196.441
EA (kN)	1.833E+07	1.833E+07	1.833E+07	1.833E+07	1.833E+07
EI (kN-m2)	2.756E+02	2.756E+02	2.756E+02	2.756E+02	2.756E+02
# of Element	10	13	2	2	100

Table 2.11   Pre-tensions of lines

Line		No.	Pre-tension at hang-off point (kN)
Mooring line		12	1,420
Riser	Liquid production	4	2,224
	Gas production	4	1,223
	Gas injection	2	4,702
	Gas export	2	2,181

In the numerical model, the mooring lines are assumed hinged at the turret and anchor position. The riser is also hinged downward at the turret and thus the riser tension is included in the calculation of vertical static equilibrium of the FPSO system. The hull/mooring/riser fully coupled model for the FPSO system is depicted in Figure 2.5.
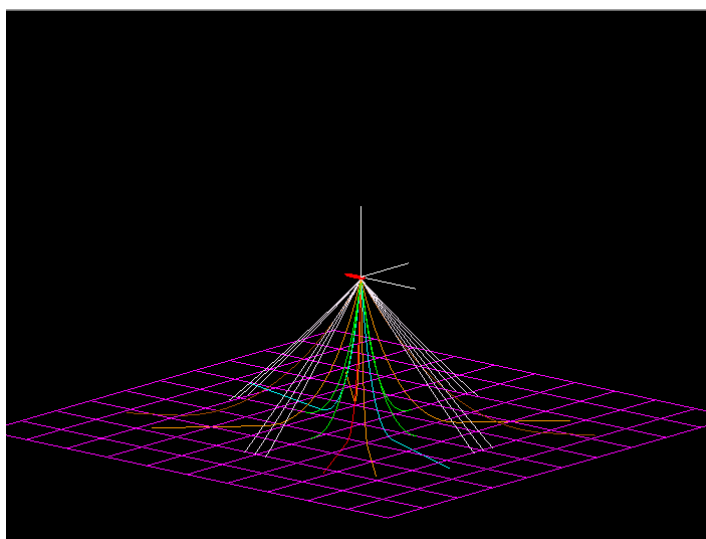
Figure 2.5   Hull/mooring/riser coupled model

2.1.3 Environmental condition

The environmental condition is the 100-year return period hurricane event at the central area of the Gulf of Mexico. Input data for the environmental condition is provided by API Bulletin 2INT-MET (2007). The JONSWAP spectrum with stiffness parameter of 2.4 is employed to generate the long crested irregular random waves. Dynamic behavior of a time varying wind load is generated for 3 hours based on the 1-point wind spectrum of API. The strong wind condition with 3 seconds gust velocity within an hour corresponds to the API Bulletin and is included in the generated wind load model. The adopted API wind spectrum and designed wind speed $u(z,t)(m/s)$ at height $z(m)$ above sea level for period $t \leq t_0 = 3600s$ is formulated as follows:

$$S(f) = \frac{320 \left(\frac{U_0}{10}\right)^2 \left(\frac{z}{10}\right)^{0.45}}{\left(1 + \tilde{f}^n\right)^{(5/3n)}}$$

$$\tilde{f} = 172 f \left(\frac{z}{10}\right)^{2/3} \left(\frac{U_0}{10}\right)^{-0.75}$$

where n = 0.468 and

- $S(f)(m^2 s^{-2}/Hz)$ is the spectral energy density at frequency $f(Hz)$

- $z(m)$ is the height above sea level

- $U_0(m/s)$ is the 1-hour mean wind speed at 10m above sea level

$$u(z,t) = U(z)[1 - 0.41 I_u(z) \ln(t/t_0)]$$

where the 1-hour mean wind speed $U(z)(m/s)$ level z is given by

21

$$I_u(z) = 0.06\left[1+0.043U_0\right]\left(\frac{z}{10}\right)^{-0.22}$$

where $U_0(m/s)$ is 1-hour average speed at 10 meter elevation.

For simplicity, wind, wave and current are assumed to propagate to the same direction. Table 2.12 shows the numerical input for the environmental load.

Table 2.12   Environmental condition

Return Period	100 year	
Hs (m)	15.79	
Tp (sec)	15.40	
γ	2.4	
1-hour Mean Wind Speed (m/sec)	48.01	
Current Profile	Depth (m)	Speed (m/sec)
	0.0	2.41
	50.4	1.80
	100.8	0
	1,829 (FPSO)	0
	3,000 (SPAR)	0

2.1.4   SCR discretization

As already mentioned, SCR should be discretized carefully in order to avoid numerical errors from too coarse mesh. Among calculated force components, bending moment is especially sensitive to the size of the discretized element and usually the numerical error occurs near TDZ where the maximum bending moment is supposed to be observed.

CHARM3D currently allows a limited number of elements for the discretization of SCR. For efficient discretization, SCR is first divided into several parts including TDZ, near TDZ, near hang-off point and the remaining water piercing part, etc. Discretization with the finest element is required at TDZ and near TDZ. The near hang-off point also requires discretization with the fine element but is less sensitive than TDZ. A comparatively coarse element can be used for the water piercing part of SCR. To double check the accuracy of the calculated bending moment by CHARM3D, it is possible to calculate the bending moment from the displacement data of nodes using an analytical method.

2.1.4.1   Bending moment calculation by analytical method

Theoretically, the bending moment of the plane section beam can be obtained as the product of bending stiffness (EI) and curvature k (=1/R) of the beam. Curvature of the beam is illustrated as shown in Figures 2.6 and 2.7. The curvature of SCR can be obtained from the displacement data at the end points of the element. The output file of

CHARM3D contains the displacement data (node coordinates and unit tangent vectors at each end) so that the bending moment can be obtained by analytical calculation.
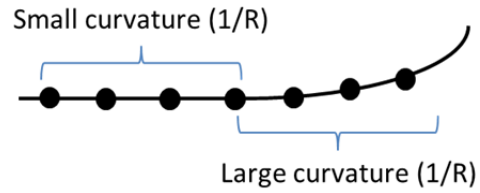
Figure 2.6 Curvature of SCR
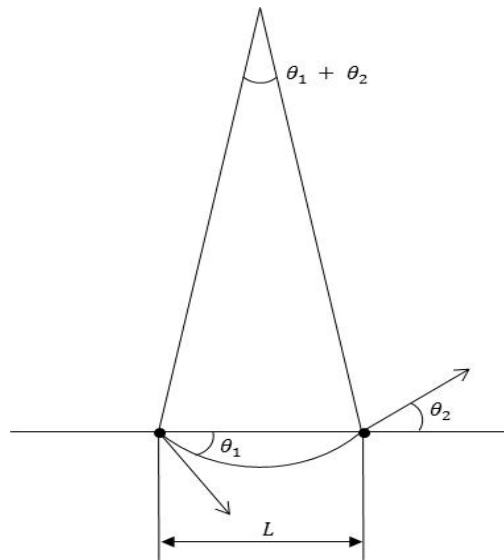
Figure 2.7 Curvature of an element

$$L = \left[2R^2 - 2R^2 \cos(\theta_1 + \theta_2) \right]^{\frac{1}{2}}$$

$$R = \frac{L}{\left[2 - 2\cos(\theta_1 + \theta_2) \right]^{\frac{1}{2}}}$$

$$BM = EI / R$$

2.1.5   SCR-seabed model

The seabed-SCR model is one of the key considerations for the reliable analysis of the behavioral characteristics of SCR. CHARM3D models the seabed as a continuous quadratic-spring foundation to support pipelines on the seabed. The mechanism of seabed stiffness on SCR in the vertical direction is as follows: When SCR is discretized to the finite element, the constant number of springs with given stiffness supports each discretized element. In this study, the seabed stiffness is 1E+07 (N/m2). This seabed model simulates the trenching and upheaval motion of SCR near TDZ with a dynamic displacement on the seabed.

The interaction between SCR and the seabed can be activated using either/both the coulomb friction model or/and the lateral damping force model. The interaction is analyzed with each discretized element of SCR. The magnitude of coulomb friction to the SCR element on the seabed is proportional to the vertical reaction force on the seabed; the coulomb friction is proportional to the square of vertical displacement of SCR in a time series. The magnitude of damping force is proportional to the velocity of the normal direction of each element of SCR. The magnitude of each force model is depicted in Figure 2.8.
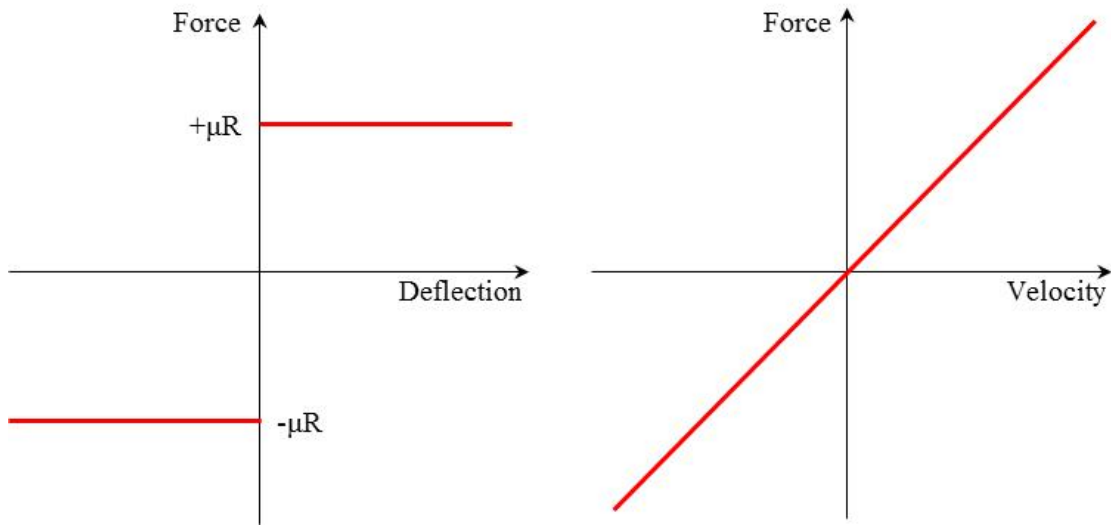
Figure 2.8 Coulomb friction (left) and lateral damping force (right)

2.2   Time series analysis

2.2.1   Static strength analysis

Once all input data for the numerical model of mooring lines and SCRs, as previously introduced, are determined, the corresponding tension along mooring lines and SCRs and the location of the end point of each line on the seabed are obtained using CHARM3D with the configuration of the line. Top tensions of mooring lines and risers are added to the weight of the floating production facility to equal the total displacement. Total displacement is first obtained through hydrostatic analysis of the relation between weight and buoyancy interaction. The hydrostatic analysis determines the equilibrium position of the floating production facility and attached mooring lines and risers before the hydrodynamic analysis in time series. Therefore the magnitude of top tension for

26

each line should be carefully determined so as not to affect the total displacement and corresponding design draft of the floating production facility.

2.2.2   Motion analysis of the floating production facility

In the time series, the motions of the submerged structures are recorded by every time step in axial and rotational directions. The measuring point is the origin of the body-coordinate system for each floating production facility. In the case of a spar platform it is located at the center of the hull section at the designed mean water level, and in the case of FPSO it is located at the center of the section of the turret at the designed mean water level. Through the analysis of motion it is possible to investigate the correlation between the motions of the floating production facility and connected lines, particularly the SCR in this study. The correlation is often found between velocity and force component which requires post-processing of the output data.

2.2.3   Behavioral characteristics of SCR

At TDZ, when negative effective tension is observed, it can lead to a bending moment which represents the curvature. The curvature of SCR is usually found on the seabed and the deformation is mainly a lateral direction. It is known that the maximum tension does not always lead to the maximum bending moment at the position but there is a high correlation between negative effective tension and the occurrence of SCR curvature at the same node.

As a result of the interaction between SCR and the seabed, there are often upheaval motions of SCR on the seabed. When this upheaval motion is observed, the

deformation of SCR needs to be analyzed in three dimensions and requires more complexity for the analysis. The bending moment often spikes when and where this upheaval motion and lateral walk of SCR are found in the same position.

2.2.4   Pipeline walking and lateral buckling

According to DNV-RP-F110, the definition of pipe walking is the axial accumulation of displacement. Lateral buckling is phenomenon of pipeline which is observed in a lateral direction and caused by axial compression.

2.3   Global buckling

2.3.1   SCR compression assessment

D. McCann (2003) introduced the parameter for examining the buckling of SCR using the concept of hang-off velocity and terminal velocity. Terminal velocity is obtained when the sum of drag force and buoyancy equals the downward gravity force. As the hang-off heave velocity increases, the restoring drag force also increases until it cancels out the gravitational acceleration; then the velocity of the element of SCR reaches terminal velocity. Since this parameter is used for the assessment of SCR compression, downward hang-off heave velocity is the target of measurement. Assuming the length is unit length, the equations for the parameter and the variables are as follows:

$$F_{net} = m \cdot g - C_d \cdot \rho \cdot D_{drag} \cdot V_{Terminal}^2 \big/ 2 = 0$$

$$V_{Terminal} = \sqrt{2 \cdot m \cdot g / C_d \cdot \rho \cdot D_{drag}}$$

, where

m = mass,

g = gravity,

C_d = normal drag coefficient,

D_{drag} = Drag Diameter,

ρ = Water density,

$V_{Terminal}$ = Terminal velocity

2.3.2 Global buckling assessment

Global buckling is a buckling as a bar in compression. It is not failure mode, but the response to the compression and imperfection caused by internal / external forces. Practically, the axial force of the pipeline is affected by temperature and pressure. However, in order to minimize the complexity of the analysis, in this study those properties are neglected in the calculation of global buckling.

The procedure and criteria for the assessment of global buckling follow the scenarios of DNV-RP-F110 which depend on the directions of the SCR deformation (lateral deformation only or three dimension deformation) and the criteria regarding the tension and bending moment. The flowchart for the scenario of lateral deformation only

is shown in Figure 2.9. The assessment result is one of three conditions (No buckling / Maybe buckling / Buckling) for the follow-up check for pipeline integrity (Pipeline Integrity Check list of DNV-RP-F110). The design check for global buckling triggered by imperfection is based on Hobb's (1984) infinite model capacity.

Successful global buckling assessment depends on the selection of the node point from the discretized model of SCR elements and the moment in time series. Since the criteria of global buckling are related to the tension and bending moment, the overall maximum negative effective tension and overall maximum bending moment along SCR in the time series are selected for investigation.
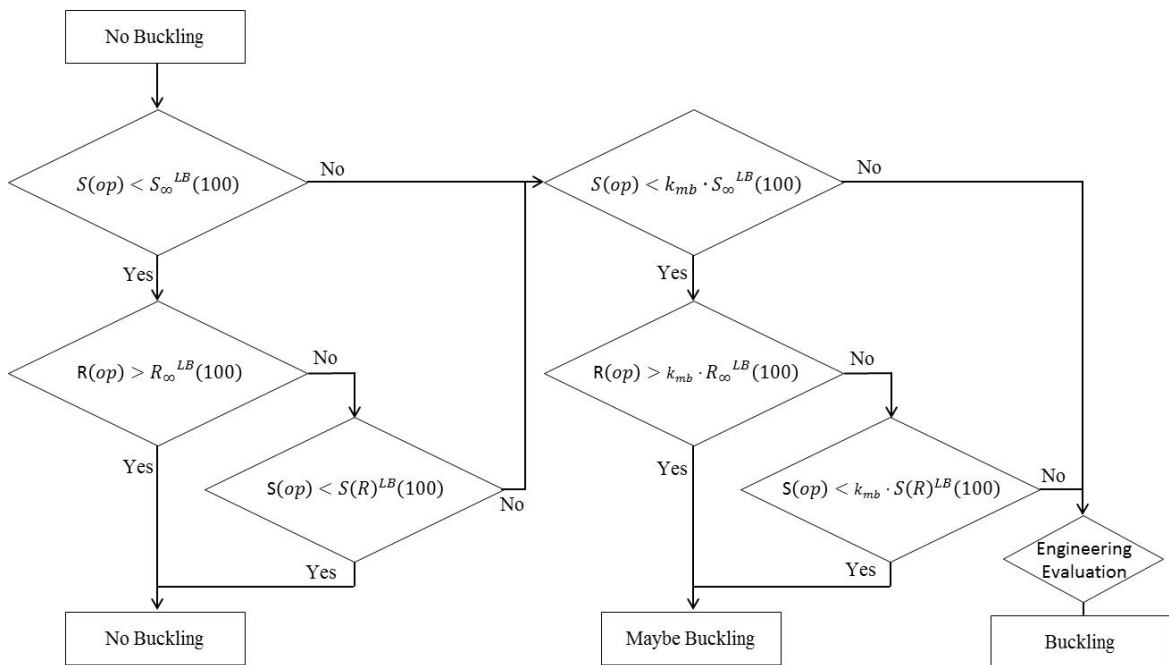
Figure 2.9   Flowchart for imperfection triggering global buckling (DNV-RP-F110)

30

where

$S(op)$: The compressive effective axial force based on operational pressure and temperature

$R(op)$: The radius of imperfection based on operational condition

$$S_{\infty}^{LB}(100) = 2.29 \frac{EI}{\overline{L}^2}, \quad \overline{L} = \left[\frac{(EI)^3}{\left(f_L^{LB}\right)^2 \cdot E \cdot A_s} \right]^{0.125}$$

f_L^{LB}: The Lower Bound lateral soil resistance force, $S(R)^{LB}(100) = f_L^{LB} \cdot R(op)$,

$$R_{\infty}^{LB}(100) = 2.41 \cdot (D-t) \cdot \sqrt{\frac{E \cdot t}{f_L^{LB}}}, \quad t : \text{The nominal thickness of SCR, } k_{mb} = 1.5$$

In order to limit the complexity of the analysis, DNV-RP-F110 suggests a simplified check to determine whether further detailed analysis is required using the following equations. The first equation represents criteria of pin-pin Euler beam buckling and the second equation represents fixed-fixed Euler beam buckling. When the second equation below is satisfied, a more developed analysis is required than the 2D analysis.

$$S_R \leq \frac{\pi^2 \cdot EI}{\left(L_{uplift}(S_R)\right)^2} \quad \text{No lateral buckling}$$

$$S_R \geq \frac{4 \cdot \pi^2 \cdot EI}{\left(L_{uplift}(S_R)\right)^2} \quad \text{Lateral buckling}$$

where

S_R is the effective axial force in the uplift span section

L_{uplift} is the length of the pipeline length lifted off at the free span crests.

2.4   Pipe integrity check (Limit state analysis)

In the pipe integrity check, using the formula in API Recommended Practice 2RD, von Mises stress is obtained as a combined stress level at any point in a pipe. The calculation is based on the internal pressure, yield stress, and tension, bending moment and other constants such as the external/internal diameter of SCR and thickness of wall. Also, the maximum allowable bending moment is obtained using the formula of Hauch and Bai (1999). The formulation for the maximum allowable bending moment is based on the previously calculated bursting pressure, tension, bending moment in the time series and safety factor and properties of SCR. Fatigue damage is calculated and the design is evaluated for short term and long term. Fatigue life is calculated based on the metocean data of target environmental area and obtained stress range through time series analysis.

SMYS (Specified Minimum Yield Strength) and SMTS (Specified Minimum Tensile Strength) are according to values of the typical pipes used in offshore subsea operations under API certification. In this study, these are assumed as below:

$$SMYS = 360 \, MPa$$

$$SMTS = 535 \, MPa$$

2.4.1   Von Mises stress calculations

Von Mises stress criterion is a practical option to calculate the combined stress level at any point in a pipe. API Recommended Practice 2RD suggests the formulation in this section 5.2.4 as follows:

$$\sigma_{API} = max\left[\left\{\left(\sigma_{pr} - \sigma_{p\theta}\right)^2 + \left(\sigma_{p\theta} - \sigma_{pz}\right)^2 + \left(\sigma_{pz} - \sigma_{pr}\right)^2\right\}/2\right]^{\frac{1}{2}}$$

$$U_{API} = \sigma_{API}/\left(C_f C_a \sigma_y\right)$$

$$U_{API} \leq 1$$

where

$\sigma_{pr} = -(p_o D_o + p_i D_i)/(D_o + D_i)$ (Radial stress),

$\sigma_{p\theta} = (p_i - p_o)(D_o/2t_{min}) - p_i$ (Hoop stress),

$\sigma_{pz} = T_w/A \pm M(D_o - t)/(2I_{xy})$, $A = (\pi/4)(D_o^2 - D_i^2)$ (Axial stress),

$I_{xy} = (\pi/64)(D_o^4 - D_i^4)$,

D_o: External diameter, D_i: Internal diameter, T_w: Tension, M: Bending moment,

A: Cross sectional area, I_{xy}: Inertia of the cross section,

σ_y: SMYS specified minimum yield stress, C_f: Design case factor, $C_a = \frac{2}{3}$

Table 2.13   Design case factor (API RP 2RD)

Design Case	Load Category	Environmental Condition	Pressure	Reducer Tensioner Capacity or One Mooring Line Broken	C_f
1	Operating	Max. operating	Design	No	1.0
2	Extreme	Extreme	Design	No	1.2
3	Extreme	Max. operating	Extreme	No	1.2
4	Extreme	Max. operating	Design	Yes	1.2
5	Temporary	Temporary	Associated	No	1.2
6	Test	Max. operating	Test	No	1.35
7	Survival	Survival	Associated	No	1.5
8	Survival	Extreme	Associated	Yes	1.5
9	Fatigue	Fatigue	Operating	No	~

2.4.2   Maximum allowable bending moment criteria

For pipelines subjected to combined pressure, local buckling is one of the potential failure modes. In this study, the maximum allowable bending moment criteria presented by Hauch and Bai (1999) are used to check the local buckling and the formulation and factors (Table 2.14) are given as follows:

$$M_{Allowable(F,p)} = \frac{\eta_{RM}}{\gamma_c} M_p \sqrt{1-(1-\alpha^2)\left(\frac{p}{\eta_{RP}p_l}\right)^2} \cos\left(\frac{\pi}{2}\frac{\frac{\gamma_c F}{\eta_{RF}|F_l|} - \alpha\frac{p}{\eta_{RM}|p_l|}}{\sqrt{1-(1-\alpha^2)\left(\frac{p}{\eta_{RM}p_l}\right)^2}}\right)$$

where

$M_{Allowable(F,p)}$: Allowable bending moment, M_p : Plastic moment, p_l : Limit pressure,

p : Pressure acting on the pipe, F_l: Limit longitudinal force,

F : Longitudinal force acting on the pipe, α : Strength anisotropy factor,

γ_c: Condition load factor, η_R : Strength usage factor, $\alpha = \dfrac{\pi D^2}{4}\left|\dfrac{p_b}{F_l}\right|$,

p_b : Bursting pressure

$$M_p = \left(1.05 - 0.0015\frac{D}{t}\right)SMYS \cdot D^2 t$$

where

D: Average diameter, t: Wall thickness

Limit longitudinal force for compression and tension

$$F_l = 0.5(SMYS + SMTS)A$$

A: cross sectional area

Limit pressure for internal overpressure condition

$$p_l = 0.5(SMYS + SMTS)\frac{2t}{D}$$

The coefficients in the formula are presented in the following table:

Table 2.14   Load and usage factors (Hauch and Bai, 1999)

Safety factor	Safety class	Low	Normal	High
γ_c	Uneven seabed	1.07	1.07	1.07
	Pressure test	0.93	0.93	0.93
	Stiff supported	0.82	0.82	0.82
	Otherwise	1.00	1.00	1.00
η_{RP}	Pressure	0.95	0.93	0.90
η_{RF}	Longitudinal force	0.90	0.85	0.80
η_{RM}	Moment	0.80	0.73	0.65

2.4.3   Fatigue

Fatigue design ensures that the riser has enough fatigue life. Fatigue analysis supports the assessment of fatigue to ensure that the riser will fulfill its intended function during the design life. There are several types of fatigue analysis for the various parts of the riser system — vortex induced vibration (VIV) fatigue analysis of riser and vortex induced (hull) motion (VIM) fatigue analysis of the floating production facility. However, in this study, only global riser fatigue analysis, which is due to the motion of the riser, is introduced using a single S-N curve of DNV RP C203 (Det Norske Veritas, 2010).

2.4.3.1 Long term sea state

Song and Stanton (2009) introduced four-step procedure to calculate the long term fatigue damage using subdivided wave environmental scatter diagram as shown in Figure 2.10.

Step (1): The wave environmental scatter diagram is subdivided into a number of representative blocks

Step (2): Within each block, a single sea state is selected to represent all the sea states within the blcok. The probabilities of occurrence for all sea states within the blcok are lumped to the selected sea state.

Step (3): The fatigue damage is computed for each selected sea state for all the blocks. Fatigue damage will be obtained by counting the stress cycles in the simulated stress time history through Rainflow counting method

Step (4): A weighted summation is finally performed based in the results obtained from step (3) and the lumped probabilities from step

Figure 2.10 Procedure for motion fatigue calculation (Song and Stanton, 2009)

A description of long term sea state using the data of joint frequency of significant wave height and mean wave period is required to obtain sea state probability. In this study, the meteorological data is based on the central area of the Gulf of Mexico

37

in 2012 which was obtained from the database of the National Data Buoy Center (NDBC). For simplicity, the database is divided into 15 blocks according to significant wave height and peak period as shown in Table 2.15.

Table 2.15   2012 Meteorological data of Gulf of Mexico (NDBC)

WIND SPEED (m/s)	WAVE HEIGHT									TOT %	TOT N
	0 - 1.4	1.5 - 3.4	3.5 - 5.4	5.5 - 6.4	6.5 - 7.4	7.5 - 8.4	8.5 - 9.4	9.5 - 10.4	10.5 - 11.4		
0 - 3			-	-	-	-	-	-	-	0.6	1322
	6.9	0.2	-	-	-	-	-	-	-	6.5	15220
4 - 10			*	-	-	-	-	-	-	12.8	29956
	36.6	2	*	-	-	-	-	-	-	25.8	60296
11 - 20				*	-	-	-	-	-	29.4	68778
	30.6	14.9	0.1	*	-	-	-	-	-	16.2	37897
21 - 33				*	-	-	-	-	-	5.1	11885
	0.6	5.6	0.8	*	*	*	-	-	-	2.1	4994
> 34			*	*	*	*	*	*	-	0.1	252
	1.1	0.2	*	*	*	*	*	*	*	1.4	3160
TOTAL %	75.7	23.1	1.1	0.1	0	0	0	0	0	100	
TOTAL N	176871	53924	2628	217	54	40	16	7	3		233760

(* < 0.05%)

2.4.3.2   Short term fatigue damage

The Miner-Palmgren rule is adopted for the calculation of accumulated fatigue damage from stress cycles with variable range. The range of stress is 30 blocks from 0 to 1200 MPa. In order to compute the accumulated stress within the variable range, the

Rain-Flow counting method is adopted. DNV RP F204 (Det Norske Veritas, 2010) introduces the formulation and criteria for the accumulated fatigue damage as follows:

$$D_{fat} = \sum_i \frac{n(S_i)}{N(S_i)}$$

$$D_{fat} \cdot DFF \leq 1$$

where

D_{fat} : Accumulated fatigue damage (Palmgren-Miner rule)

DFF : Design Fatigue Factor (Table 2.16)

$n(S_i)$: Number of stress cycles with range S_i

$N(S_i)$: Number of stress cycles to failure given by S-N curve

Table 2.16   Design fatigue factors DFF (DNV RP F204)

Safety class		
Low	Normal	High
3.0	6.0	10.0

2.4.3.3   S-N curve

The S-N curve contains the basic fatigue capacity, expressing the number of fatigue stress to failure N and the given constant stress range S. DNV RP F204 introduces the relation between those two variables as follows:

$$N = \bar{a} \cdot S^{-m}$$

or equivalently:

39

$$\log(N) = \log(\overline{a}) - m \cdot \log(S)$$

where
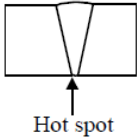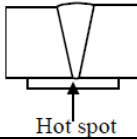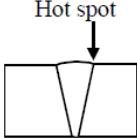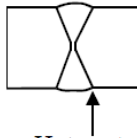
$\overline{a}$ and m are empirical constants established by experiments.

DNV RP C203 provides a database of design S-N curves which is obtained from relevant experiments. In the case of pipeline, the S-N curve is selected based on the characteristics of welding and the tolerance requirement. The S-N curves provided by DNV RP C203 are tabulated as follows:

Table 2.17   S-N curves in seawater with cathodic protection (DNV RP C203)

S-N curve	$N \leq 10^6\,cycles$		$N \geq 10^6\,cycles$ $\log \overline{a_2}$ $m_2 = 5.0$	Fatigue limit at 10^7 cycles	Thickness exponent k	Stress concentration in the S-N detail as derived by the hot spot method
	m_1	$\log \overline{a_1}$				
B1	4.0	14.917	17.146	106.97	0	
B2	4.0	14.685	16.856	93.59	0	
C	3.0	12.192	16.320	73.10	0.15	
C1	3.0	12.049	16.081	65.50	0.15	
C2	3.0	11.901	15.835	58.48	0.15	
D	3.0	11.764	15.606	52.63	0.20	1.00
E	3.0	11.610	15.350	46.78	0.20	1.13
F	3.0	11.455	15.091	41.52	0.25	1.27
F1	3.0	11.299	14.832	36.84	0.25	1.43
F3	3.0	11.146	14.576	32.75	0.25	1.61
G	3.0	10.998	14.330	29.24	0.25	1.80
W1	3.0	10.861	14.101	26.32	0.25	2.00
W2	3.0	10.707	13.845	23.39	0.25	2.25
W3	3.0	10.570	13.617	21.05	0.25	2.50
T	3.0	11.764	15.606	52.63	0.25 for $SCF \leq 10.0$ 0.30 for $SCF \geq 10.0$	1.00

Table 2.18   Classification of welds in pipelines (DNV RP C203)

Description		Tolerance requirement	S-N curve	Thickness exponent k	SCF
Welding	Geometry and hot spot				
Single side	Hot spot	$\delta \le \min(0.15t, 3mm)$	F1	0.00	1.0
Single side	Hot spot	$\delta > \min(0.15t, 3mm)$	F3	0.00	1.0
Single side on backing	Hot spot	$\delta \le \min(0.1t, 2mm)$	F	0.00	1.0
Single side on backing	Hot spot	$\delta > \min(0.1t, 2mm)$	F1	0.00	1.0
Single side	Hot spot	-	D	0.15	Eq (below)
Double side	Hot spot	-	D	0.15	Eq (below)

$$SCF = 1 + \frac{3\delta_m}{t} e^{-\sqrt{t/D}}$$

Based on the information in Tables 2.17 and 2.18, S-N curve D has the most strict tolerance requirement and largest $\log \bar{a}_1$ which means greater resistance to fatigue than other S-N curves in Table 2.18, while F3 shows the lowest tolerance requirement and resistance to fatigue. In this study, F1 is selected as the S-N curve.

2.4.3.4   Long term fatigue damage (DNV RP F204) and fatigue life

After fatigue damage is computed for each selected short-term sea state for all ranges of stress, the weighed fatigue damage accumulation, which is based on the long term sea states, can be obtained as follows:

$$D_L = \sum_{i=1}^{N_S} D_i P_i$$

where

D_L : Long term fatigue damage

N_S : Number of discrete sea state in the wave scatter diagram

P_i : Sea states probability.

D_i : Short term fatigue damage

Fatigue life is determined according to the following equation:

$$T_{fat} = \frac{T_0}{D_L}$$

where

T_{fat} : Fatigue life

T_0 : Timeframe (simulation time)

42

3   CASE STUDIES

3.1   Spar system

3.1.1   Time series analysis on spar

In the given environmental conditions, a time series analysis of the motion of SPAR is performed for 3 hours. The motion of SPAR is classified in 6 modes and analyzed with displacement in a time series. Newman's approximation is applied to the calculation of the second-order difference-frequency wave forces in the bi-frequency domain as introduced by Y.B. Kim and M.H. Kim (2002). The statistics showing the result of the time series are tabulated except for the data of the first 1,000 seconds in order to remove the ramping effect.
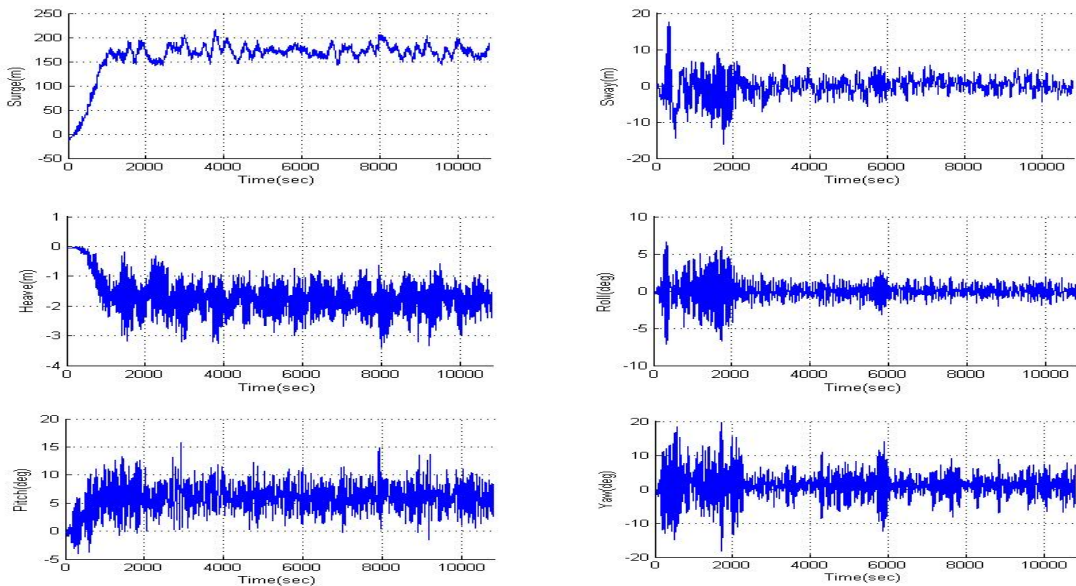
Figure 3.1   Time series of 6DOF motions of spar

43

Table 3.1   Displacement statistics from 1,000 sec to 10,800 sec in time series

	Max	Min	Mean	SD
Surge (m)	216.3898	141.3991	171.7610	12.3117
Sway (m)	9.3708	-16.1051	-0.0909	2.6642
Heave (m)	-0.1877	-3.3958	-1.7950	0.4522
Roll (deg)	5.9575	-6.7201	-0.0111	1.2654
Pitch (deg)	15.7206	-1.5923	6.1258	2.2791
Yaw (deg)	19.6433	-18.2131	1.1410	3.7017

Three hours of time series analysis of spar motion were performed. The ramping effect is observed for approximately 1,000 seconds in each mode of the time series. The plots in Figure 3.1 and the statistics in Table 3.1 show that among axial motion, surge is dominant. This is due to the large profile area of spar to current load. The heave motion is smaller than other axial motions. The buoyancy-can effect decoupled the heave motion of the spar and the vertical risers and therefore the heave motion response of the spar is freed from the vertical tension of TTRs. Compared to the spar with TTRs which is hinge connected, the model in this study has larger heave motion but still the variation of heave motion is within 1 meter. Although the hull of the spar is symmetric to the vertical center axis, the unsymmetrical arrangement of vertical risers causes the sway and yaw motion of the spar system in the time series.

3.1.2   Time series analysis of SCR near TDZ

Analysis of SCR behavior near TDZ is important for the assessment of global buckling and other failure modes such as local buckling and SCR fatigue. For the analysis of SCR at TDZ, six nodes of SCR near the TDZ were chosen for the time series analysis as shown in the following subsection. Those nodes initially lie on the seabed and therefore the observed node motions and force components on the seabed in the time series are considered as the behavioral characteristics of SCR at TDZ. The most significant behavioral characteristics of nodes in the time series should be the force components including tension, bending moment, tensile stress and bending stress. Thus the heave displacement and force components are analyzed respectively for each node and the statistics data is tabulated in the following subsections. The tensile stress and bending stress are investigated on the most critical three nodes near TDZ for further investigation of fatigue analysis.

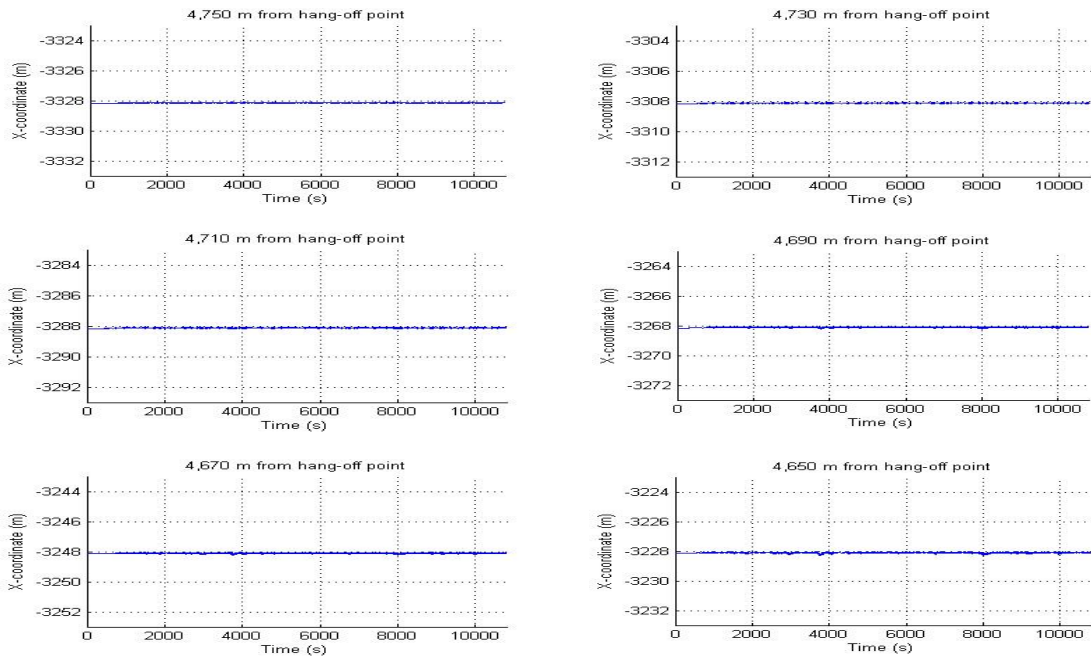**Figure 3.2　X-directional displacement of nodes over SCR near TDZ**
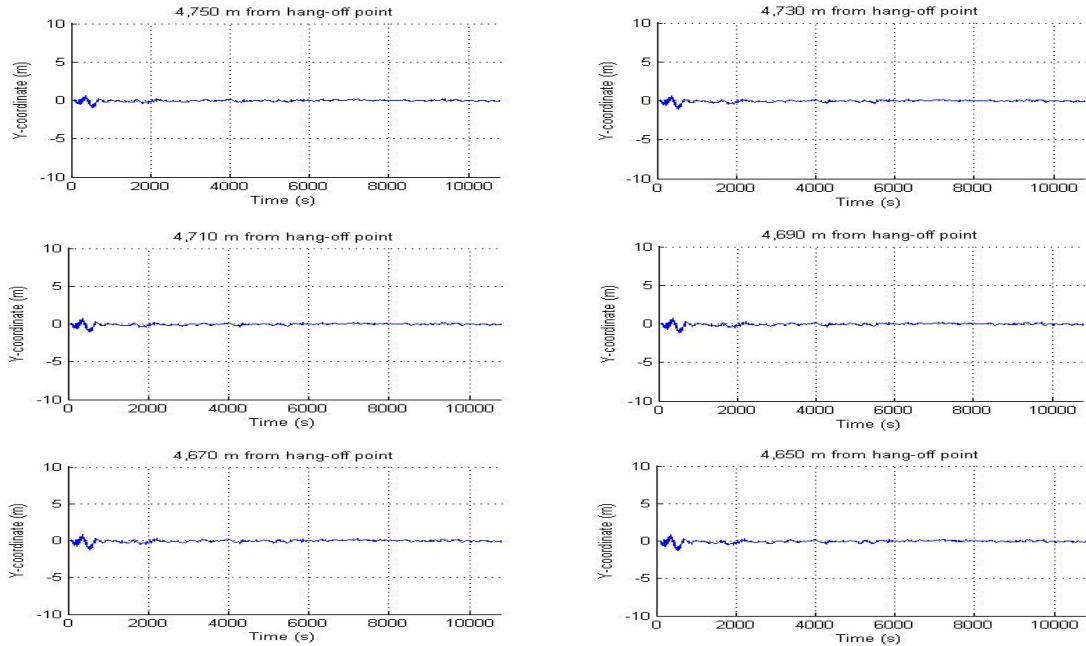
Figure 3.3　Y-directional displacement of nodes over SCR near TDZ
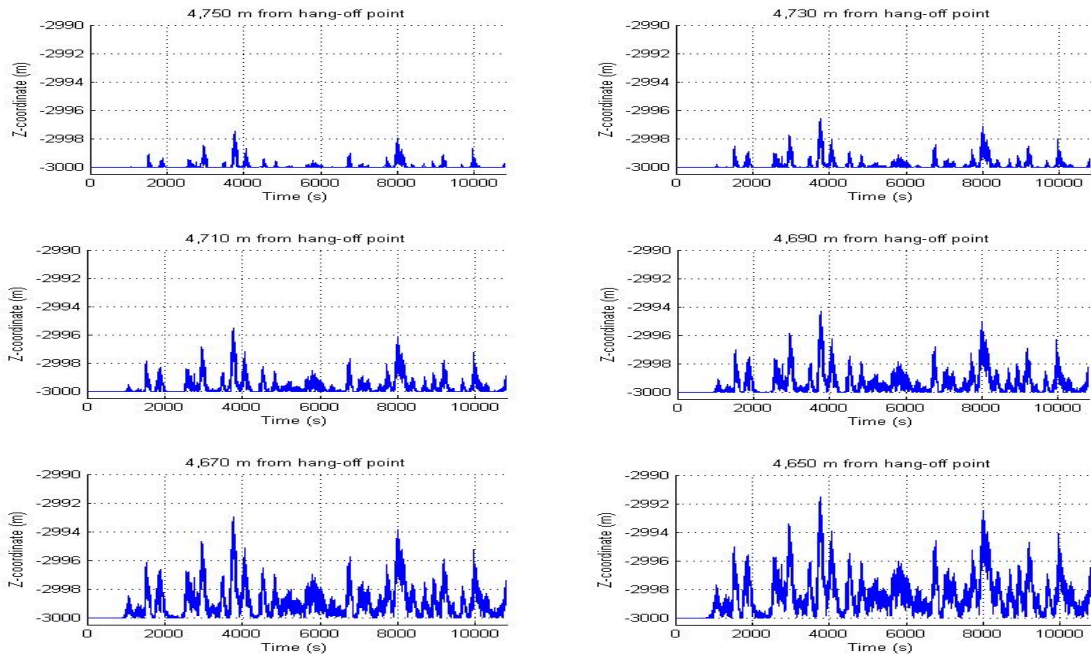
Figure 3.4   Z-directional displacement of nodes over SCR near TDZ
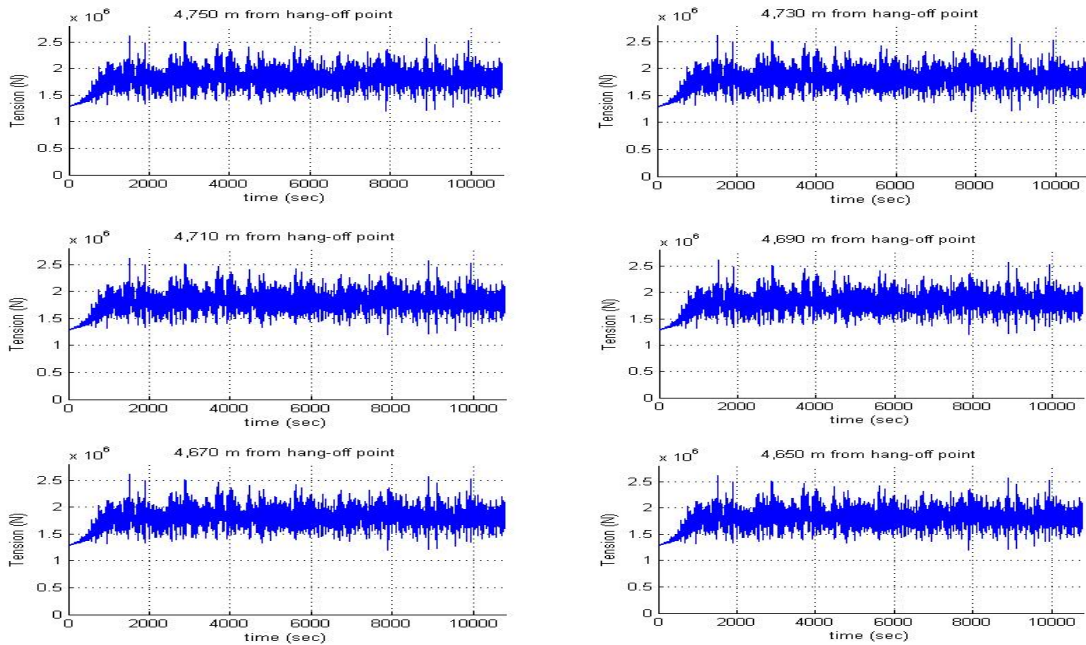
Figure 3.5   Tension at nodes over SCR near TDZ
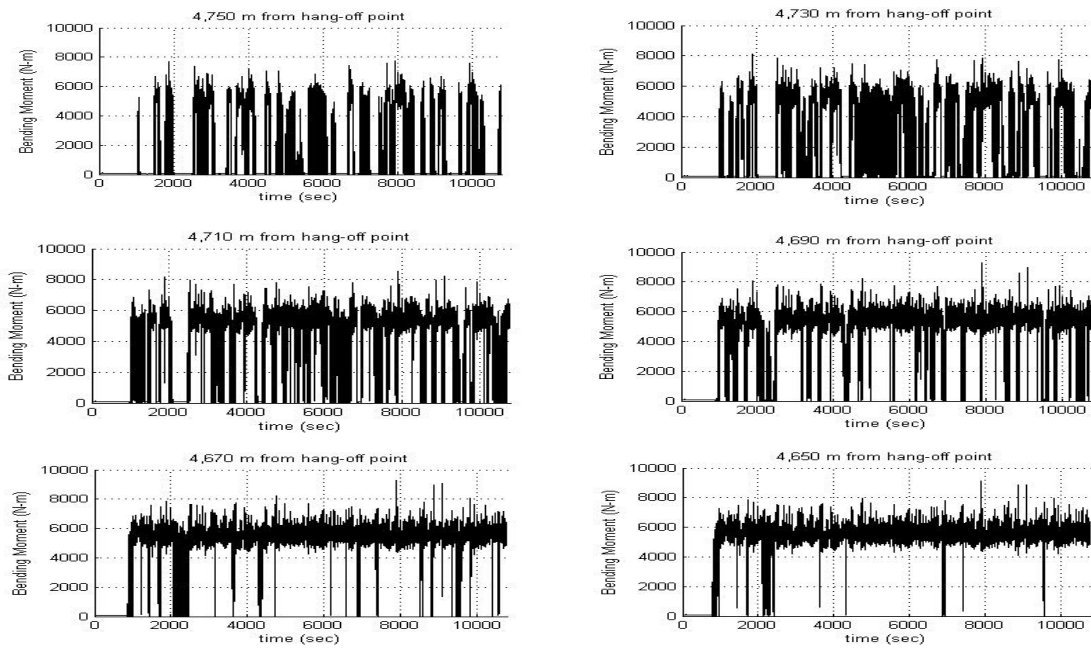
Figure 3.6   Bending moment at nodes over SCR near TDZ
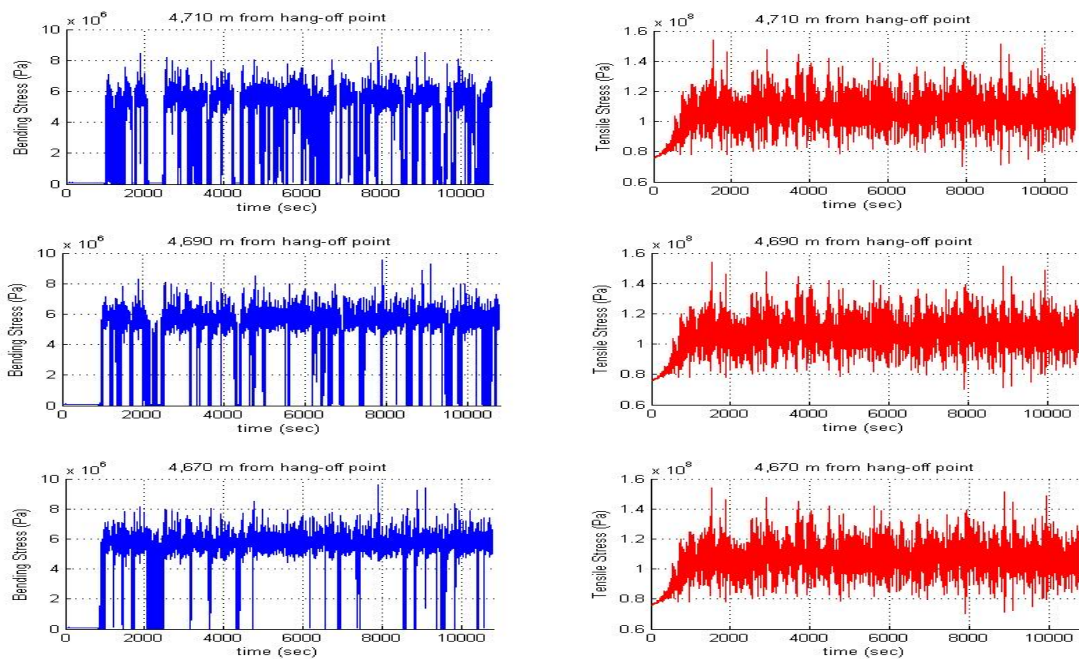
Figure 3.7   Bending stress and tensile stress at nodes over SCR near TDZ

48

Table 3.2   Statistics of time series on the node at 4,750m from hang-off point

	Max	Min	Mean	SD
X-dir coordinate (m)	-3328.1	-3328.2	-3328.1	0.0154
Y-dir coordinate (m)	0.2215	-0.3973	-0.0315	0.0909
Z-dir coordinate (m)	-2,997.5	-3.00E+03	-2,999.9	0.2151
Tension (N)	2.61E+06	1.20E+06	1.83E+06	1.70E+05
Bending moment (N-m)	7.73E+03	3.11E-01	1.61E+03	2.29E+03

Table 3.3   Statistics of time series on the node at 4,730m from hang-off point

	Max	Min	Mean	SD
X-dir coordinate (m)	-3308	-3308.2	-3308.1	0.0165
Y-dir coordinate (m)	0.239	-0.4264	-0.0341	0.0981
Z-dir coordinate (m)	-2996.6	-3000	-2999.8	0.3572
Tension (N)	2.61E+06	1.20E+06	1.83E+06	1.70E+05
Bending moment (N-m)	8.13E+03	1.47E-01	2.67E+03	2.55E+03

Table 3.4   Statistics of time series on the node at 4,710m from hang-off point

	Max	Min	Mean	SD
X-dir coordinate (m)	-3288	-3288.2	-3288.1	0.0179
Y-dir coordinate (m)	0.2566	-0.455	-0.0366	0.1053
Z-dir coordinate (m)	-2995.5	-3000	-2999.7	0.5465
Tension (N)	2.61E+06	1.20E+06	1.83E+06	1.70E+05
Bending moment (N-m)	8.57E+03	3.59E-01	3.82E+03	2.38E+03
Tensile stress (Pa)	1.54E+08	7.00E+07	1.08E+08	1.00E+07
Bending stress (Pa)	8.86E+06	3.71E+02	3.95E+06	2.46E+06

Table 3.5   Statistics of time series on the node at 4,690m from hang-off point

	Max	Min	Mean	SD
X-dir coordinate (m)	-3268	-3268.2	-3268.1	0.0201
Y-dir coordinate (m)	0.2741	-0.4834	-0.0391	0.1125
Z-dir coordinate (m)	-2994.3	-3000	-2999.4	0.7758
Tension (N)	2.61E+06	1.20E+06	1.83E+06	1.70E+05
Bending moment (N-m)	9.26E+03	3.20E-01	4.73E+03	1.83E+03
Tensile stress (Pa)	1.54E+08	7.00E+07	1.08E+08	1.00E+07
Bending stress (Pa)	9.57E+06	3.30E+02	4.89E+06	1.89E+06

Table 3.6   Statistics of time series on the node at 4,670m from hang-off point

	Max	Min	Mean	SD
X-dir coordinate (m)	-3248	-3248.2	-3248.1	0.024
Y-dir coordinate (m)	0.2915	-0.5116	-0.0416	0.1197
Z-dir coordinate (m)	-2993	-3000	-2999	1.0312
Tension (N)	2.61E+06	1.20E+06	1.83E+06	1.70E+05
Bending moment (N-m)	9.29E+03	1.96E+00	5.26E+03	1.20E+03
Tensile stress (Pa)	1.54E+08	7.04E+07	1.08E+08	1.00E+07
Bending stress (Pa)	9.60E+06	2.02E+03	5.44E+06	1.24E+06

Table 3.7   Statistics of time series on the node at 4,650m from hang-off point

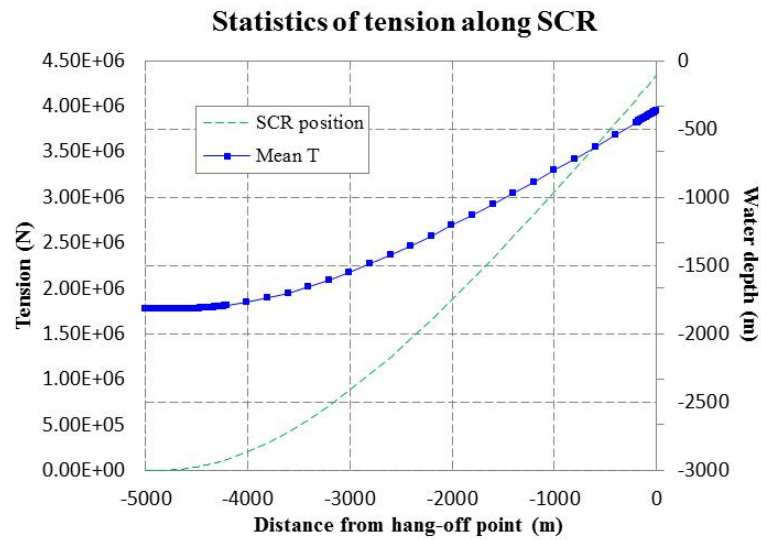|	Max	Min	Mean	SD
X-dir coordinate (m)	-3228	-3228.3	-3228.1	0.0304
Y-dir coordinate (m)	0.3087	-0.5396	-0.0441	0.1269
Z-dir coordinate (m)	-2991.5	-3000	-2998.4	1.2986
Tension (N)	2.61E+06	1.20E+06	1.83E+06	1.70E+05
Bending moment (N-m)	9.11E+03	4.61E+00	5.48E+03	702.3817

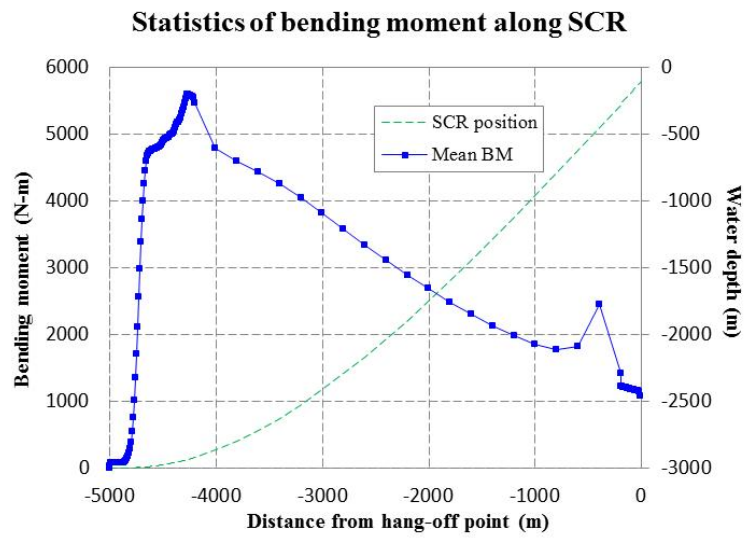**Figure 3.8   Mean tension along SCR near TDZ**

Figure 3.9   Mean bending moment along SCR near TDZ

51

The force components (Figures 3.5, 3.6 and 3.7) and motion characteristics (Figure 3.2, 3.3, 3.4) of SCR at TDZ were observed in the time series. The statistics data is tabulated in Tables 3.2 ~ 3.7. Figures 3.2 and 3.3 show that there are small and moderate variation of x and y directional displacements of nodes at TDZ. Evidence of pipeline walking and lateral buckling of SCR was not found in those time series analysis. With careful observation, it is noted that surge displacement of SPAR and vertical motion of nodes near TDZ show a good correlation. This can be geometrically explained. When the top of the catenary line is pulled horizontally away to the opposite direction of the anchor point along the line, there will be a vertical lifting force to the nodes that are lying on the seabed close to TDZ. In this manner, it is also possible to presume that heave displacement of SPAR has an effect on the horizontal motion of nodes near TDZ.

As shown in Figures 3.8 and 3.9, the variation of tension in the extended range is moderate through all measuring points which will make it possible to roughly presume the tension at the hang off point. Since the bending moment can be regarded to be proportional to the curvature of SCR, the results above indicate that the curvature should be very small on the seabed where it is near -5,000 m in Figure 3.9. Assuming the seabed is flat, lying SCR does not have curvature and the bending moment on the seabed should be zero. The curve in the plot shows bending moment decreases significantly near TDZ to the seabed.

3.1.3   Bending moment of SCR on seabed

For the purpose of analyzing the bending moment sensitivity to discretized element size, several combinations of SCR discretization are modeled for spar case and

compared as shown in Figures 3.10, 3.11 and 3.12. Discretization cases are two homogeneous lengths of element cases (40 elements with 125 m length and 125 elements with 40 m length) and one combined length of element case (120 elements with 10 m and 200 m length). As dynamic conditions, the maximum and minimum surge conditions of spar (which is the most significant motion responses among the axial displacement in the times series) are selected.
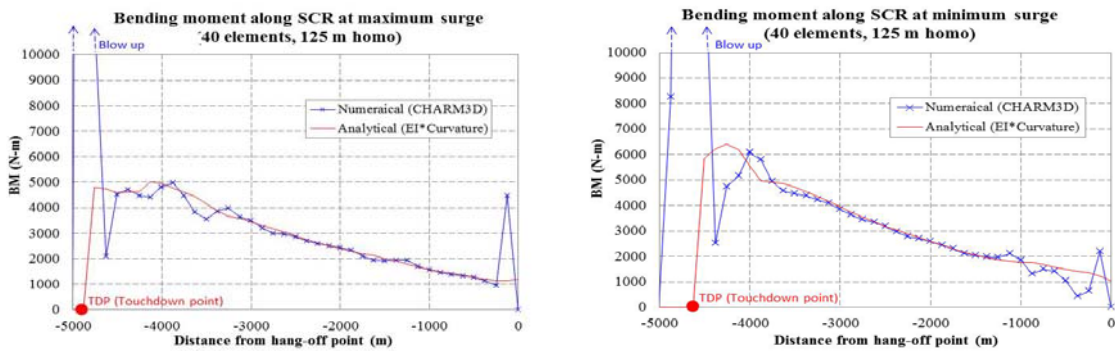
Figure 3.10 Discretization with 125 m length element
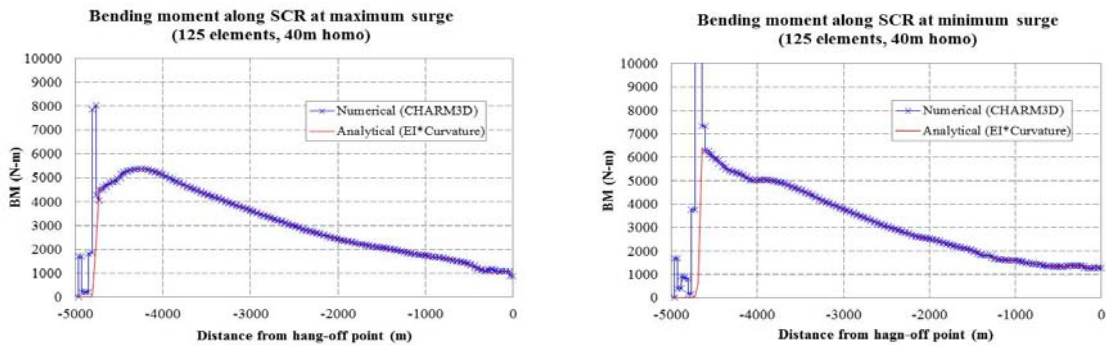
Figure 3.11 Discretization with 40 m length element
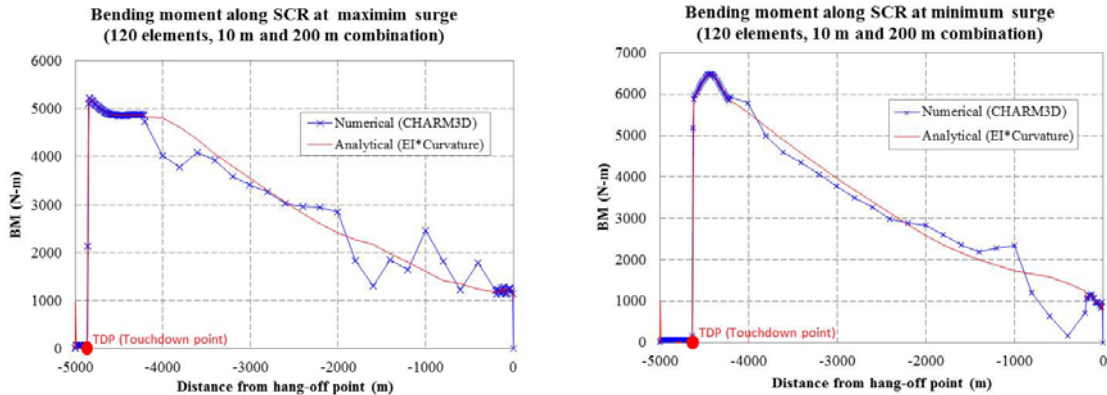
Figure 3.12 Discretization with 10 m and 200 m length elements

Figures 3.10, 3.11 and 3.12 commonly show that the bending moment from end point (-5,000 m in horizontal axis) to hang-off point (0 m in horizontal point) spikes at TDP and then increases shortly in the minimum surge case before it decreases, while it just decreases in the maximum surge case. In each comparison, the finer discretization part has better agreement between the analytical calculation and numerical calculation for bending moment. Especially on the seabed, bending moment calculated by the numerical method with 125 m length elements increases indefinitely, while the result of 10 m length elements shows good accordance between numerical and analytical results. In the case of discretization with a homogeneous 40 meters length of element, the bending moment obtained by the numerical method shows good coincidence with the analytical result throughout the ocean-piercing part of SCR. However, blow-up and fluctuation of numerically-obtained bending moment are mainly found from TDZ to the end point. The above results indicate that the numerical calculation is sensitive to

element size, especially on the seabed. The results also indicate a rough guideline for the minimum element size of SCR discretization.

At the minimum surge moment, the overall bending moment on SCR is higher than that at the maximum surge moment. Considering the configuration of connection between SCR and a floating production facility, at the minimum surge there is less tension on SCR which results in high bending moment.

3.1.4   SCR compression assessment

Based on the result of the time series on the spar case, there is no negative effective tension on SCR at TDZ as shown in Figure 3.13. That indicates there is no global buckling which is driven by negative effective tension on SCR in the time series of the spar case. Also, there is an estimation technique to assess negative effective tension without using the time series analysis; This often useful for the rough estimation of global buckling in the very beginning stage of SCR design. The estimation method is introduced in the following subchapter.
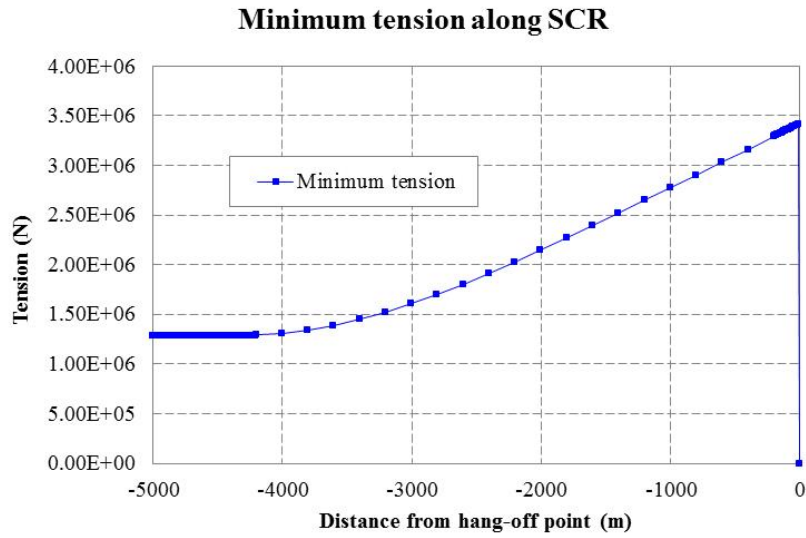
Figure 3.13 Minimum tension at each node along SCR

3.1.4.1   Correlation between hang-off velocity and SCR compression at TDZ
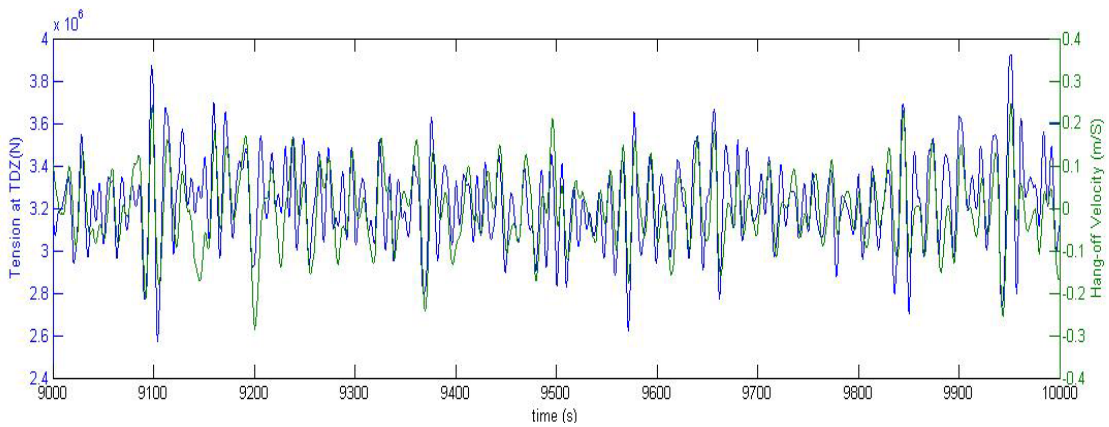
Figure 3.14 Tension at TDZ and heave velocity at hang-off point in time series

Cheng et al (2007) introduced the correlation between hang-off vertical velocity and the tension on SCR near TDZ. The time series of tension and heave hang-off

velocity in Figure 3.14 show that they are highly correlated. Figure 3.15 shows the maximum bending moment which is found right after the minimum effective tension near 9,100 seconds in the time series. This indicates that the maximum bending moment can be estimated not only from the effective tension but also from the velocity of the hang-off point.
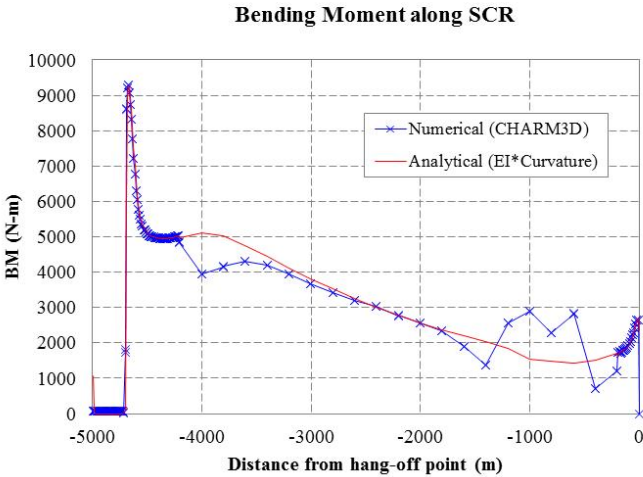
Figure 3.15 Maximum bending moment at TDZ in time series

3.1.4.2   Estimation of SCR compression from Hang-off velocity / Terminal velocity
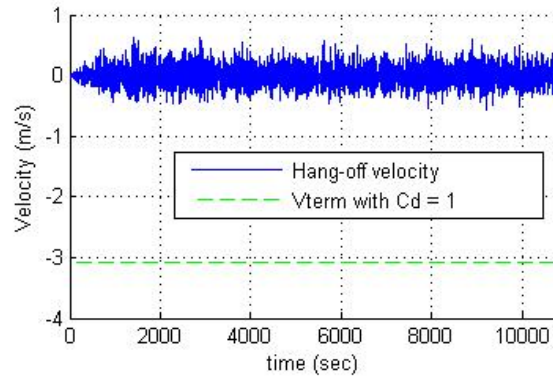
Figure 3.16 Hang-off velocity and terminal velocity

The vertical heave velocity of the hang-off point is compared with the terminal velocity which is obtained using the equation in 2.3.1. Based on the main particulars of SCR and 1 as the normal drag coefficient, the calculated terminal velocity for SCR in the spar case is 3.08 m/s to downward as shown in Figure 3.16. It is smaller than the minimum velocity of the hang-off point in the time series. This result of approximation indicates that there is no compression in SCR which can cause global buckling. However, global buckling is also caused by curvature and corresponding bending moment on SCR and so an assessment is required even if there is no compression.

3.1.4.3   Comparison of CHARM3D and other commercial software (OrcaFlex)

In order to show the reliability of CHARM3D, the result of analysis using other commercial software, OrcaFlex is compared with that of CHARM3D, based on identical environmental loads and a hull-riser-mooring model. The condition for the comparison

is the maximum bending moment at TDZ which was shown in Figure 3.15. The comparison of the results using the two programs is shown below (Figure 3.17).
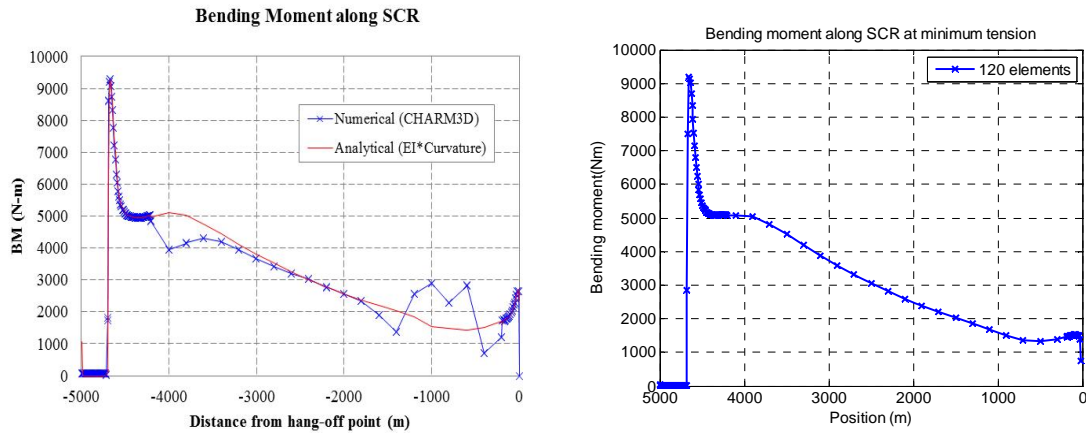
Figure 3.17 Max. BM at TDZ using CHARM3D (left) and OrcaFlex (right)

The analysis results for the maximum bending moment at TDZ using different programs (Charm3D and OrcaFlex) show that each bending moment along SCR has close peak value and tendency. However, where a coarse element is used for the discretization, discrepancies are found between the results from analytical and numerical results.

3.1.5   Global buckling assessment

In the spar case, SCR does not show upheaval direction of dynamics at TDZ and there is only lateral motion on the seabed. Therefore among the scenarios for global buckling assessment, a scenario of exposed pipeline on an even seabed is selected.

3.1.5.1 Scenario 1: Exposed pipeline on even seabed
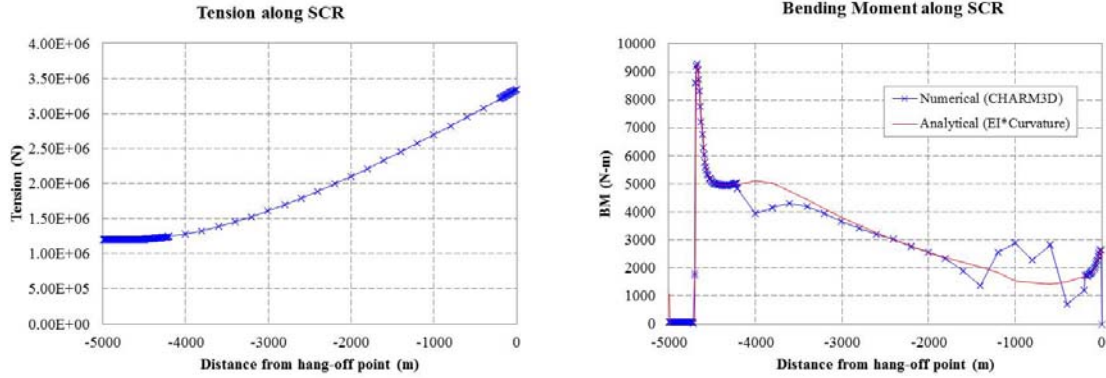
Figure 3.18 Tension and bending moment at maximum bending moment

Table 3.8   The variables of Figure 2.9 at maximum BM on SCR (spar)

Variable	Description	Number (unit)
$S(op)$	Compressive effective axial force	-1.20E+06 (N)
$R(op)$	radius of imperfection	1.20E+05 (m)
$S_\infty^{LB}(100)$	$2.29 \cdot \dfrac{EI}{\overline{L}^2}$	1.15E+07 (N)
$\overline{L}$	$\left[\dfrac{(EI)^2}{\left(f_L^{LB}\right)^2 \cdot E \cdot A_s}\right]^{0.125}$	2.673 (m)
f_L^{LB}	Lower bound lateral soil resistance force	4.50E+01 (N)
$S(R)^{LB}(100)$	$f_L^{LB} \cdot R(op)$	5.40 E+06 (N)
$R_\infty^{LB}(100)$	$2.41 \cdot (D-t) \cdot \sqrt{\dfrac{E \cdot t}{f_L^{LB}}}$	5.86E+02 (m)
k_{mb}	factor	1.5

60
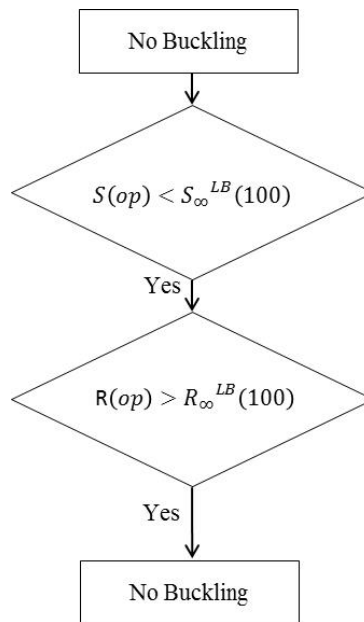
Figure 3.19 Flowchart for global buckling assessment at maximum BM

Figure 3.18 shows the tension and the bending moment at the maximum bending moment condition. Table 3.8 shows the input data for the variables of flowchart which is used for assessment of global buckling. Based on those variables, Figure 3.19 is obtained as the result of the assessment. It is found that there is no global buckling when the maximum bending moment occurs with the spar model. Considering there is no compression on SCR in the time series, neither tension nor bending moment causes global buckling on SCR with the spar model.

3.2 FPSO system

3.2.1 Time series analysis on FPSO

In this chapter, a time series analysis of FPSO and a Steel Catenary Riser (SCR) model is performed using CHARM3D. Environmental conditions are identical with the spar system and in order to simulate the head sea, the direction of every environmental load is expressed as 180 degrees. The corresponding displacements of FPSO in the time series follow this standard of direction so that the sign of displacement in the horizontal direction becomes the opposite of the case of the spar. Also, in order to remove the ramping effect the resulting statistics of the result of time series are tabulated except for the data of the first 1,000 seconds.
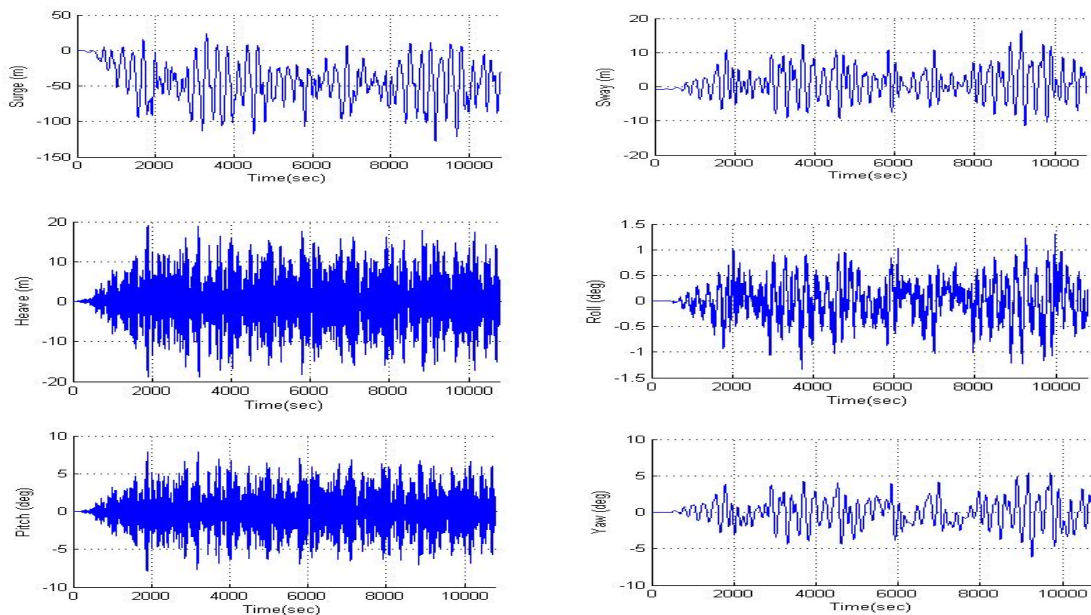
Figure 3.20 Time series of 6DOF motions of FPSO

Table 3.9   Displacement statistics from 1,000 sec to 10,800 sec in time series

	Max	Min	Mean	SD
Surge (m)	23.3443	-127.29	-46.63	28.2786
Sway (m)	16.4548	-11.398	1.157	4.6301
Heave (m)	19.1286	-18.906	-0.0038	6.1424
Roll (deg)	1.3044	-1.3432	0.0058	0.3902
Pitch (deg)	7.908	-7.8831	0.011	2.4674
Yaw (deg)	5.3788	-6.1272	-0.0397	1.9466

Three hours of time series analysis on FPSO motion were performed. The dynamics and statistic data of the displacement is tabulated in Figure 3.20 and Table 3.9. Considering the ramping effect, the first 1,000 seconds in the time series are excluded in the statistics. Comparing the results of motion analysis of FPSO with that of spar, it is noticeable that the mean surge displacement of FPSO is less than thirty percent of the mean surge displacement of spar. Considering that the environmental loads in the two cases are identical, the projected area of both floating production facilities to wave, current and wind can be one of the main reasons for the difference in amplitude. The most significant motion in the FPSO time series is the heave motion which has more than ten times the standard deviation of the spar case. Unlike the spar platform, the natural period of FPSO is subject to the dominant wave energy from the peak period of exciting waves. Therefore compared to the motions of spar, FPSO has larger heave and pitch motion response because of the resonance with the wave load. Also, the origin of body coordinate of FPSO is located in the center of the turret at mean water level so it is not necessary to consider the pitch motion for the heave motion of the hang-off point.

3.2.2   Time series analysis of SCR near TDZ

For the analysis of SCR at TDZ, one SCR and six nodes of the SCR near the TDZ were chosen for the time series analysis as tabulated in the following subsection. Among the 6-modes displacement of nodes, the most significant motion driven by the FPSO motion in the time series should be found in the vertical direction. Therefore heave displacement, tension, and bending moment are analyzed respectively for each node and the statistics data is tabulated in the following subsections. Also tensile stress and bending stress are investigated on three nodes near TDZ for further investigation of pipe integrity.
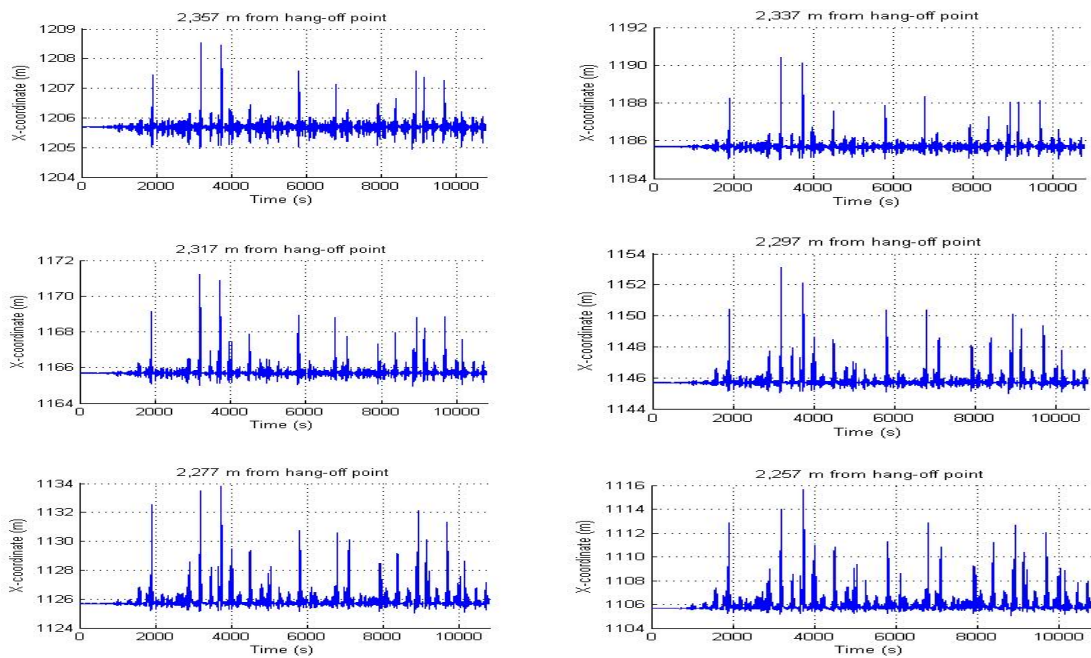
Figure 3.21 X-directional displacement of nodes over SCR near TDZ
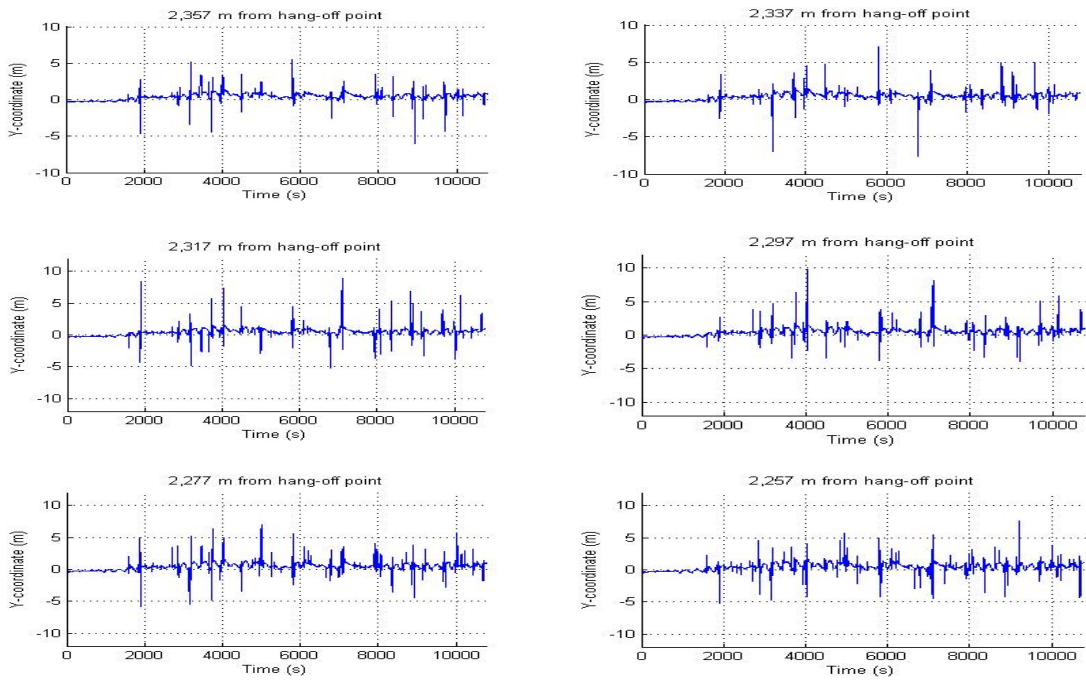
Figure 3.22 Y-directional displacement of nodes over SCR near TDZ
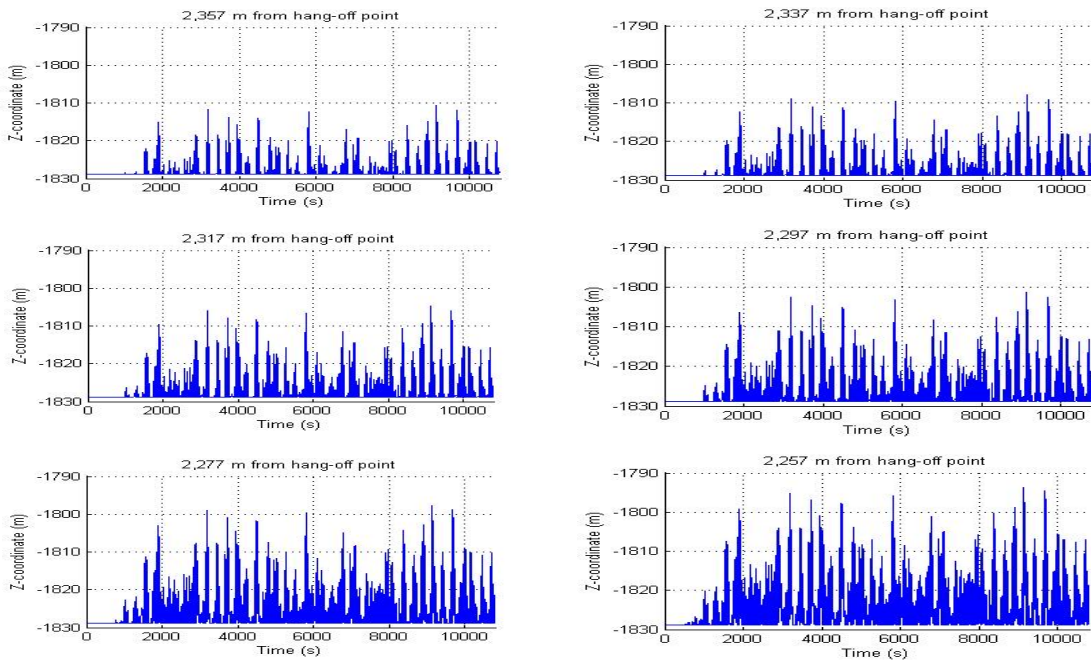
Figure 3.23 Z-directional displacement of nodes over SCR near TDZ
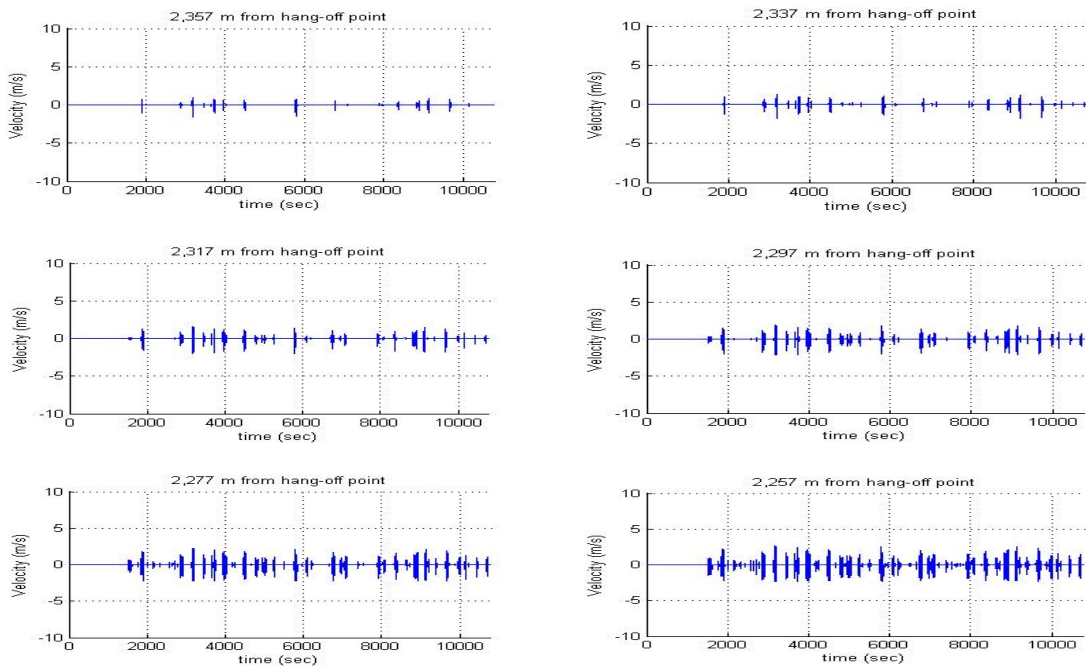
Figure 3.24 Vertical velocity of nodes over SCR near TDZ
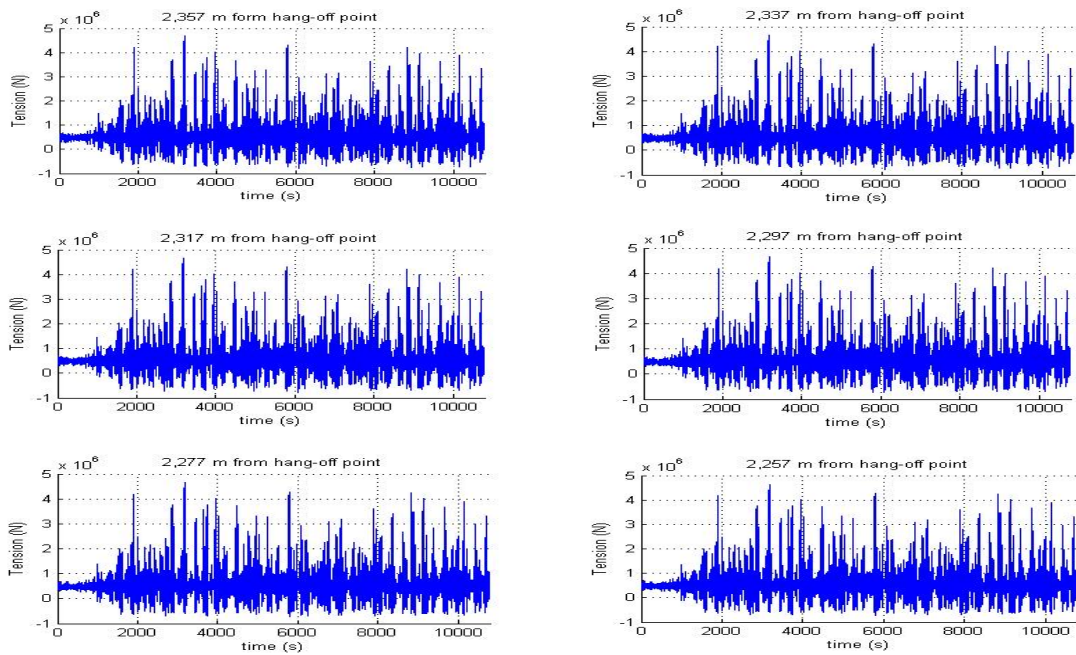
Figure 3.25 Tension at nodes over SCR near TDZ
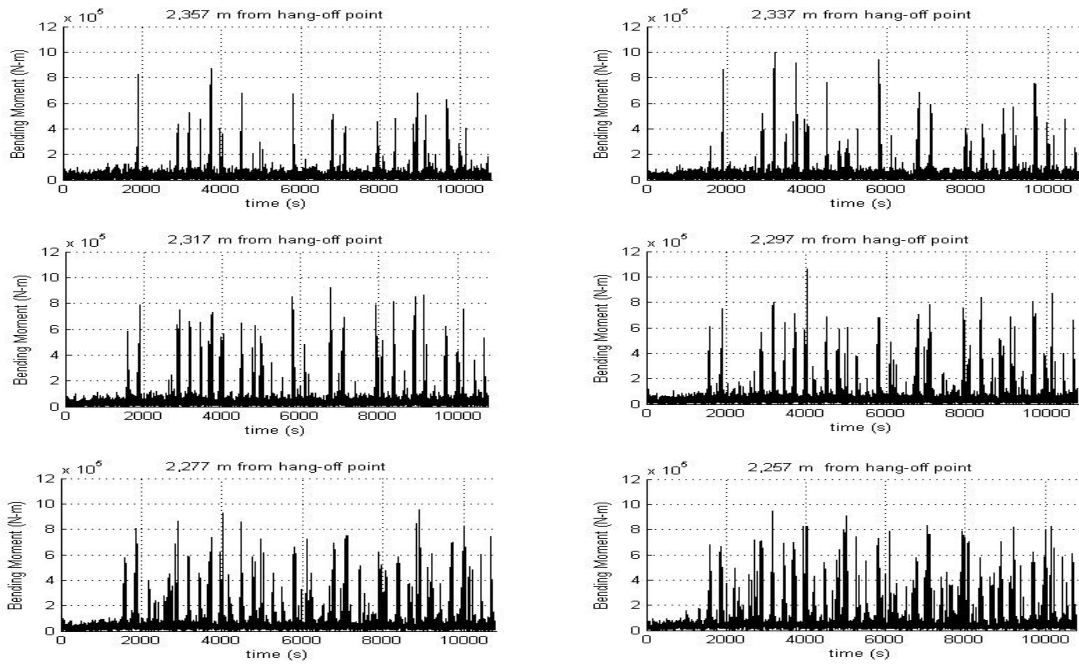
Figure 3.26 Bending moment at nodes over SCR near TDZ
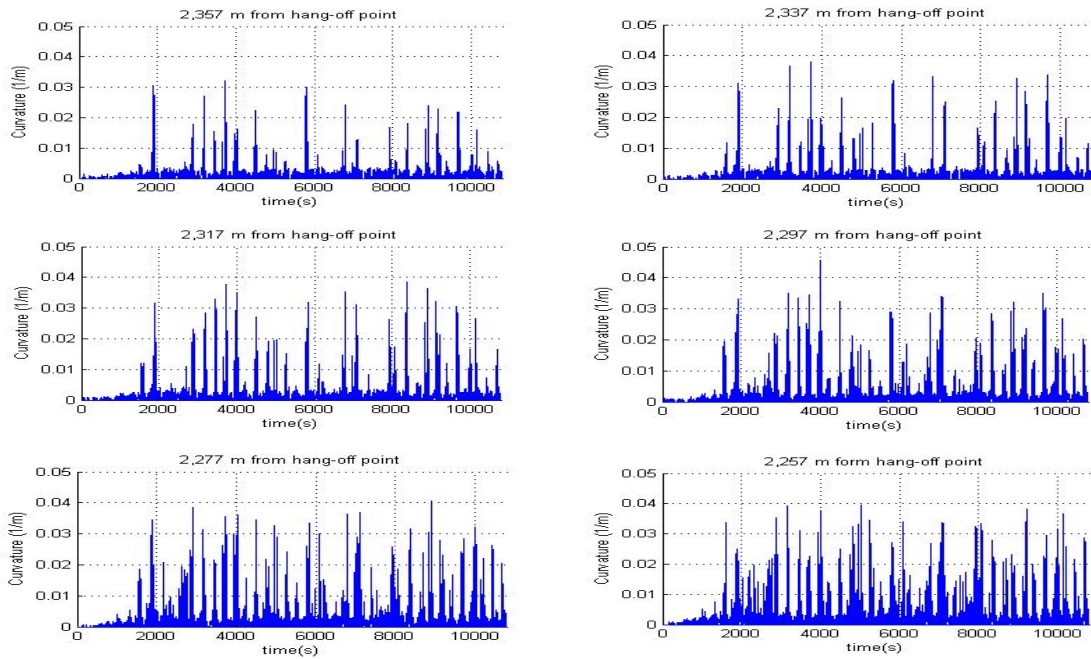
Figure 3.27 Curvature at nodes over SCR near TDZ
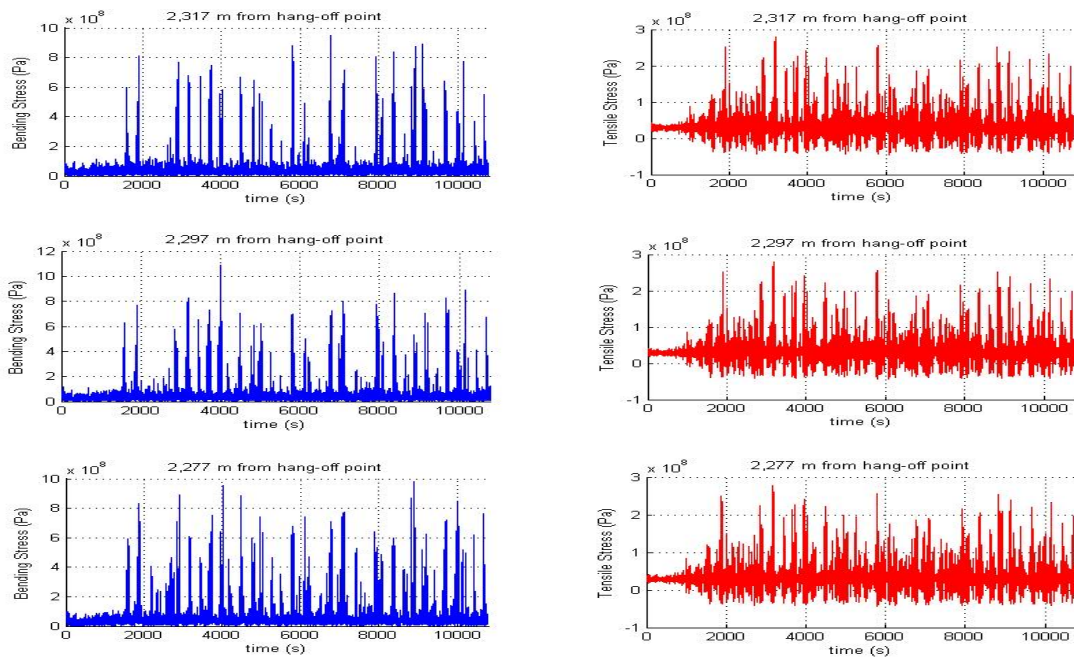
Figure 3.28 Bending stress and tensile stress at nodes over SCR near TDZ

Table 3.10   Statistics of time series on the node at 2,357 m from hang-off point

	Max	Min	Mean	SD
X-dir coordinate (m)	1.21E+03	1.21E+03	1.21E+03	0.2148
Y-dir coordinate (m)	5.5356	-5.992	0.4858	0.4641
Z-dir coordinate (m)	-1810.7	-1828.9	-1828.1	1.9726
Z-dir velocity (m/s)	0.918	-1.585	0	0.0565
Curvature (1/m)	3.22E-02	1.84E-21	7.61E-04	2.40E-03
Tension (N)	4.68E+06	-7.86E+05	5.94E+05	6.49E+05
Bending moment (N-m)	8.72E+05	2.91E+02	3.86E+04	5.46E+04

Table 3.11   Statistics of time series on the node at 2,337 m from hang-off point

	Max	Min	Mean	SD
X-dir coordinate (m)	1.19E+03	1.19E+03	1.19E+03	0.2913
Y-dir coordinate (m)	7.1093	-7.5918	0.4972	0.4865
Z-dir coordinate (m)	-1807.8	-1828.8	-1827.8	2.562
Z-dir velocity (m/s)	1.218	-1.846	0	0.0876
Curvature (1/m)	3.79E-02	3.82E-21	8.94E-04	2.80E-03
Tension (N)	4.67E+06	-8.01E+05	5.94E+05	6.49E+05
Bending moment (N-m)	1.00E+06	4.00E+02	4.12E+04	6.36E+04

Table 3.12   Statistics of time series on the node at 2,317 m from hang-off point

	Max	Min	Mean	SD
X-dir coordinate (m)	1.17E+03	1.17E+03	1.17E+03	0.367
Y-dir coordinate (m)	8.8953	-5.1696	0.5139	0.6178
Z-dir coordinate (m)	-1804.7	-1828.9	-1827.2	3.2663
Z-dir velocity (m/s)	1.535	-2.053	0	0.1314
Curvature (1/m)	3.84E-02	4.90E-21	1.10E-03	3.40E-03
Tension (N)	4.67E+06	-7.78E+05	5.95E+05	6.49E+05
Bending moment (N-m)	9.23E+05	1.73E+02	4.62E+04	7.90E+04
Tensile stress (Pa)	2.79E+08	-4.66E+07	3.56E+07	3.89E+07
Bending stress (Pa)	9.48E+08	1.77E+05	4.75E+07	8.11E+07

Table 3.13   Statistics of time series on the node at 2,297 m from hang-off point

	Max	Min	Mean	SD
X-dir coordinate (m)	1.15E+03	1.15E+03	1.15E+03	0.4857
Y-dir coordinate (m)	9.8307	-3.9032	0.5364	0.5766
Z-dir coordinate (m)	-1801.3	-1828.9	-1826.4	4.1208
Z-dir velocity (m/s)	1.873	-2.119	0	0.1857
Curvature (1/m)	4.57E-02	2.79E-21	1.30E-03	3.60E-03
Tension (N)	4.66E+06	-7.28E+05	5.96E+05	6.49E+05
Bending moment (N-m)	1.06E+06	9.30E+02	4.90E+04	8.10E+04
Tensile stress (Pa)	2.79E+08	-4.36E+07	3.57E+07	3.89E+07
Bending stress (Pa)	1.09E+09	9.56E+05	5.03E+07	8.33E+07

Table 3.14   Statistics of time series on the node at 2,277 m from hang-off point

	Max	Min	Mean	SD
X-dir coordinate (m)	1.13E+03	1.13E+03	1.13E+03	0.618
Y-dir coordinate (m)	7.038	-5.9036	0.5512	0.6151
Z-dir coordinate (m)	-1797.7	-1828.9	-1825.3	5.0777
Z-dir velocity (m/s)	2.234	-2.258	0	0.2575
Curvature (1/m)	4.06E-02	2.26E-21	1.50E-03	4.00E-04
Tension (N)	4.65E+06	-7.37E+05	5.97E+05	6.49E+05
Bending moment (N-m)	9.55E+05	4.02E+02	5.41E+04	8.89E+04
Tensile stress (Pa)	2.79E+08	-4.41E+07	3.57E+07	3.88E+07
Bending stress (Pa)	9.81E+08	4.13E+05	5.56E+07	9.13E+07

Table 3.15   Statistics of time series on the node at 2,257 m from hang-off point

	Max	Min	Mean	SD
X-dir coordinate (m)	1.12E+03	1.11E+03	1.11E+03	0.7613
Y-dir coordinate (m)	7.6571	-5.2399	0.5429	0.5925
Z-dir coordinate (m)	-1793.6	-1828.9	-1823.7	6.1049
Z-dir velocity (m/s)	2.62	-2.359	0	0.3466
Curvature (1/m)	3.94E-02	1.37E-21	1.80E-03	4.30E-03
Tension (N)	4.64E+06	-7.42E+05	5.98E+05	6.48E+05
Bending moment (N-m)	9.49E+05	2.90E+02	5.78E+04	9.41E+04
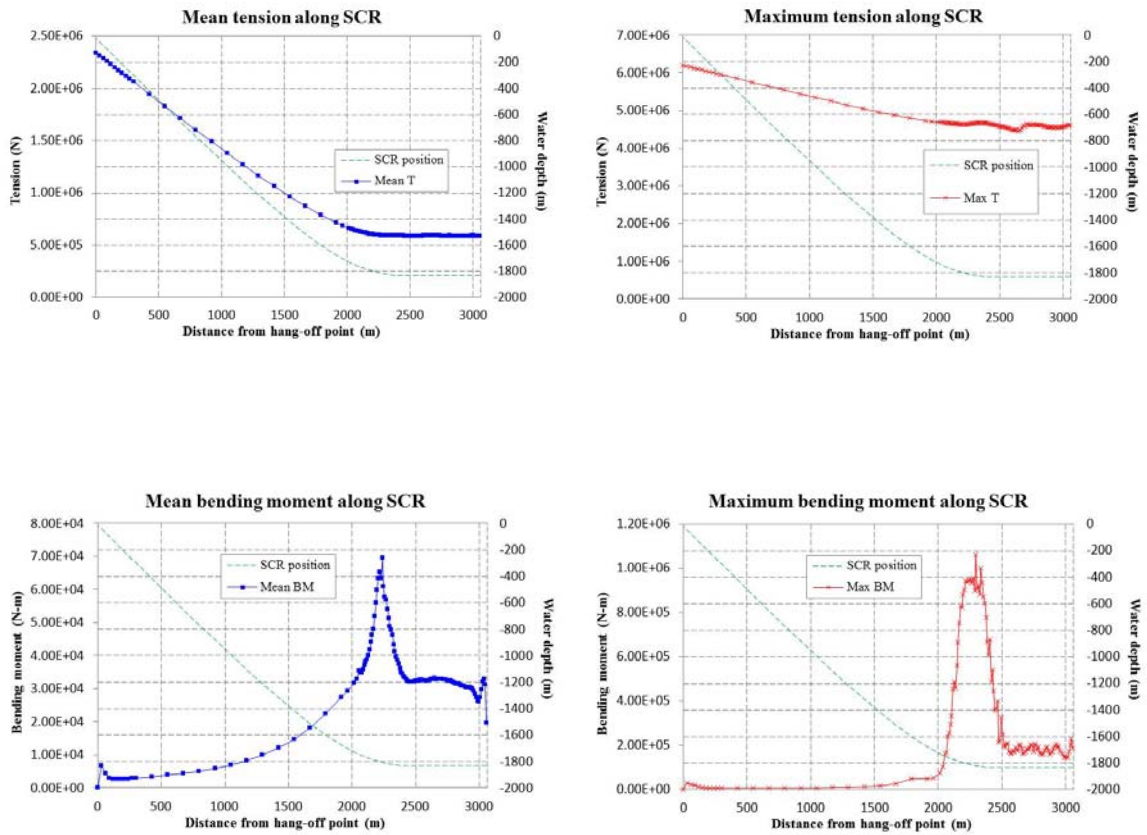
Figure 3.29 Statistics of force components at nodes along SCR
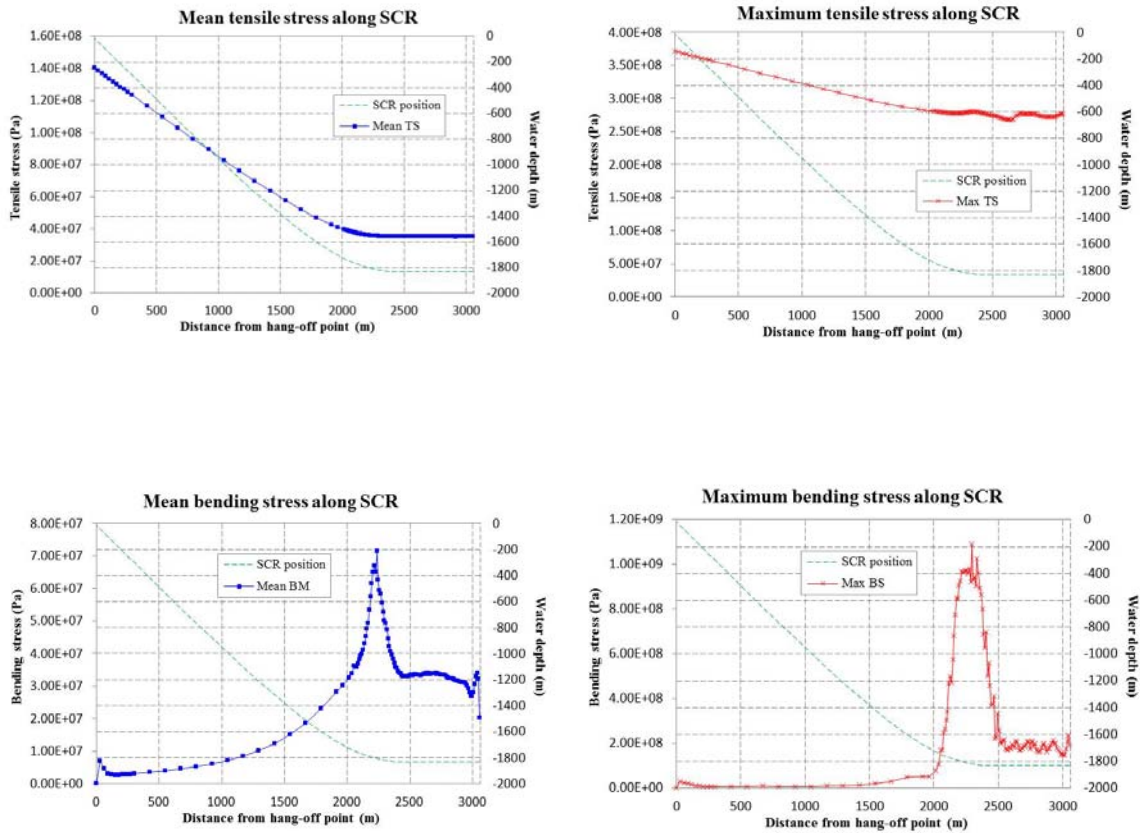
Figure 3.30 Statistics of stress components at nodes along SCR

Force components (Figures 3.25, 3.26, 3.27 and 3.28) and behavioral characteristics (Figures 3.21, 3.22, 3.23 and 3.24) of SCR at TDZ were analyzed in the time series. Tables 3.10 ~ 3.15 and Figures 3.29 and 3.30 show the statistics of time series analysis. The displacements of nodes in the x-direction and y-direction show moderate and small motions of nodes over the time series while several cycles of sudden large displacements were also observed. The sudden large y-directional displacements represent the lateral buckling since those cycles of displacement responses have clear

correlation with the cycles of negative and positive axial tensions of SCR at same positions. As shown in the time series of node heave motions near TDZ, the magnitude of heave at TDZ is approximately three times greater than the nodes in the SPAR case. This resulted from the large heave motion of the FPSO tanker which leads to the following large magnitude of tension variation as shown in the time series analysis in tension near TDZ. Particularly, the negative tension observed near TDZ is one of the important driving factors of global buckling. Bending moment in the time series is also much greater than the maximum peak values of the spar case. As shown in Figure 2.7, curvature is calculated based on the coordinates of nodes and the tangent vector at each end of an element. Linear calculation for the bending moment is possible from the multiplication of curvature and EI of SCR which is called analytical method for the bending moment calculation in this study. Based on the result of time series analysis, curvatures of the selected nodes over SCR at TDZ were found highly correlated with bending moment at the same positions.

Tensile stress and bending stress were also investigated. The result of investigation indicates that bending stress is generally larger than tensile stress. This result is discussed again in the pipe integrity part.

3.2.3   Bending moment on SCR

3.2.3.1   Analytical and Numerical methods

As described in Figure 2.7, the multiplication of curvature of nodes and constant bending stiffness is the analytical method used for the bending moment calculation.

Since curvature is obtained based on the geometric data of nodes, bending moment calculated by the analytical method is less sensitive to the length of the element than the numerical method. For example, when multiple numbers of elements are connected as shown in Figure 3.31, the analytical method assumes curvature based on the coordinate data and multiplies the reciprocal of the radius of curve and bending stiffness to obtain bending moment. On the other hand, the numerical method of CHARM3D divides a discretized element into a constant number of smaller elements to calculate bending moment. Therefore the numerical method means coarser discretization than the analytical method and the corresponding result is also less correct than the analytical method. API RP 2RD recommends discretization with a finer element size near TDZ which emphasizes the careful discretization of SCR necessary to avoid numerical errors.
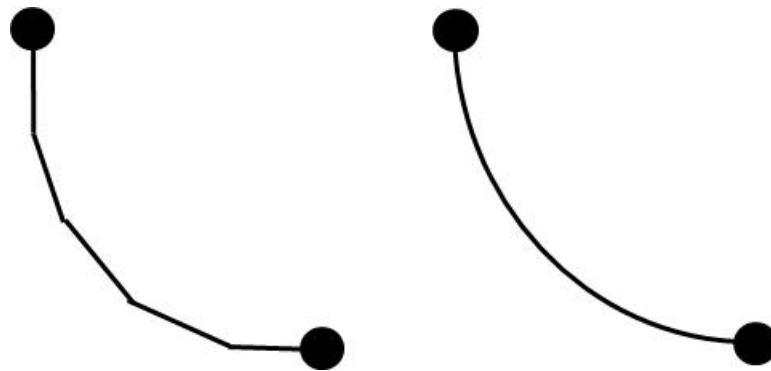
Figure 3.31 Numerical method (left) and analytical method (right)

3.2.3.2 Bending moment on seabed

In order to investigate the characteristics of bending moment on SCR near TDZ, the correlation between the bending moment on SCR and the displacement of FPSO is analyzed. As shown in Figure 3.32, the bending moment at the maximum and minimum heave motions of FPSO is checked to investigate the correlation between motion of the FPSO and bending moment on SCR at TDZ. After the correlation between FPSO heave displacement and bending moment on SCR is checked using the analytical method, the calculation results of bending moment by the analytical method and the numerical method are compared to check the SCR discretization with beam elements. Last, the maximum global bending moment in the time series analysis and the bending moment distribution along SCR are investigated to better understand the behavior of SCR at TDZ and the following buckling assessment.
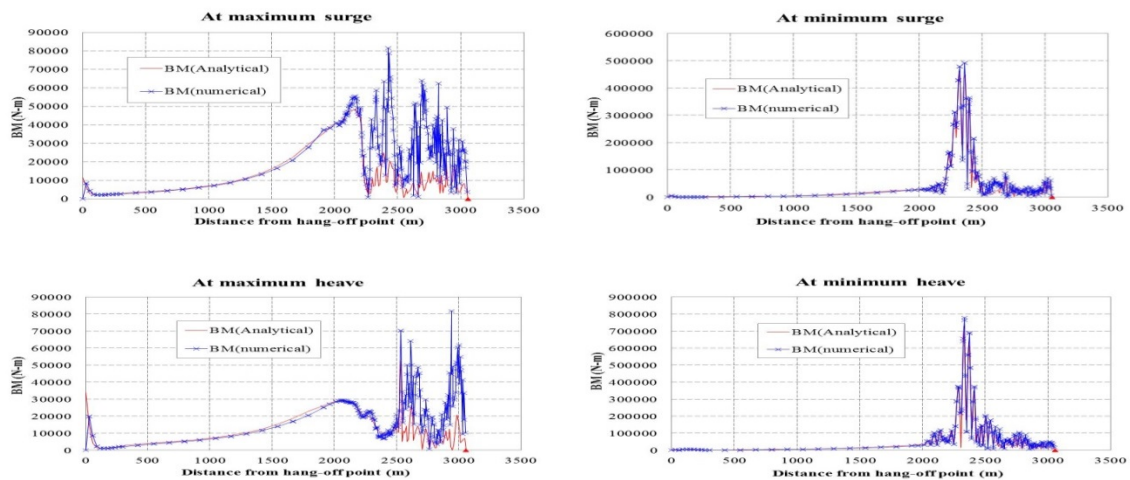
Figure 3.32 Bending moment at Max. and Min. surge and heave displacement

As shown in Figure 3.32, the bending moment on SCR near TDZ has a high correlation with heave and surge. Although the variation of heave motion is smaller than that of surge, the velocity of heave motion is larger than surge which explains a high correlation between the FPSO heave displacement and the bending moment at TDZ. Based on the result of analytical method, bending moment curve generally peaks near TDZ, between 2,200 m and 2,500m, and this leads to lateral buckling on the seabed, often causing global and local buckling.

A sensitivity check of the SCR element length to the calculated bending moment was also investigated in Figure 3.32. The numerical method for the calculation of bending moment with the combination of fine and coarse elements has a good agreement with the analytical method on a large scale (Maximum surge and minimum heave). Meanwhile, when the scale of the calculated bending moment is small, a discrepancy between the results of the two methods is observed.

The most efficient way to find the maximum bending moment using CHARM3D is to check the maximum bending moment of each node in the time series. The time series of the node is then observed to find when the maximum bending moment occurs. It is then possible to plot the bending moment distribution along SCR.
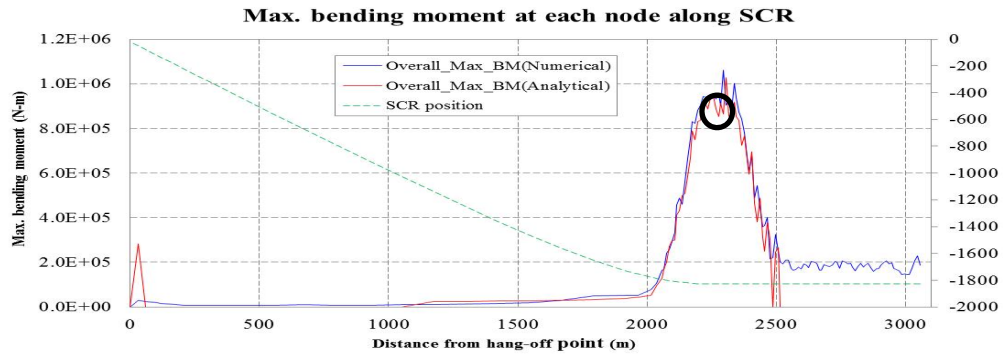
Figure 3.33 Maximum bending moment at each node along SCR
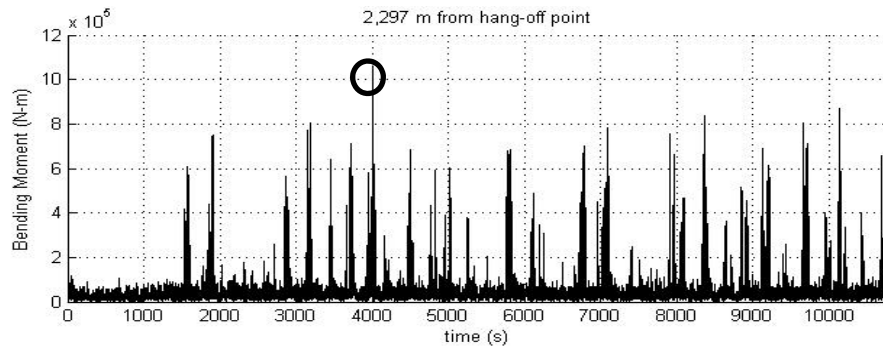
Figure 3.34 Maximum bending moment at TDZ
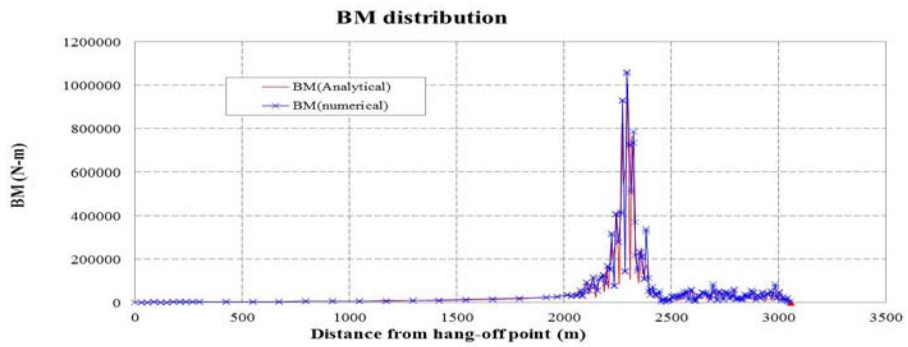
Figure 3.35 Bending moment along SCR at 4,017 sec in the time series

78

The maximum bending moment at each node along SCR and the corresponding time series at the position of maximum bending moment and the distribution at the instant are analyzed. From the maximum bending moment distribution as shown in Figure 3.33, it is possible to find the node which has the greatest bending moment in the time series. Accordingly, the time series analysis of the bending moment of the node (Figure 3.34) and the bending moment distribution along SCR when the node has the greatest bending moment (Figure 3.35) need to be investigated to confirm the position and time of maximum bending moment along SCR. It is also possible to find the minimum tension using a same manner as shown in Figures 3.36, 3.37 and 3.38.
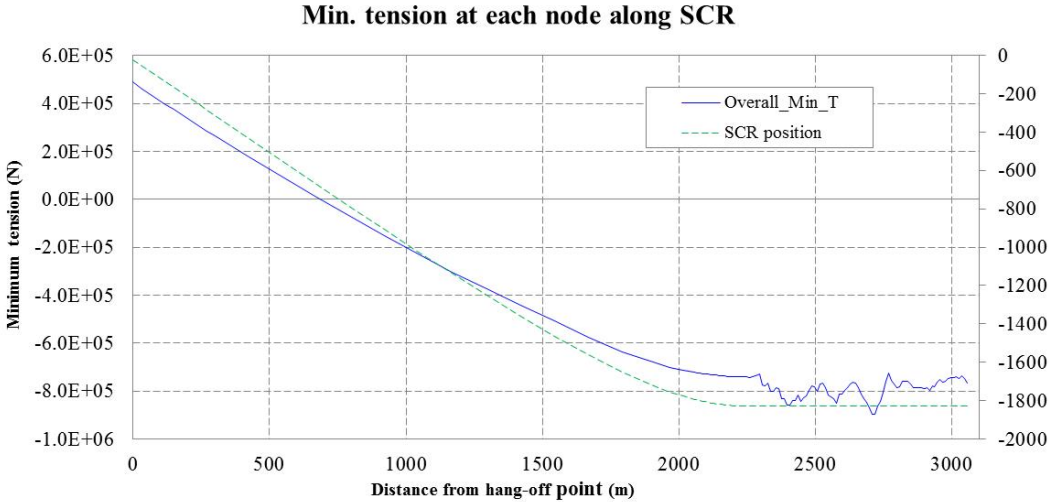
Figure 3.36 Minimum tension at each node along SCR
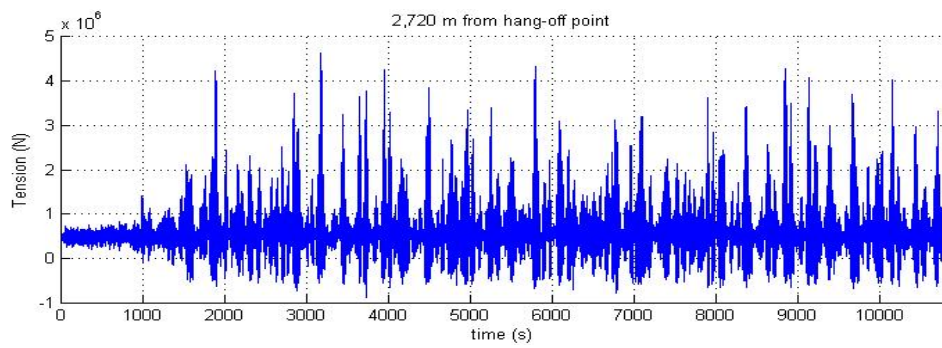
Figure 3.37 Minimum tension at TDZ
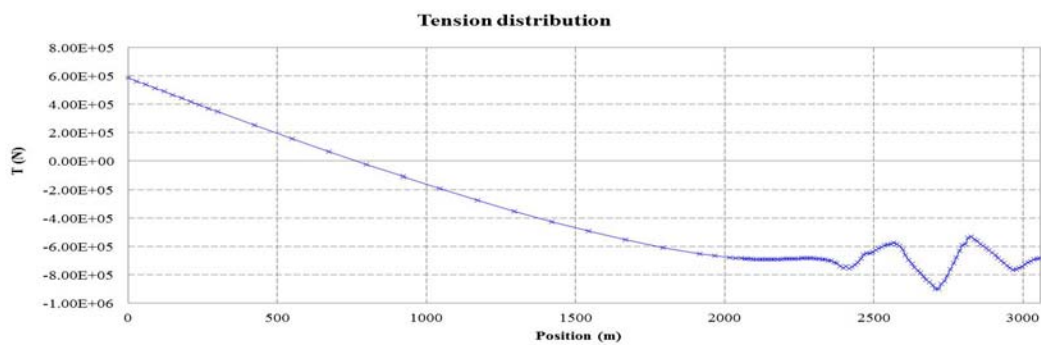
Figure 3.38 Tension at 3,737 sec in time series

3.2.4 SCR compression assessment

3.2.4.1 Correlation between hang-off velocity and SCR compression at TDZ
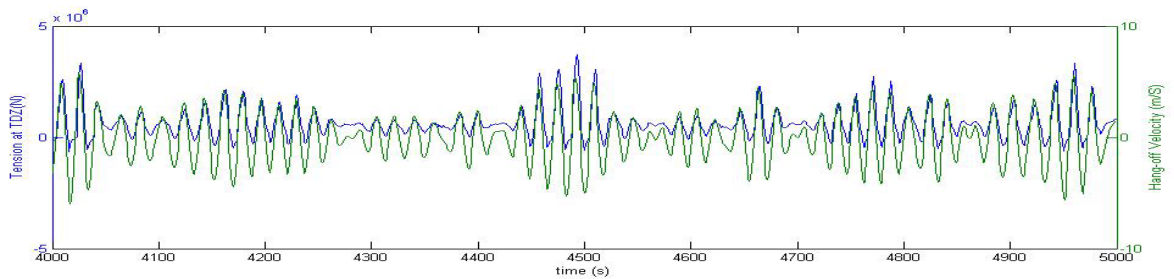
Figure 3.39 Tension at TDZ and hang-off heave velocity in time series

80

Figure 3.39 illustrates two different time series in 1,000-seconds in which effective tension and hang-off heave velocity are highly correlated with each other. However, it is difficult to estimate when the negative effective tension occurs in the time series from the heave velocity data of the hang-off point. In order to assess SCR negative tension, criteria for the FPSO heave velocity is required as introduced in the following subsection.

3.2.4.2   Estimation of SCR compression from Hang-off velocity / Terminal velocity
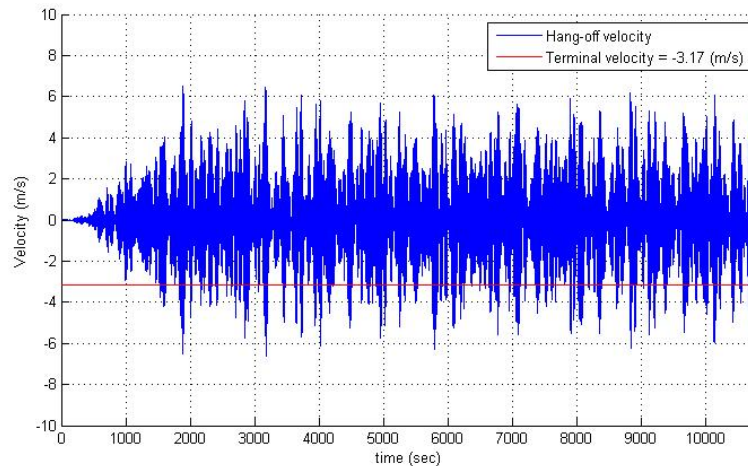
Figure 3.40 Partial time series of hang-off heave velocity and terminal velocity
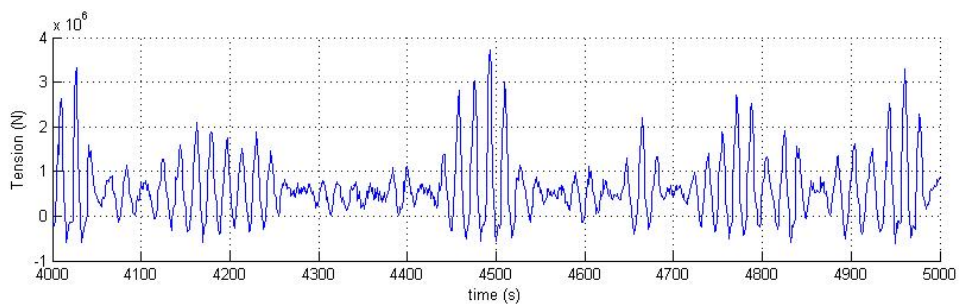
Figure 3.41 Partial time series of effective tension at TDZ

The compression load on SCR near TDZ and the vertical velocity are assessed using the time series analysis and equation which was introduced at 2.3.1. Figure 3.40 indicates that there are negative effective tensions on SCR in the time series. Figures 3.40 and 3.41 show that the parameter using the hang-off velocity and terminal velocity have a fairly good agreement with the actual measurement result obtained by CHARM3D. However, with this method, it is difficult to accurately estimate the negative tension near TDZ as well as the curvature of SCR at TDZ. After all, the parameter composed of terminal velocity and hang-off velocity can be used to assess the possibility of SCR compression; but for further investigation the time series analysis of tension and bending moment requires a reliable program such as CHARM3D.

3.2.4.3   Comparison of CHARM3D and other commercial software (OrcaFlex)

The result of analysis using other commercial software, OrcaFlex, based on identical environmental loads and the hull-riser-mooring model is compared with that of CHARM3D. In this subchapter, the maximum bending moments at each node in the time series are compared with each other as shown in Figure 3.42.
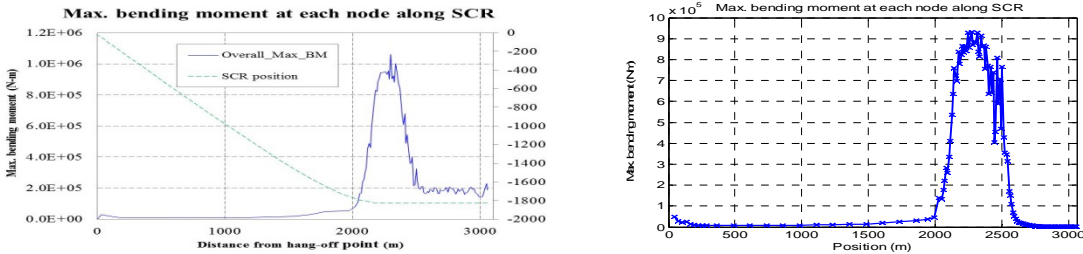
Figure 3.42 Max. BM at TDZ using CHARM3D (left) and OrcaFlex (right)

The analysis results for the maximum bending moment at each node in the time series using different programs (Charm3D and OrcaFlex) show that each bending moment along SCR has a close peak value (1.0E+06 and 0.9E+06) and similar tendency along SCR. However, in the CHARM3D result, bending moment on the seabed is approximately 2.0E+05 (N-m), while the result of OrcaFlex is nearly 0. The result of CHARM3D indicates the curvature of SCR is observed along the seabed. The seabed stiffness model of OrcaFlex is linear while that of CHARM3D is nonlinear (using quadratic-spring) which can explain the different seabed dynamics of SCR in each plot.

3.2.5 Pipe walking and lateral buckling

The global and local bucklings are both driven by the significant negative tension and lateral and upheaval motions of SCR near TDZ. The sequence of global buckling is initialized by negative effective tension which turns into the curvature on the seabed while the negative tension perishes. The curvature of SCR on the seabed is a result of the interaction between the SCR motion and seabed friction. CHARM3D applies the coulomb friction concept as the friction force in the seabed model. In this subsection, the correlation between the lateral buckling of SCR on the seabed and the motions of FPSO are investigated.
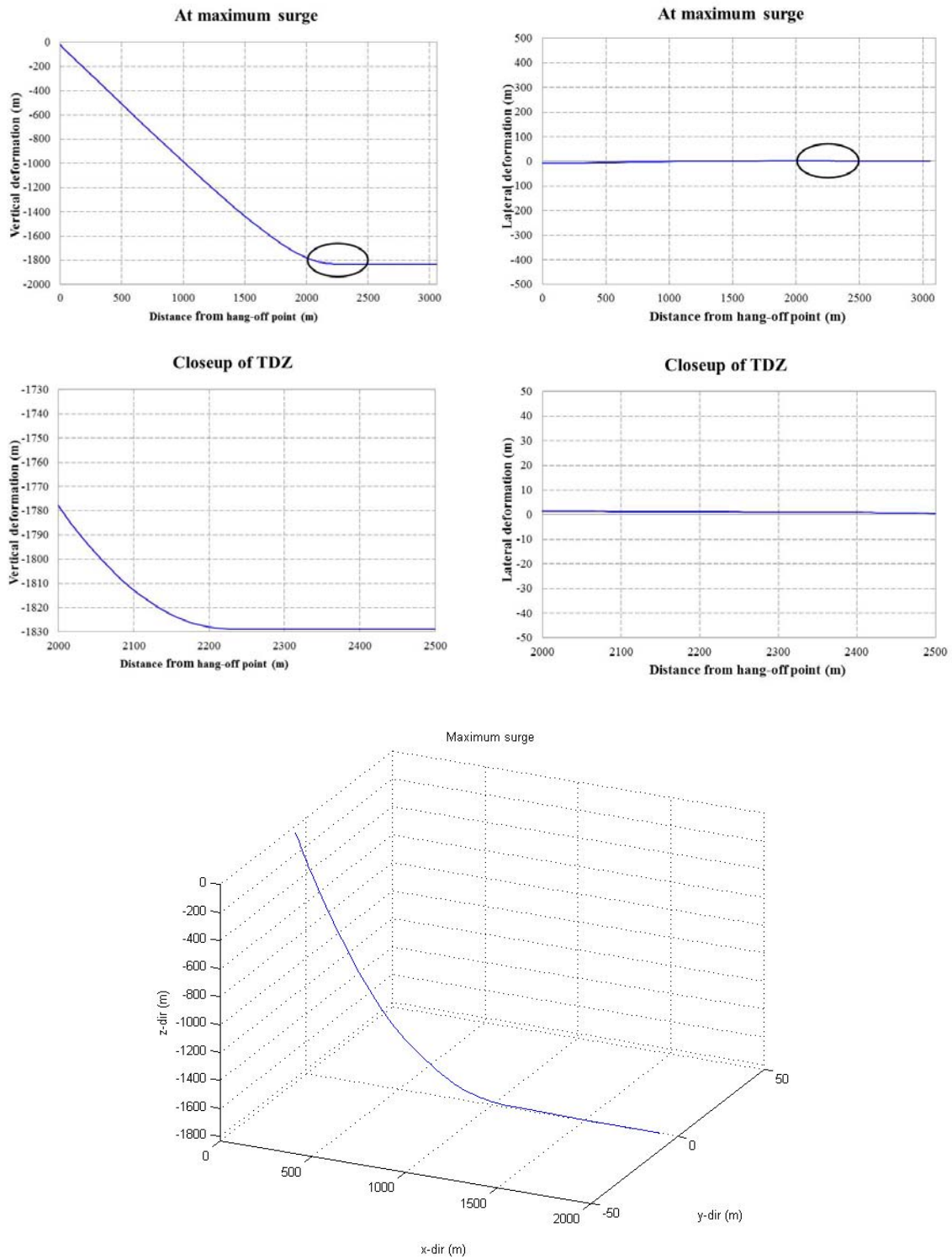
Figure 3.43 Lateral / Vertical projection of SCR at maximum surge displacement
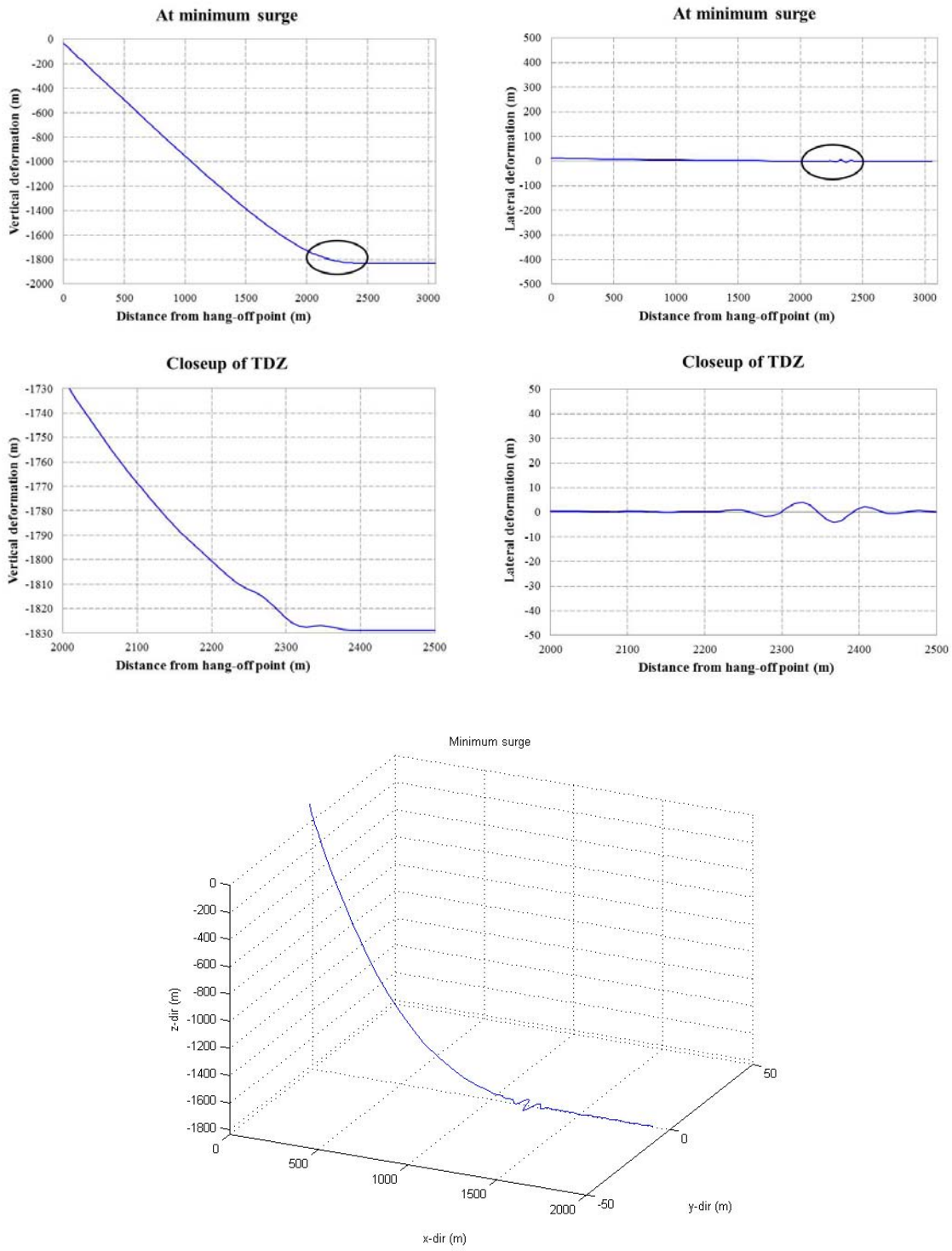
Figure 3.44 Lateral / Vertical projection of SCR at minimum surge displacement
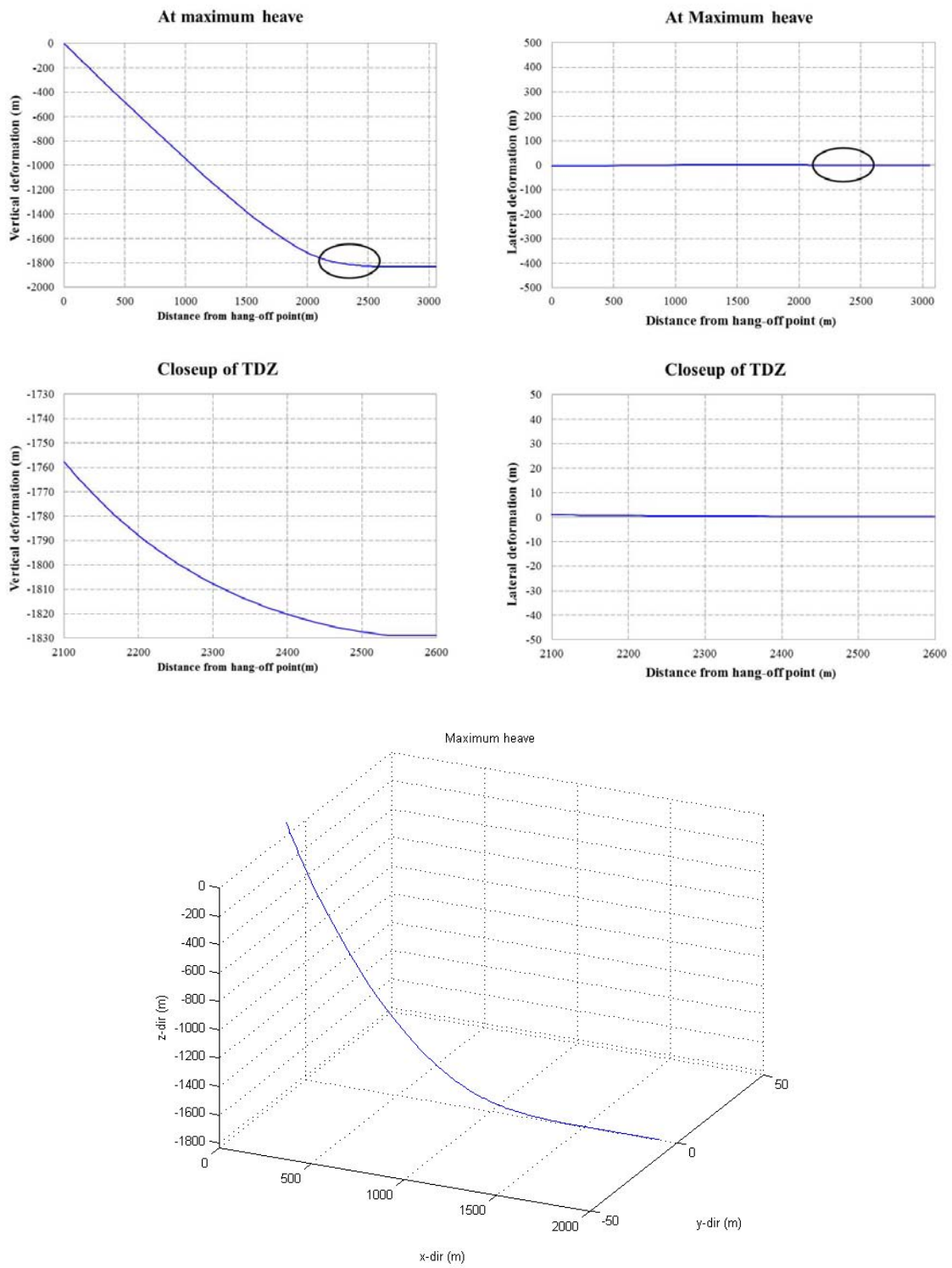
Figure 3.45 Lateral / Vertical projection of SCR at maximum heave displacement
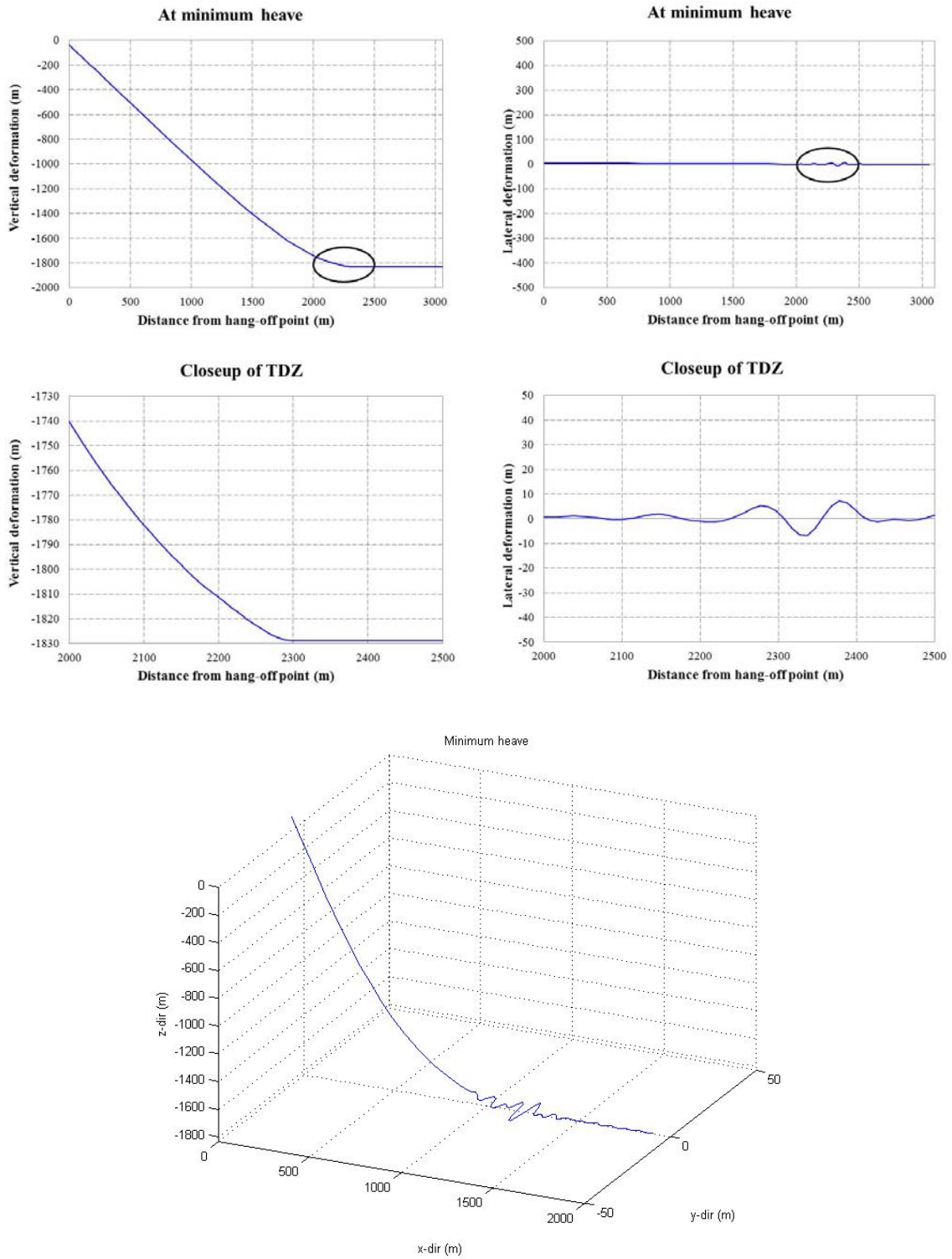
Figure 3.46 Lateral / Vertical projection of SCR at minimum heave displacement
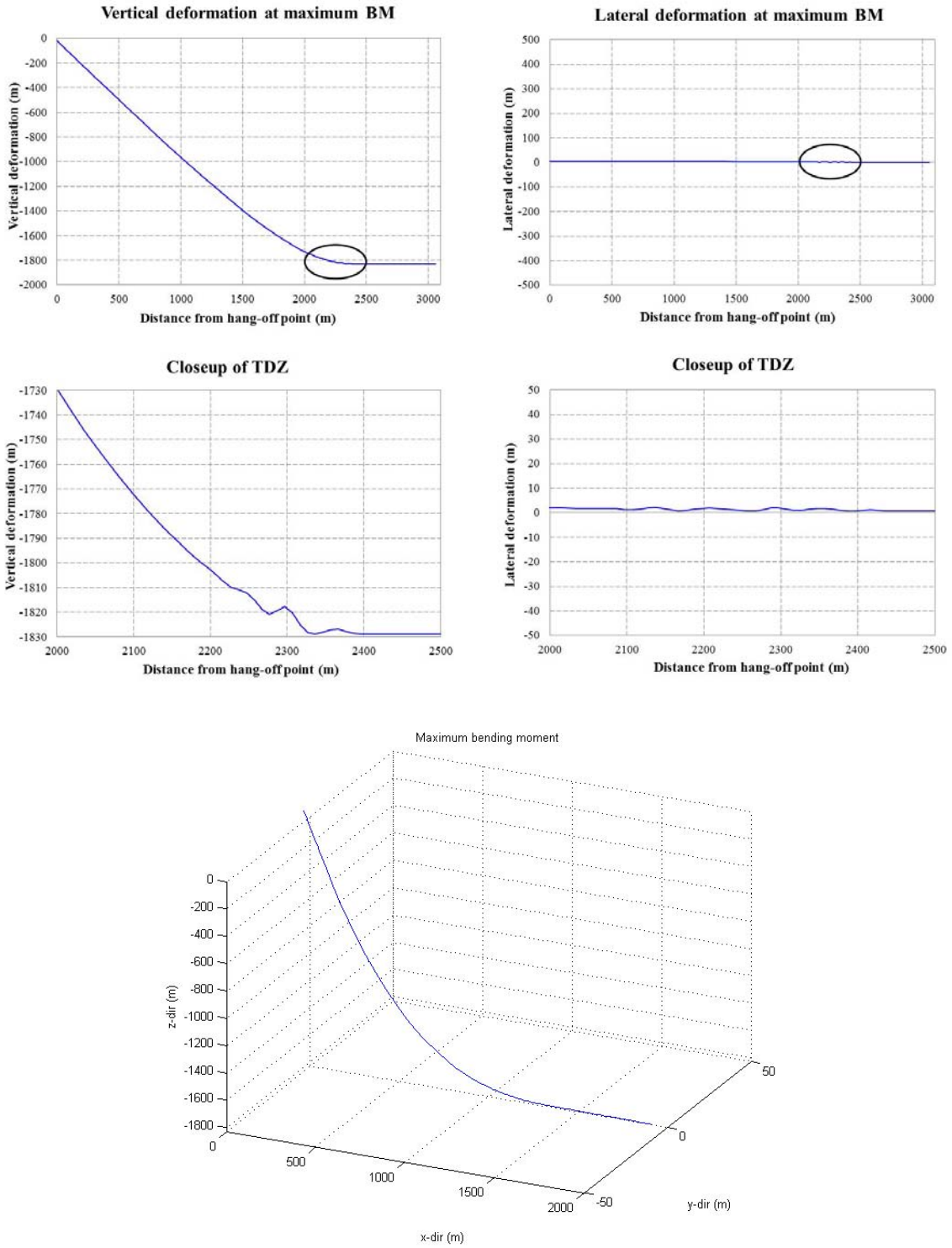
Figure 3.47 Lateral / Vertical projection of SCR at maximum bending moment

From the results of analysis on the lateral buckling of SCR at the maximum and minimum heave (Figures 3.43 and 3.44) and surge (Figures 3.45 and 3.46) displacement of FPSO, it was found that both the horizontal and vertical motions of FPSO are driving factors for lateral buckling of SCR. As shown in Figures 3.44 and 3.46, prominent lateral buckling is observed near TDZ at minimum heave and minimum surge displacement. This is readily explained by the geometric position of FPSO and SCR. When FPSO has a minimum heave displacement, the fairlead point has maximum draft and the downward displacement acts as a negative effective tension along SCR to the TDZ where the lateral buckling occurs as a result. Likewise, the nodes of SCR near TDZ repeatedly attach to and separate from the seabed at the minimum and maximum surge displacement of FPSO and cause a similar behavioral motion of SCR. These cycles not only cause the sequence of bending moment but also the compression and tension on SCR at TDZ.

The negative effective tension on SCR often turns into the upheaval motion of SCR at TDZ. The upheaval motion of SCR is found near the point of contact to the seabed and causes a significant amount of bending moment. Therefore it is important to pay more attention to the magnitude of bending moment than the scale of lateral buckling on the seabed for further investigation on buckling and integrity check. As shown in Figure 3.47, despite the small scale of lateral buckling, the upheaval displacement of SCR is significant at TDZ which results in the overall maximum bending moment at the position.

3.2.6 Seabed lateral friction model

The seabed model adopts coulomb friction to the horizontal direction and lateral damping to the normal direction of SCR element. In this study, only the coulomb friction with the coefficient 0.5 works against the lateral motion of SCR. Therefore it is possible to model the seabed by combining the coefficients of friction and damping. Three types of seabed model with lateral force are compared for the condition of minimum heave as shown below.
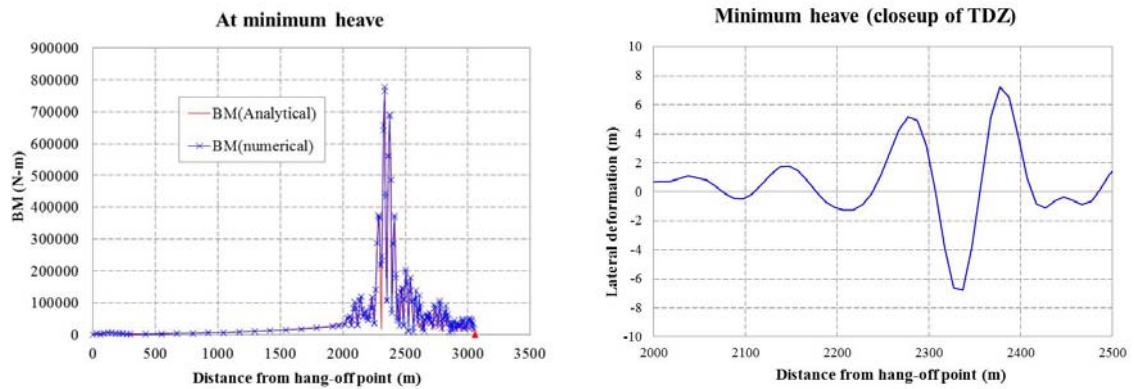
Figure 3.48 Seabed model with friction coefficient 0.5
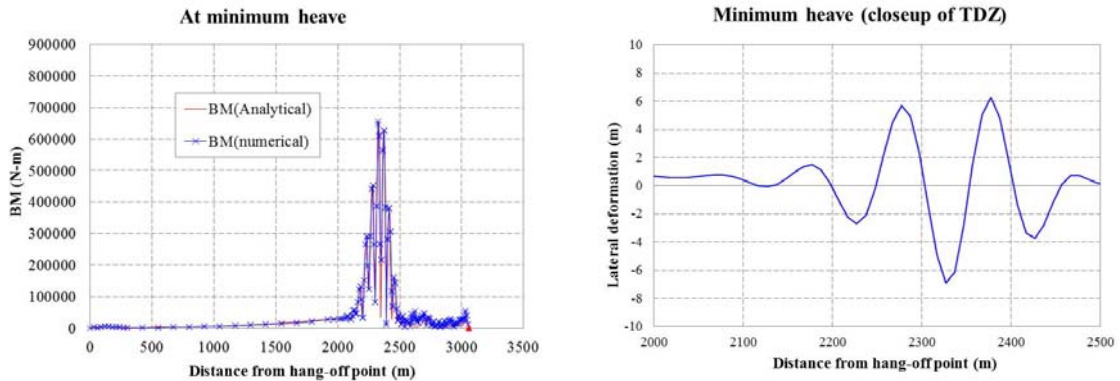
Figure 3.49 Seabed model with friction coefficient 0.5, damping coefficient 500
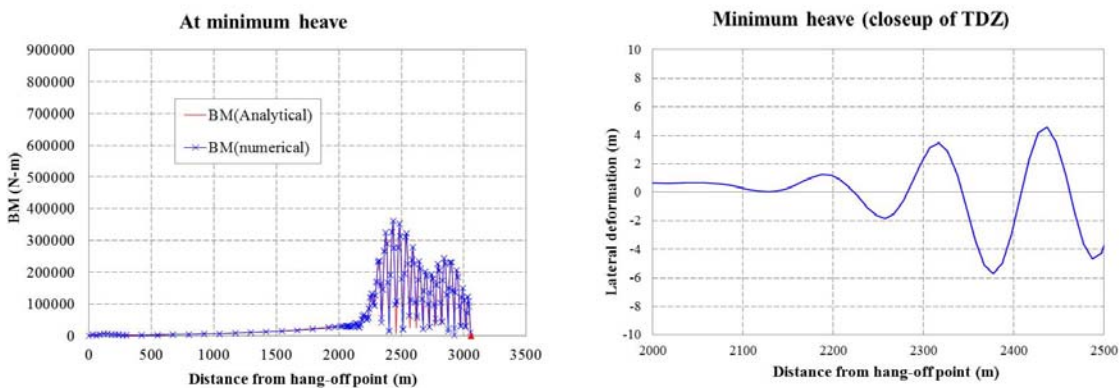
Figure 3.50 Seabed model with no coefficient and no damping

In Figure 3.50, overall bending moment on the seabed (2,100 m to 3,060 m from hang-off point) is found while in Figures 3.48 and 3.49 the bending moment is concentrated at near touchdown point (TDP). This indicates the friction model on the seabed keeps the negative tension (Compression) and bending moment of SCR from

91

moving to longitudinal direction to end point (3,060 m from hang-off point). Because of the lateral friction force on the seabed, the negative tension which is generated by the downward heave motion of the floating structure does not progress along SCR on the seabed and result in a large magnitude of lateral deformation at TDZ. Figures 3.48 and 3.49 also show that when there is an additional lateral damping force to the friction force, the magnitude of lateral deformation at the seabed and maximum bending moment decreased over TDZ.

3.2.7   Global buckling assessment

3.2.7.1   Scenario 1: Exposed pipeline on even seabed

A design flow for imperfection triggering global buckling is introduced in Figure 2.9. Since the assessment of global buckling is assumed to be a post design stage, operational conditions in a time series are investigated in this report. In this subsection, the minimum heave condition, which was introduced previously, is investigated for the assessment of global buckling. The radius of imperfection is obtained by dividing the bending moment by bending stiffness. The bending moment and tension distribution at minimum heave is shown in Figure 3.51.
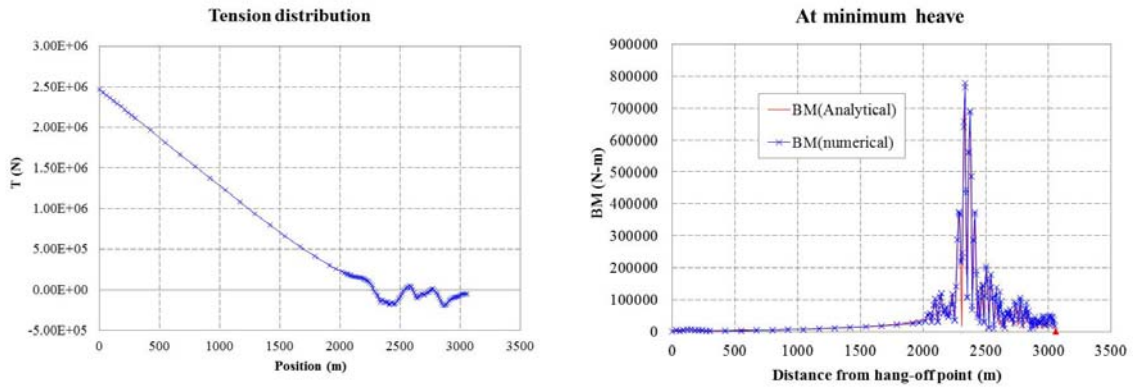
Figure 3.51 Tension and bending moment at minimum heave

Table 3.16 The variables of Figure 2.9 at maximum BM on SCR (FPSO)

Variable	Description	Number (unit)
$S(op)$	Compressive effective axial force	1.20E+05 (N)
$R(op)$	radius of imperfection	3.09E+01 (m)
$S_\infty^{LB}(100)$	$2.29 \cdot \dfrac{EI}{\overline{L}^2}$	1.51E+08 (N)
$\overline{L}$	$\left[\dfrac{(EI)^2}{\left(f_L^{LB}\right)^2 \cdot E \cdot A_s} \right]^{0.125}$	0.584 (m)
f_L^{LB}	Lower bound lateral soil resistance force	3.34E+03 (N)
$S(R)^{LB}(100)$	$f_L^{LB} \cdot R(op)$	1.03E+05 (N)
$R_\infty^{LB}(100)$	$2.41 \cdot (D-t) \cdot \sqrt{\dfrac{E \cdot t}{f_L^{LB}}}$	6.53E+02 (m)
k_{mb}	factor	1.5

93
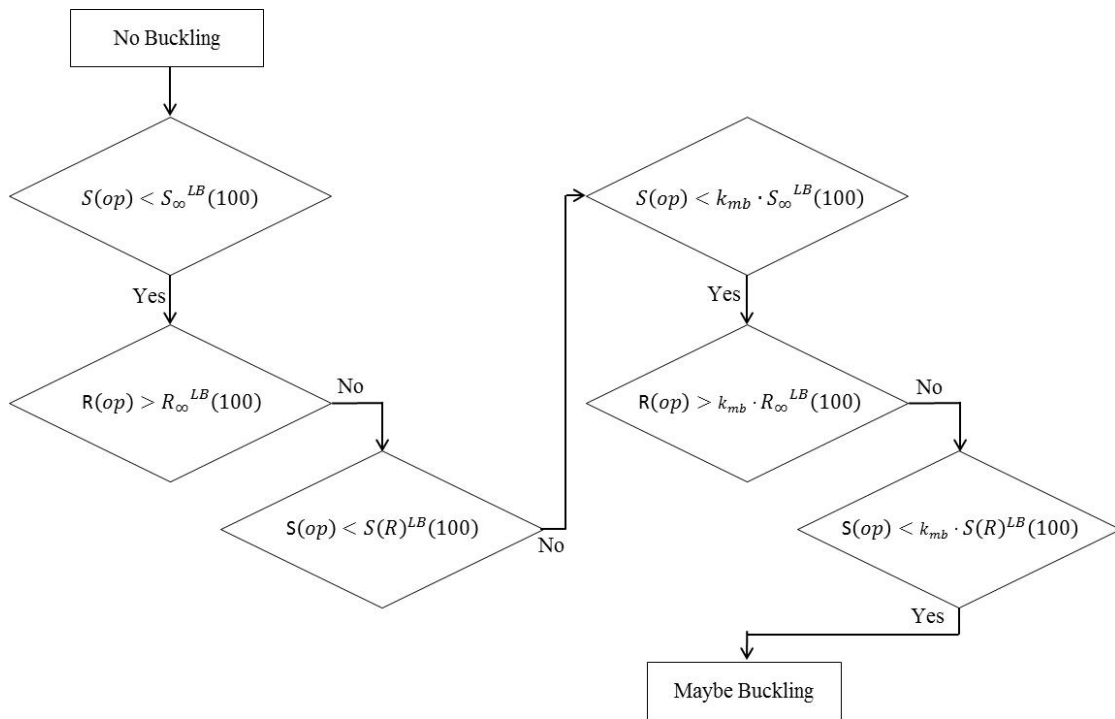
Figure 3.52 Flowchart for global buckling assessment at minimum heave

Using the numbers in Table 3.16, the result of global buckling assessment is shown in Figure 3.52. In case the result of assessment is Maybe Buckling as shown in Figure 3.52, in the pipe integrity check, fatigue analysis is not necessary.

3.2.7.2   Scenario 2: Exposed Pipeline on un-Even seabed

As previously explained, in order to avoid the complexity of the analysis, a simplified method for global buckling assessment is used with exposed pipelines on an un-even seabed. In this subsection, the maximum bending moment condition (Figures 3.53 and 3.54), which was introduced previously, is investigated to assess global buckling.
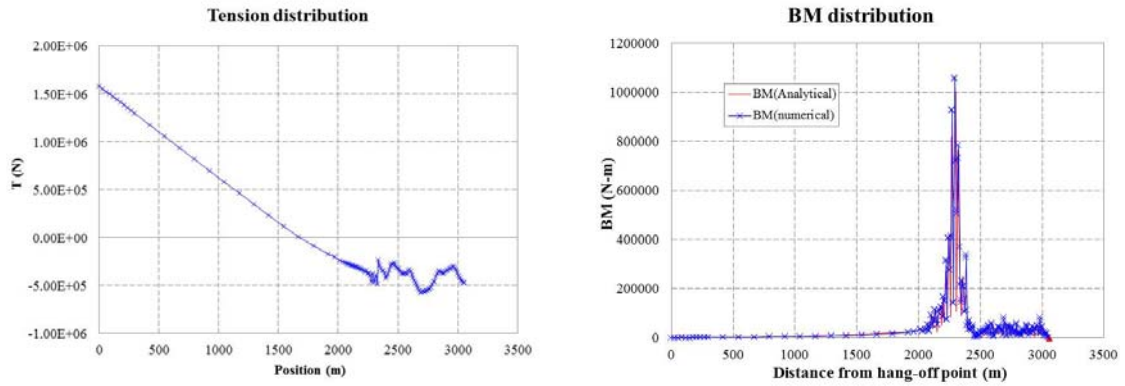
Figure 3.53 Tension and bending moment at maximum bending moment
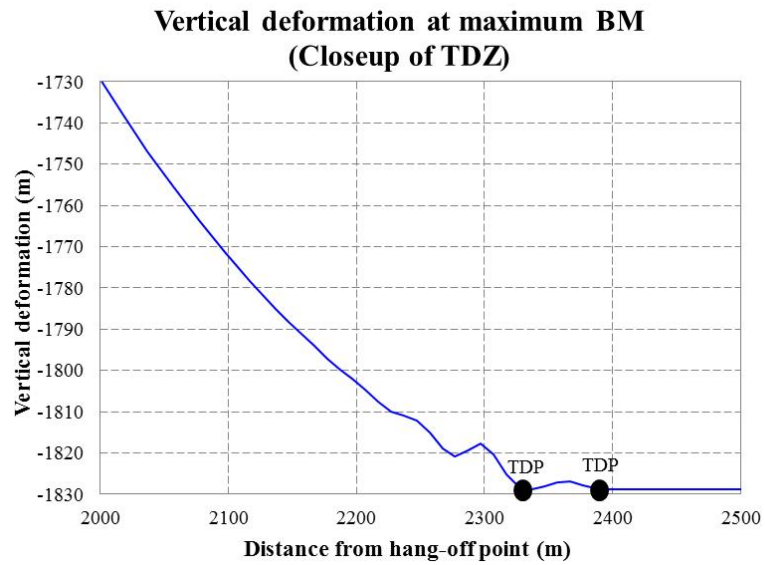
Figure 3.54 Side view of SCR with un-even seabed scenario

95

Table 3.17   The variables of criteria where maximum bending moment occurs

Variable	Description	Number (unit)	Check
S_R	Effective axial force in the uplift span section	Max: 4.26E+05 (N) Min: 2.31E+05 (N)	-
L_{uplift}	Length of pipeline lifted off at the free span crests	59.977 (m)	-
$\dfrac{\pi^2 \cdot EI}{\left(L_{uplift}\right)^2}$	Criterion for No lateral buckling	6.17E+04	Lateral buckling assessed
$\dfrac{4 \cdot \pi^2 \cdot EI}{\left(L_{uplift}\right)^2}$	Criterion for lateral buckling and optimized design by 3D	2.47E+05	Lateral buckling assessed

Global buckling was assessed according to the procedure for the scenario of Exposed Pipeline on un-Even seabed of DNV recommended practice. In this scenario, the curvature of SCR is observed in three dimensions and therefore a corresponding approach is required. However, the criteria at each step assess the possibility of lateral buckling with a simplified equation to avoid complexity of three dimensional analyses. The result shows that the compressive effective axial force is large enough to make SCR globally buckle into a lateral direction on the seabed; This requires further detailed investigation.

3.2.8   Pipe integrity check (Limit state analysis)

The pipe integrity check includes checks on the hoop stress, local buckling, von Mises tress and fatigue analysis. In this subsection, these analyses are performed based on the results of Chapter 3.2.6.2 to cover every step.

3.2.8.1   Von Mises stress calculations according to API design code

Concept and formulation for Von Misses stress calculations was previously introduced in Chapter 2.4.2. In this subsection, the input data is based on two conditions including the overall maximum bending moment, the overall minimum tension along SCR. Internal pressure for SCR is assumed to be 6,000 psi (41.3685 MPa) which is the same as 3.2.7.1. The input data for pressure and diameter are taken from Table 3.17. In this study, the tolerance of pipe wall thickness is neglected for the simplicity of analysis procedure. The design factor is 1.0 which represents the maximum operating load condition in design pressure in Table 2.13. The input data and the result of calculation are tabulated as follows:

Table 3.18   Von Mises stress at the maximum BM (2,300 m from hang-off point)

Variable	Description	Number (unit)
T_w / A	Tensile stress at TDZ at maximum BM	-2.78E+01 (MPa)
$M(D_o - t)/(2I_{xy})$	Observed maximum bending stress along SCR	1.03E+03 (MPa)
σ_{pr}	$-(p_o D_o + p_i D_i)/(D_o + D_i)$	-28.73 (Mpa)
$\sigma_{p\theta}$	$(p_i - p_o)(D_o / 2t_{min}) - p_i$	85.6 (MPa)
σ_{pz}	$T_w / A \pm M(D_o - t)/(2I_{xy})$	1.00E+03 (MPa) -1.05E+03 (MPa)
A	$(\pi/4)(D_o^2 - D_i^2)$	1.67E-02 (m2)
I_{xy}	$(\pi/64)(D_o^4 - D_i^4)$	1.12E-04 (m4)

σ_{API}	$max\left[\left\{\left(\sigma_{pr}-\sigma_{p\theta}\right)^2+\left(\sigma_{p\theta}-\sigma_{pz}\right)^2+\left(\sigma_{pz}-\sigma_{pr}\right)^2\right\}/2\right]^{1/2}$	1.09E+03 (MPa) 1.06E+03 (MPa)
U_{API}	$\sigma_{API}/\left(C_f C_a \sigma_y\right)$	**4.55** **4.45**

Table 3.19 Von Mises stress at the minimum T (2,720 m from hang-off point)

Variable	Description	Number (unit)
T_w/A	Tensile stress at TDZ at maximum BM	-5.38E+01 (MPa)
$M(D_o-t)/(2I_{xy})$	Observed maximum bending stress along SCR	2.27E+01 (MPa)
σ_{pr}	$-(p_o D_o + p_i D_i)/(D_o + D_i)$	-28.73 (Mpa)
$\sigma_{p\theta}$	$(p_i - p_o)(D_o/2t_{min}) - p_i$	85.6 (MPa)
σ_{pz}	$T_w/A \pm M(D_o-t)/(2I_{xy})$	-3.12E+01 (MPa) -7.65E+01 (MPa)
A	$(\pi/4)(D_o^2 - D_i^2)$	1.67E-02 (m2)
I_{xy}	$(\pi/64)(D_o^4 - D_i^4)$	1.12E-04 (m4)
σ_{API}	$max\left[\left\{\left(\sigma_{pr}-\sigma_{p\theta}\right)^2+\left(\sigma_{p\theta}-\sigma_{pz}\right)^2+\left(\sigma_{pz}-\sigma_{pr}\right)^2\right\}/2\right]^{1/2}$	1.44E+02 (MPa) 1.52E+02 (MPa)
U_{API}	$\sigma_{API}/\left(C_f C_a \sigma_y\right)$	**0.60** **0.64**

As shown in Table 3.18 and 3.19, bending moment is dominant at overall maximum bending moment condition and so is tension at overall minimum tension condition. However, the magnitude ratio of bending stress and tensile stress in two condition show that even in the overall minimum tension condition the magnitude ratio

of bending stress by tensile stress is approximately 0.42, while that in the overall

maximum bending moment condition is more than 37. This indicates that in the FPSO

case, the bending moment is generally dominant for the von Mises stress calculation.

The bending moment and corresponding bending stress can be either positive or negative,

as shown in Figure 3.55, in Table 3.19 and 3.20. Based on the calculated result in Table

3.19, the bending stress has its maximum magnitude when it is negative. The obtained

U_{API} in each case also corresponds to the magnitude of bending moment.
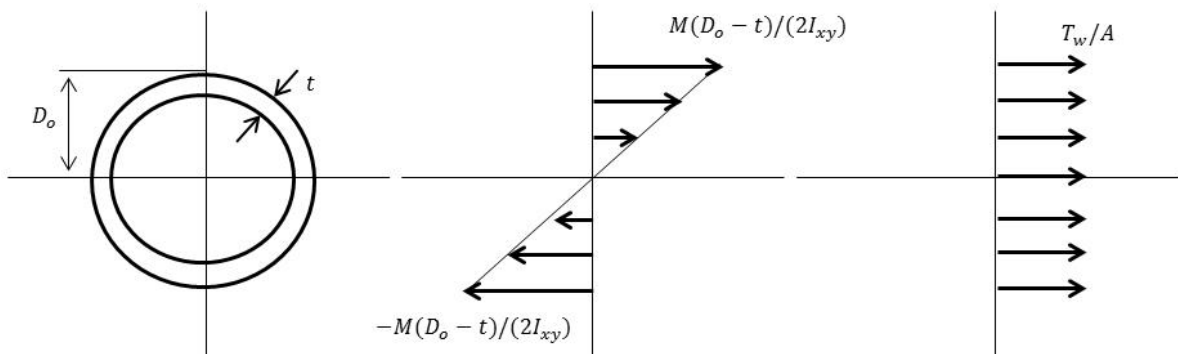
Figure 3.55 Tensile stress and bending stress on pipe

The obtained U_{API} is larger than 1.0; this result indicates that the von Mises

stress criteria are not satisfied with the current SCR design and FPSO model in the given

environmental condition. In the formulation, among all types of stress, the axial stress is

dominant in the magnitude and, particularly, the bending moment contribution is

significant.

Also, maximum strain can be calculated from the ratio of maximum nominal stress (sum of tensile stress and bending stress) and Young's modulus of steel, 200 (GPa), to check the material fail. The calculation is as below:

$$\sigma_{nominal} = \sigma_{tensile} + \sigma_{bending}$$

$$max.\sigma_{nominal} = 13.69E+08(Pa)$$

$$max.\varepsilon = \frac{max.\sigma}{E} = 0.006845$$

3.2.8.2   Maximum allowable bending moment criteria

In order to investigate the local buckling, the formulation for maximum allowable bending moment criteria is checked. The formulation was introduced in 4.3.3 and input data is based on the condition when / where the maximum bending moment is observed as introduced in 3.2.6.2. The input data is tabulated in Table 3.20.

Table 3.20   The variables of maximum allowable bending moment

Variable	Description	Number (unit)
M_p	$\left(1.05 - 0.0015\dfrac{D}{t}\right)SMYS \cdot D^2 t$	5.52E+05 (N-m)
F_l	$0.5 \cdot (SMYS + SMTS)A$	7.47E+06 (m2)
p_l	$p_l = 0.5(SMYS + SMTS)\dfrac{2t}{D}$	81.04 (MPa)
$M_{Allowable}$	$\dfrac{\eta_{RM}}{\gamma_c} M_p \sqrt{1-(1-\alpha^2)\left(\dfrac{p}{\eta_{RP}p_l}\right)^2} \cos(\dfrac{\pi}{2}\dfrac{\dfrac{\gamma_c F}{\eta_{RF}|F_l|} - \alpha \dfrac{p}{\eta_{RM}|p_l|}}{\sqrt{1-(1-\alpha^2)\left(\dfrac{p}{\eta_{RM}p_l}\right)^2}})$	1.16E+05 (N-m)

The obtained $M_{Allowable}$ is smaller than the maximum bending moment which is observed in the time series and more than 7E+05 (N-m). This result indicates that the design of the SCR model does not satisfy the given environmental conditions.

3.2.9   Fatigue

As previously introduced, the accumulated damage from stress cycles with various ranges is first calculated to assess the short term damage. Table 3.21 shows the procedure and variables including blocks of the stress ranges and distribution of corresponding numbers of occurrence at 2,267 m from hang-off point. As already mentioned, the Miner-Palmgren rule is used to accumulate fatigue damage with the formulation shown below:

$$D_{fat} = \sum_i \frac{n(S_i)}{N(S_i)} = \frac{1}{a} \sum_i n(S_i) S_i^m$$

, where

D_{fat} : Accumulated fatigue damage (Palmgren-Miner rule)

DFF : Design Fatigue Factor (Table 2.17)

$n(S_i)$: Number of stress cycles with range S_i

$N(S_i)$: Number of stress cycles to failure given by S-N curve

Table 3.21   Table of variables for accumulated damage calculation at TDZ

Block	Min (Mpa)	Max (Mpa)	Ave. (Mpa)	stress^m	N of cycle	Short term D_{fat}
30	1.16E+03	1.20E+03	1.18E+03	2.29E+15	0	0.00E+00
29	1.12E+03	1.16E+03	1.14E+03	1.93E+15	0	0.00E+00
28	1.08E+03	1.12E+03	1.10E+03	1.61E+15	0	0.00E+00
27	1.04E+03	1.08E+03	1.06E+03	1.34E+15	1	1.97E+00
26	1.00E+03	1.04E+03	1.02E+03	1.10E+15	0.5	8.13E-01
25	9.60E+02	1.00E+03	9.80E+02	9.04E+14	0	0.00E+00
24	9.20E+02	9.60E+02	9.40E+02	7.34E+14	2.5	2.70E+00
23	8.80E+02	9.20E+02	9.00E+02	5.90E+14	3.5	3.04E+00
22	8.40E+02	8.80E+02	8.60E+02	4.70E+14	6	4.16E+00
21	8.00E+02	8.40E+02	8.20E+02	3.71E+14	5.5	3.00E+00
20	7.60E+02	8.00E+02	7.80E+02	2.89E+14	7	2.98E+00
19	7.20E+02	7.60E+02	7.40E+02	2.22E+14	4.5	1.47E+00
18	6.80E+02	7.20E+02	7.00E+02	1.68E+14	6	1.48E+00
17	6.40E+02	6.80E+02	6.60E+02	1.25E+14	5	9.22E-01
16	6.00E+02	6.40E+02	6.20E+02	9.16E+13	7	9.44E-01
15	5.60E+02	6.00E+02	5.80E+02	6.56E+13	12.5	1.21E+00
14	5.20E+02	5.60E+02	5.40E+02	4.59E+13	7	4.73E-01
13	4.80E+02	5.20E+02	5.00E+02	3.13E+13	10	4.60E-01
12	4.40E+02	4.80E+02	4.60E+02	2.06E+13	17	5.16E-01
11	4.00E+02	4.40E+02	4.20E+02	1.31E+13	6.5	1.25E-01
10	3.60E+02	4.00E+02	3.80E+02	7.92E+12	13	1.52E-01
9	3.20E+02	3.60E+02	3.40E+02	4.54E+12	15.5	1.04E-01
8	2.80E+02	3.20E+02	3.00E+02	2.43E+12	14.5	5.19E-02
7	2.40E+02	2.80E+02	2.60E+02	1.19E+12	17.5	3.06E-02
6	2.00E+02	2.40E+02	2.20E+02	5.15E+11	23.5	1.78E-02
5	1.60E+02	2.00E+02	1.80E+02	1.89E+11	40	1.11E-02
4	1.20E+02	1.60E+02	1.40E+02	5.38E+10	76	6.02E-03
3	8.00E+01	1.20E+02	1.00E+02	1.00E+10	184.5	2.72E-03
2	4.00E+01	8.00E+01	6.00E+01	7.78E+08	387.5	4.44E-04
1	0.00E+00	4.00E+01	2.00E+01	3.20E+06	2126	1.00E-05

$$D_{fat} = 2.66E + 01$$

$$D_{fat} \cdot DFF \leq 1$$

From the result of the short term fatigue analysis above, the accumulated damage does not satisfy the criteria with any design fatigue factor (DFF). After all, the SCR model in this study fails the fatigue analysis when the high design fatigue factor is required. Figure 3.56 and Table 3.22 shows the accumulated fatigue damage distribution along SCR. Those results indicate the most severe fatigue damage is found near TDZ and the calculated short term fatigue damages of SCR on seabed (between 3,060 m and 2,100 m from hang-off point) do not satisfy the criteria with high design fatigue factor (=10).
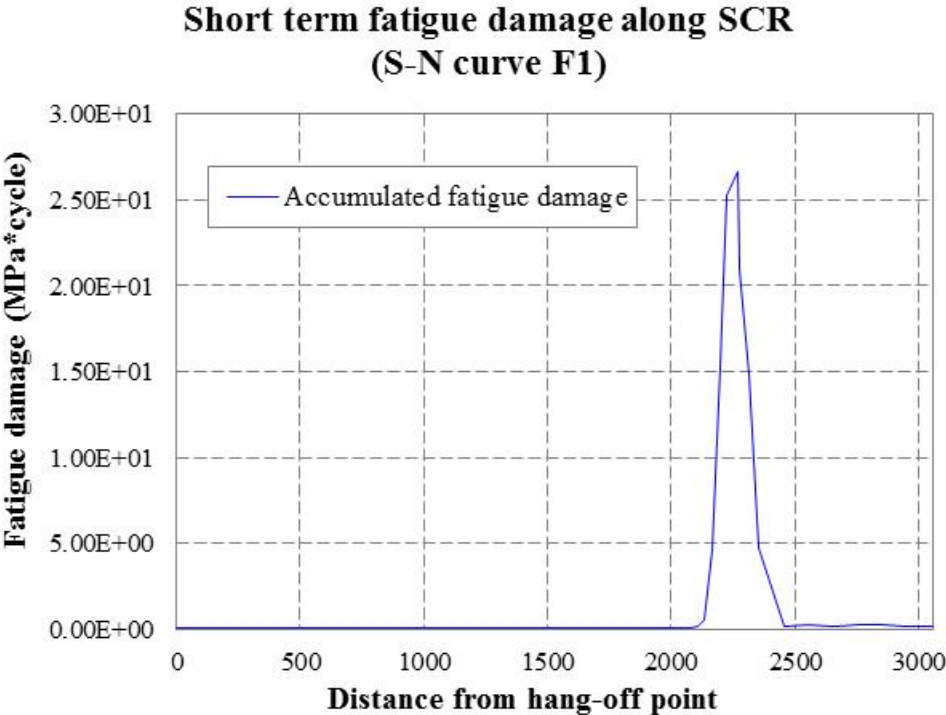

Figure 3.56 Accumulated short term fatigue damage along SCR

Table 3.22   Short term fatigue damage at nodes of SCR

No.	Distance from hang-off point (m)	Short term fatigue damage (Mpa*cycle)	Criteria with high safety factor (=10)
1	3056.5	1.79E-01	Not satisfied
2	2956.5	1.62E-01	Not satisfied
3	2856.5	2.11E-01	Not satisfied
4	2756.5	2.10E-01	Not satisfied
5	2656.5	2.00E-01	Not satisfied
6	2556.5	2.17E-01	Not satisfied
7	2456.5	1.46E-01	Not satisfied
8	2356.8	4.74E+00	Not satisfied
9	2316.8	1.48E+01	Not satisfied
10	2277.0	2.09E+01	Not satisfied
11	2267.0	2.66E+01	Not satisfied
12	2227.1	2.52E+01	Not satisfied
13	2197.1	1.54E+01	Not satisfied
14	2166.5	4.60E+00	Not satisfied
15	2136.5	5.29E-01	Not satisfied
16	2106.5	1.34E-01	Not satisfied
17	2076.5	8.95E-02	Satisfied
18	2036.5	8.57E-02	Satisfied
19	1916.6	8.14E-02	Satisfied
20	1792.5	8.31E-02	Satisfied
21	1543.9	9.13E-02	Satisfied
22	1295.2	9.26E-02	Satisfied
23	1046.4	9.51E-02	Satisfied
24	797.6	9.67E-02	Satisfied
25	548.8	9.69E-02	Satisfied
26	300.0	9.69E-02	Satisfied
27	240.0	1.00E-01	Satisfied
28	180.0	1.01E-01	Not satisfied
29	120.0	9.81E-02	Satisfied
30	60.0	1.06E-01	Not satisfied
31	0.0	9.82E-02	Satisfied

4   SUMMARY AND CONCLUSION

The coupled dynamic analysis of the hull-mooring-riser was performed for spar platform and FPSO using CHARM3D. The motions of floating production facilities were analyzed by displacement and spectrum investigation. Coupled motions and force components of SCR nodes near TDZ were checked in order to understand the behavioral characteristics such as sub-critical local dynamic buckling at TDZ. When a negative effective tension was observed in the behavioral characteristics, criteria for global buckling was applied to investigate whether a pipe integrity check including von Mises stress, maximum strain for material fail, local buckling and fatigue analysis is necessary for the SCR model. Also, sensitivity of element size to the force components of SCR was checked focusing on the relationship between element sizes and bending moment of TDZ.

In the spar case, compared to heave motion, surge motion was dominant because of the large displacement of the spar hull and the buoyancy-can effect which decouples the heave motion of TTR and the spar platform so the set-down effect on the hull decreases. When the surge displacement of the spar was either maximum or minimum as shown in Figure 3.10, the observed bending moment along SCR varied according to the location of the hang-off point. This showed the correlation between the surge displacement of the hang-off point and bending moment on SCR at TDZ. Also, as shown in 3.1.4.1, the heave hang-off velocity had a high correlation with effective tension on SCR at TDZ. However, it is concluded that no sub-critical local dynamic buckling was

assessed with the spar model. That can provide a feedback to the initial SCR design to confirm there is no problem.

In the FPSO case, the heave motion was found to be much greater than the spar. That led to the negative effective tension on SCR and corresponding sub-critical local dynamic buckling which results in the propagating deformation and bending moment along SCR. The maximum negative effective tension and bending moment were both found at TDZ, near TDP. The comparison between seabed with and without coulomb friction also confirmed the idea that seabed friction inhibits the propagation of compression on SCR. The correlation between the motion of FPSO and force components on SCR was also found showing that both surge and heave motions are correlated with the bending moment on the SCR at TDZ. The results of global buckling assessment by scenarios indicated that there is global buckling on SCR at TDZ and a pipe integrity check (limit state analysis) is necessary. The criteria for the pipe integrity check, however, were not satisfied with the SCR model for FPSO in this study. Specifically, the criteria of von Mises stress, local buckling and short term damage criteria were not satisfied. That shows how the instability of SCR caused by sub-critical local dynamic buckling results in the failure of the model.

The analysis results give feedback to the initial SCR design for an improved design. The most critical reason for the failure was too much nominal stress. Since the nominal stress consists of tensile stress and bending stress, several approaches to reduce these stresses can be considered from the viewpoint of engineering. First, using a different kind of SCR which can absorb excessive compression on the SCR is possible.

Lazy wave SCR can be a good example. Second, increasing the wall thickness of SCR can be the next option. Since tensile stress and bending stress are affected by the sectional area of the pipeline and area moment of inertia respectively, increasing the wall thickness can reduce the stress in operating conditions. However, in this case, the weight of SCR and corresponding top tension should be carefully calculated again.

There are some issues for a more refined analysis. First, a function for the check of elastic and plastic deformation and material fail is necessary to CHARM3D. The SCR in this study is simulated as if it has indefinite minimum yield stress so a manual integrity check was necessary as performed in this study. Therefore it will be necessary to add functions for the check of elastic and plastic deformation and collapse of the material to CHARM3D program.

The soil resistance of the seabed is also one of the concerns. If the seabed is assumed as a mud floor, the repeated cycles of interaction between SCR and seabed should form topography such as trench and berms which affect the next cycle of SCR behavior on the seabed. In this study, however, the seabed was assumed to be flat and the seabed topography is not formed by the SCR-soil interaction. Therefore the seabed in this study should be assumed as a hard and flat floor which has a constant friction over the area. The resistance on the seabed is one of the important driving factors for a sub-critical local dynamic buckling at TDZ. Therefore the models for the topography and resistance factors on the seabed need to be developed for more precise simulation.

REFERENCES

API Bulletin 2INT-MET, 2007. Interim guidance on hurricane conditions in the Gulf of Mexico. American Petroleum Institute, 3-5, Washington, DC.

API RP 2RD, 2009. Design of risers for floating production systems (FPSs) and tension-leg platforms (TLPs), American Petroleum Institute, 83, Washington, DC.

Aubeny, C., Biscontin, G., 2008. Interaction model for steel compliant riser on soft seabed. In: Proceedings of the Offshore Technology Conference, Houston, TX.

Aubeny, C., Biscontin, G., 2009. Seafloor-riser interaction model. International Journal of Geomechanics, 9, 133-141.

Bridge, C., Howells, H., Toy, N., Parke, G., and Woods, R. (2003). Full scale model tests of a steel catenary riser. In: Proceedings of Int. Conf. on Fluid Structure Interaction, Cadiz, Spain.

Bruton, D., White, D., Carr, M., Cheuk, C., 2008. Pipe-Soil Interaction During Lateral Buckling and Pipeline walking – The SAFEBUCK JIP, In: Proceedings of the Offshore Technology Conference, Houston, TX.

Bruton, D., White, D., Cheuk, C., Bolton, M., Carr, M., 2006. Pipe/Soil interaction behavior during lateral buckling, including large-amplitude cycle displacement tests by the Safebuck JIP. In: Proceedings of the Offshore Technology Conference, Houston, TX.

Cheng, Y., Song, R., Mekha, B., Torstrick, A., Liu, H., 2007. Compression assessment of deepwater steel catenary risers at touch down zone, In: Proceedings of the Offshore Mechanics and Arctic Engineering, San Diego, CA.

Det Norske Veritas, 2007. Recommended Practice DNV RP F110, Global buckling of submarine pipelines Structural design due to high temperature/high pressure, DNV Services, Research and Publications, Hovik, Norway.

Det Norske Veritas, 2010. Offshore Standard DNV-OS-F201, Dynamic risers, DNV Services, Research and Publications, Hovik, Norway.

Det Norske Veritas, 2010. Recommended Practice DNV RP C203, Fatigue design of offshore steel structures, DNV Services, Research and Publications, Hovik, Norway.

Det Norske Veritas, 2010. Recommended Practice DNV RP F204, Riser fatigue, DNV Services, Research and Publications, Hovik, Norway.

Hauch S. and Bai Y., 1999. Bending Moment Capacity of Pipes, In: Proceedings of the Offshore Mechanics and Arctic Engineering, St. John's, Newfoundland, Canada.

Hobb R.E., 1984. In-service buckling of Heated pipelines, ASCE (American Society of Civil Engineer) Journal of Transportation Engineering, 119, 175-189.

Kim, Y.B., and Kim, M.H., 2002. Hull/mooring/riser coupled dynamic analysis of a tanker-based turret-moored FPSO in deep water, In: Proceeding of the 12th International Offshore and Polar Engineering Conference, KitaKyushu, Japan.

Kim, M.H., Tahar, A., Kim, Y.B., 2001. Variability of TLP motion analysis against various design methodologies/parameters, In: Proceedings of the 11th International Offshore and Polar Engineering Conference, Stavanger, Norway.

Koo, B., 2003. Evaluation of the effect of contact between risers and guide frames on offshore spar platform motions, Ph.D. Dissertation, Ocean Engineering Department, Texas A&M university, College Station, TX.

Kuiper, G., Brugmans, J. and Metrikine, A., 2007. Destabilization of deep-water risers by a heaving platform, Journal of sound and vibration, 310, 541-557.

McCann, D., Smith, F., O'Brien, P., 2003. Guidelines for compression modeling in flexible risers for deepwater applications, In: Proceedings of the Offshore Technology Conference, Houston, TX.

Nakhaee, A., 2010. Study of the fatigue life of steel catenary risers in interaction with the seabed, Ph.D. Dissertation, Ocean Engineering Department, Texas A&M university, College Station, TX.

National Data Buoy Center, 2013. Station history, Retrieved from http://www.ndbc.noaa.gov/station_history.php?station=42360

National Renewable Energy Laboratory. (2008). Biofuels. Retrieved May 6, 2008, from http://www.nrel.gov/learning/re_biofuels.html

Song, R., Stanton, P., 2009, Advances in deepwater steel catenary riser technology state-of-the-art: part II – Analysis, In: Proceedings of the Offshore Mechanics and Arctic Engineering, Hawaii, USA

Tahar, A., Kim, M., 2003. Hull/mooring/riser coupled dynamic analysis and sensitivity study of a tanker-based FPSO. Applied Ocean Research 25(6), 367-382.

Tahar, A., Ran, Z., and Kim, M.H., 2002, Hull/mooring/riser coupled spar motion analysis with buoyancy-can effect. In: Proceedings of the 12th International Offshore and Polar Engineering Conference, Kitakyshu, Japan.

Wichers, J.E.W., Devlin, P. V., 2001. Effect of coupling of mooring lines and risers on the design values for a turret moored FPSO in deep water of Gulf of Mexico. In: Proceedings of the 11th International Offshore and Polar Engineering Conference, Stavanger, Norway.

Yang, C.K., Kim, M.H., 2010. Transient effects of tendon disconnection of a TLP by hull-tendon-riser coupled dynamic analysis. Journal of Ocean Engineering 37 (8-9), 667-677.

Yue, B., Walters, D., Yu, W., Raghavan, K., Thompson, H., 2011. Lazy Wave SCR on Turret Moored FPSO, In: Proceedings of the 11th International Offshore and Polar Engineering Conference, Stavanger, Norway.

Zhou, J., Liu, Y., Li, X., 2010. Pipe Walking-Lateral Buckling Interaction, In: Proceedings of Earth and Space 2010: Engineering, Science, Construction, and Operations in Challenging Environment 2010 ASCE, Hawaii, USA.

Zou, J., 2012, Semisubmersible platforms with Steel Catenary Risers for Western Australia and Gulf of Mexico, Techno Press, 2(2), 99-113.